

Welding induced residual stresses in a segment of an orthotropic steel deck

MSc thesis

Arvid Maarleveld



Welding induced residual stresses in a segment of an orthotropic steel deck

by

Arvid Maarleveld

to obtain the degree of Master of Science

at the Delft University of Technology,

to be defended publicly on Wednesday May 4, 2022 at 15:00.

Student number: 4363876

Project duration: June 14, 2021 – May 4, 2022

Thesis committee: Prof. dr. ir. M. Veljkovic, TU Delft, CEG, Steel and Composite structures, Chair
Dr. ir. J. A. F. P. Correia, TU Delft, CEG, Steel and Composite structures
Dr. ir. J. H. den Besten, TU Delft, 3ME, Maritime and Transport Technology
Ir. D. H. Malschaert, TU Delft, CEG, Steel and Composite structures, Daily supervisor
Ir. B. van Aken, Iv-Infra, Daily supervisor

An electronic version of this thesis is available at <http://repository.tudelft.nl/>.

Cover Image: Suurhoffbrug fabricated by Hollandia Infra where high frequency mechanical impact (HFMI) post weld treatment has been applied to compensate for welding residual stresses in critical fatigue details. Source: Paul van Baardwijk, Rijkswaterstaat



Preface

Before you lies the master thesis "Welding induced residual stresses in a segment of an orthotropic steel deck". A numerical model was developed which predicts the residual stress distribution. The model was validated by temperature and distortion measurements. This thesis has been written to obtain the master's degree for Civil Engineering at Delft University of Technology. The project started in June 2021 and will end in May 2022.

This research topic was formulated together with professor Veljkovic and the engineering company Iv-Infra, where I undertook an internship. The project was difficult regarding the organization of the experiment, the establishment of a new methodology for measuring distortions with a 3D scanner and overcoming convergence errors in the numerical model, but extensive research has allowed me to answer the research question. I would like to express my gratitude to my graduation committee.

Firstly, I would like to thank prof. Veljkovic for helping me formulate the research topic, for the helpful suggestions during the progress meetings and for the opportunity for presenting my work at the IABSE conference.

Secondly, I would like to thank dr. Correia and dr. den Besten for their helpful suggestions they gave me during the meetings and for the helpful comments on my report.

Thirdly, I want to thank my daily supervisors, David and Bart, for their excellent guidance. Bart and David gave me helpful suggestions for improving the report and were always available to answer my theoretical and practical questions. David assisted me really well during the experiment and with problems I encountered in the numerical model.

Finally, I would like to thank my family and friends for their support and their advice.

*Arvid Maarleveld
Delft, April 2022*

Summary

Welded details in orthotropic steel decks (OSD) are susceptible to fatigue cracks which are caused by local weld defects, geometric stress concentrations and residual tensile stresses. Residual tensile stresses are formed during the welding process and the distribution depends on many factors. Knowledge about the residual stress distribution is required for accurate fatigue assessment. The rib-to-crossbeam detail in the design of the new Schipholbridge does not meet the fatigue requirements according to Eurocode 3 when using a reasonable geometry. Therefore, high frequency mechanical impact (HFMI) post weld treatment will be used to improve fatigue resistance. Incorporating the residual stress distribution in fatigue life prediction models will improve their accuracy, which can lead to more favorable results which can avoid the use of HFMI. The main objective of this master thesis is to determine the accuracy of a subsequently coupled thermo-mechanical finite-element model which predicts welding induced residual stresses in a segment of an OSD. The fatigue life prediction is not included in the scope of this thesis. The accuracy of the model was determined by comparing temperature and distortions with experimental data from three specimens consisting of a 900x400mm deck plate, a 350mm deep trapezoidal stiffener and a 600x15mm crossbeam web with a Haibach cope hole. During the welding, temperatures were recorded by a FLIR® E96 thermal camera. Welding distortions were obtained by subtracting the geometry before welding from the geometry after welding. The 3D geometry was obtained by the Artec® LEO scanner. The scans were post processed in Artec® studio software and data was extracted by the NumPy-stl package in Python. The predicted temperature distribution and deformations corresponded well to experimental results. The maximum deviation in the temperature distribution 1.8s after welding was 67 °C and occurred at the last position of the welding torch. The maximum deviation between predicted and measured upward displacements of the deck plate 10mm from the edge was 0.2mm, with smaller deviations on average. Due to the good correspondence of experimental and numerical results, residual stresses were presented. On the deck plate in longitudinal direction, tensile stresses of yield strength magnitude were obtained after unclamping. At the rib-to-crossbeam connection, the stress in the direction perpendicular to the weld toe at the location of the weld toe was equal to the yield strength after unclamping. The stresses quasi-linearly go to zero through the thickness of the rib.

Contents

Preface	i
Summary	ii
1 Introduction	1
1.1 Background information	1
1.1.1 Welded joints and residual stresses	1
1.1.2 Fatigue problems in welded connections in orthotropic steel bridge decks	2
1.2 Problem statement	3
1.3 Research objectives	4
1.4 Methodology	4
1.5 Scope	4
1.6 Research structure	5
2 Literature review	6
2.1 Physics of fatigue	6
2.2 Fatigue assessment methods	8
2.3 Welding induced residual stresses	9
2.3.1 Formation process	9
2.3.2 Effect on fatigue resistance	10
2.3.3 Relaxation	10
2.3.4 Measurement methods	11
2.3.5 Prediction models	13
2.4 Experimental and numerical results	15
2.4.1 Hole-drilling method	15
2.4.2 Distortion measurements	16
3 Welding experiment	18
3.1 Introduction	18
3.2 Specimens, equipment and experimental set-up	18
3.3 Experimental procedure	19
3.4 Data processing	21
3.5 Results	24
3.5.1 Temperature	24
3.5.2 Distortions	26
3.6 Conclusions	30
3.7 Discussion	30
3.8 Recommendations	31
4 Numerical simulation of the welding experiment	32
4.1 Introduction	32
4.2 Units	32
4.3 Model	33
4.4 Model details	35
4.4.1 Mesh	35
4.4.2 Steps	36
4.4.3 Boundary conditions	37
4.5 Heat input	38
4.6 Material properties	39
4.7 Parametric study	41

4.8	Results	42
4.8.1	Temperature	42
4.8.2	Displacements	45
4.8.3	Residual stresses	48
4.9	Conclusions	52
4.10	Discussion	53
5	Conclusions & Recommendations	54
5.1	Conclusions	54
5.2	Discussion	55
5.3	Recommendations	55
	References	60
A	IABSE conference paper	61
B	Raw data geometry Artec scanner	72
C	Python script thermal model	74
D	Python script mechanical model	78
E	Dflux subroutine	84
F	Documentation of experiment	87
F.1	Welding parameters	87
F.2	Tack weld geometry	89

Introduction

1.1. Background information

1.1.1. Welded joints and residual stresses

Welding is a widely used process for joining metals. It is applied in bridges, marine structures, pipelines, ships and more. Before welding was introduced in the late 1930s and early 1940s, connections in these structures were riveted. Welded structures are superior to riveted structures for many reasons including higher strength, water tightness, weight savings, simple design and high construction speed. However, despite its advantages, welded joints are prone to distortions and fatigue damage. Distortions reduce the accuracy of assembly, cause an undesirable appearance and reduce the strength of welded joints [1]. Fatigue damage occurs due to weld defects, geometric stress concentrations and tensile residual stresses [2, 3, 4]. Tensile residual stresses are formed during the welding process by steep temperature gradients causing incompatible thermal strains. Restrained thermal shrinkage during cooling leads to tensile residual stresses that can reach the yield strength. Tensile stresses cause initial fatigue cracks to remain open and increase the crack growth rate [5, 6]. The formation process is illustrated in Figure 1.1, where natural shrinkage of the weld material is shown in Figure 1.1a and the restrained shrinkage in Figure 1.1b [7].

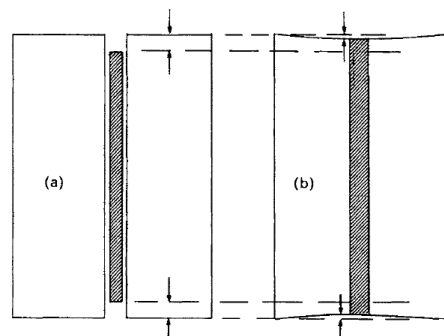


Figure 1.1: Formation process of welding residual stresses. Longitudinal shrinkage is restrained by surrounding, cooler material. Unrestrained shrinkage (a) and restrained shrinkage (b) [7]

Residual stresses in a butt weld in longitudinal and transverse direction are shown in Figure 1.2. Tensile residual stresses of high magnitude are found near the weld in Figure 1.2b. The magnitude is usually as high as the yield strength [2].

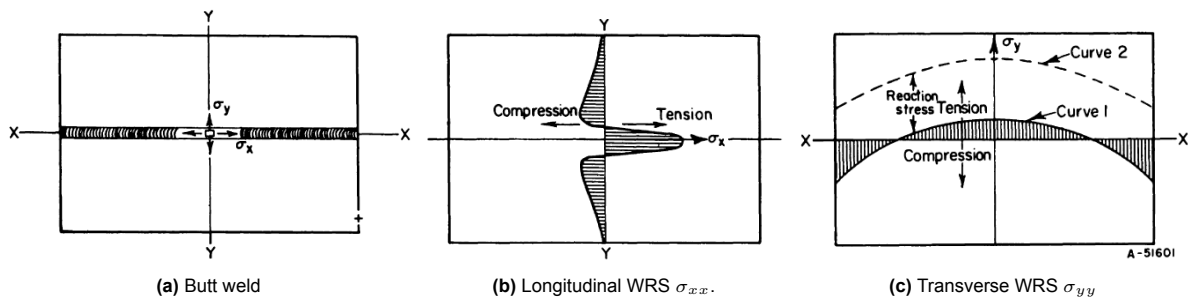


Figure 1.2: Longitudinal and transverse welding residual stress (WRS) distribution in a butt joint [2]

1.1.2. Fatigue problems in welded connections in orthotropic steel bridge decks

An orthotropic steel bridge deck consists of a deck plate, stiffeners in longitudinal direction, crossbeams and main girders, see Figure 1.3 [8]. The structures have many advantages, such as a relatively low self-weight, high load capacity and a practical construction process. Due to these advantages, the structures are widely used around the world. For long-span bridges and movable bridges, the low self-weight is particularly important [9].

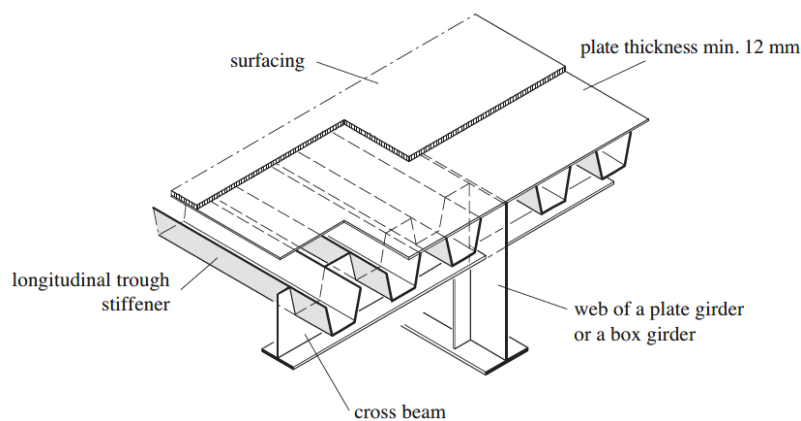


Figure 1.3: Orthotropic steel deck [8].

Despite the positive characteristics, the welded details are prone to fatigue. In research by de Jong [10], detected cracks have been divided in four categories, namely:

1. Cracks in the deck plate;
2. Cracks in the weld through-deck plate;
3. Cracks in the stiffener splice joint; and
4. Cracks in the through-crossbeam connection.

In Figure 1.4a, deck plate crack types DPS01 and DPS02 are shown. Both crack types are similar, but occur at a different location. The crack originates from the weld root and propagates into the deck plate. In the Netherlands, deck plate cracks have been observed in the Moerdijk bridge, Galecopper Bridges, van Brienoord bridge and several others [10, 11]. A crack in the weld starting from the root has also been observed as mentioned in point number 2. Cracks in the deck plate or stiffener originating from the weld toe are possible, but have not been observed yet [12]. In Figure 1.4b, observed cracks in the rib-to-crossbeam connection with a Haibach cope hole are shown. Repairing existing bridges and preventing fatigue damage in new bridges is important, especially now that traffic intensity and loads have been increasing [10, 11].

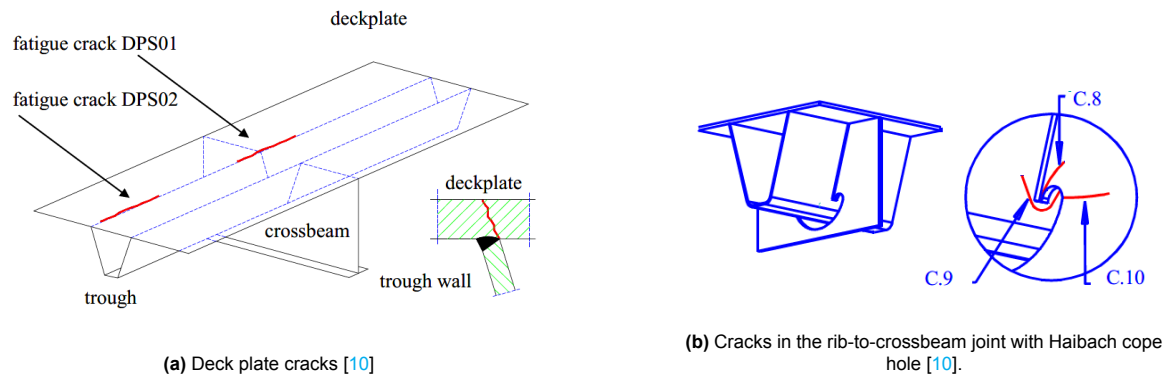


Figure 1.4: Cracks in the deck plate and around the Haibach cope hole [10]

1.2. Problem statement

For the design of the new orthotropic steel bridge decks in the Schipholbrug, the engineering company Iv-Infra concluded that, when using a reasonable geometry, the rib-to-crossbeam connection does not fulfill the fatigue requirements according to the detail category 80 in table 8.8 in EN1993-1-9 [13]. Additional detail categories for this rib-to-crossbeam detail are given in the design recommendations in ROK 2.0 [14]. Detail 3a was found governing, where a crack occurs in the through, originating from the weld toe due to vertical stresses in the through, see Figure 1.5. It only meets the fatigue requirements after applying HFMI post weld treatment. The detail category improves from 100 to 140. In addition, the slopes m_1 and m_2 change from 3 and 5 to 5 and 9, respectively. HFMI post weld treatment introduces residual compressive stresses in the weld toe and therefore compensates for residual tensile stresses introduced by the welding process. While this treatment allows for an economic design, it is a laborious treatment and it removes redundancy in design, so the fatigue resistance can no longer be improved during its lifetime.

The engineering company is interested in the accuracy of the detail category and whether HFMI is actually required. Since the distribution of residual stresses has a large influence on the fatigue life and depends on many factors, the fatigue life estimate of detail 3a might be conservative. In addition, the Schipholbrug detail has some deviations compared to detail 3a. The crossing angle between the stiffener and the crossbeam web is not perpendicular and the rib-to-crossbeam joint will be fabricated with a double fillet weld, instead of a double bevel groove, for practical reasons. More research is required to accurately assess the fatigue resistance and to determine the effect of the crossing-angle and weld type on the fatigue resistance.

The exact background of the ROK 2.0 is not publicly available, but detail categories are obtained from a series of testing. While S-N curves found in the Eurocode and ROK 2.0 are proven safe, more research needs to be performed to quantify the effect of different welding techniques, geometries and installation procedures on fatigue life [12]. In addition to testing, several fatigue prediction methods are available based on full range S-N curves [15], strain energy density [16] or Linear Elastic Fracture Mechanics (LEFM) [12]. Residual stresses can be incorporated in these prediction models to increase their accuracy.

Residual stresses can be measured by methods such as incremental hole-drilling or diffraction techniques [17]. Predicted models also exist based on a thermo-mechanical analysis with the Goldak double ellipsoid heat source model (DEHSM) [18]. However, since welding is a complicated process and the residual stress distribution depends on many parameters, several simplifications and assumptions need to be made in computational welding mechanics [19, 3]. To gain confidence in these simplifications and increase the accuracy of predicted results, experimental validation is required. With data obtained from experimental results, welding processes can be optimized.

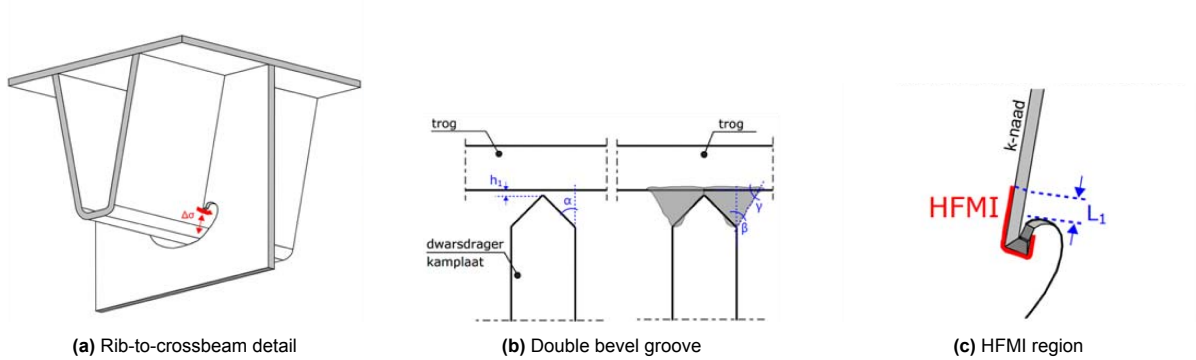


Figure 1.5: Detail 3a in ROK 2.0 [14]. A crack originates from the weld toe due to vertical stresses in the rib and propagates into the rib.

1.3. Research objectives

The main objective of the research is to obtain residual stress distributions from a numerical model to be used in fatigue prediction models in future research. To gain confidence in simplifications used in the model, the model is validated by experimentally obtained temperature distributions and deformations. The second objective is to establish a new experimental methodology with the use of a handheld 3D scanner to obtain welding distortions.

The main research question is:

- *To what level of accuracy can a numerical welding simulation model predict welding-induced temperature gradients, distortions and residual stresses in a segment of an orthotropic steel deck?*

The main research question will be answered with the following sub-questions.

- What is the measured temperature distribution around the heat source?
- What is the measured distortion field?
- How does the measured distortion field compare with the numerical welding simulation model?
- What values of WIR stresses result from the numerical model?

1.4. Methodology

Experimental data will be obtained from welding experiments on three specimens. The specimens represent a segment of an OSD and consist of a deck plate, trapezoidal stiffener and a crossbeam, as shown in Figure 1.5a. The crossbeam web has a Haibach cope hole. Welding distortions will be obtained by comparing 3D geometry scans before and after welding obtained by the Artec Leo © scanner. Temperature distributions will be measured by a FLIR © E96 thermal camera.

The numerical simulation is based on a subsequently coupled thermal and mechanical finite-element analysis in the commercially available software package called Abaqus ©. In the thermal analysis, the welding heat source is substituted by the Goldak double ellipsoid heat source model [20] and the obtained results are used as a predefined field in the mechanical analysis. The deposition of filler material is simulated by the birth and death principle which is used by many researchers among which Xin and Veljkovic [4].

1.5. Scope

This research focuses on prediction of residual stresses and measurements of temperature and distortions in a segment of an OSD. The fatigue lifetime prediction is not included in the scope of this thesis. The influence of the crossing angle and a double bevel groove instead of a fillet weld on the residual stress distribution is also not included in the scope.

1.6. Research structure

In chapter 2, a literature review is performed where the physics of fatigue, fatigue assessment methods, effects of residual stresses on fatigue resistance and experimental and numerical methods for obtaining residual stresses and distortions are explained.

In chapter 3, the welding experiment is discussed. The experimental setup, sequence of events, methodology and experimental results are given.

In chapter 4, the numerical simulation of the welding experiment is discussed. The model details, material properties, loads and results are presented. The resulting temperature distribution and distortions are compared to experimental values. Finally, residual stresses are presented along various paths on the specimen and around the weld seam.

In chapter 5, conclusions are drawn and research questions are answered. Additionally, recommendations are given about the established experimental methodology, modelling considerations and steps for future research.

2

Literature review

In this chapter, a literature review is performed covering the physics of fatigue, fatigue assessment methods, residual stress formation process and the effect on fatigue life, and finally residual stress measuring and prediction methods.

2.1. Physics of fatigue

Prior to discussing the effect of residual stresses on fatigue life, the physics of fatigue will be addressed. Fatigue is defined as the process by which a crack originates and propagates under cyclic loading. When the crack reaches a critical size, sudden collapse, leakage or large deflections may occur. Fatigue cracks may occur at a loading magnitude of much less than the static design stress [7]. Fatigue life can be divided in two stages, namely a crack initiation and a crack propagation phase. Crack initiation occurs at the microscopic scale, where invisible cracks start to form in slip bands [21]. The crack propagation phase occurs at the macroscopic scale, where micro cracks continue to grow until failure [4, 21, 22]. The stages and events in each stage are illustrated in Figure 2.1.

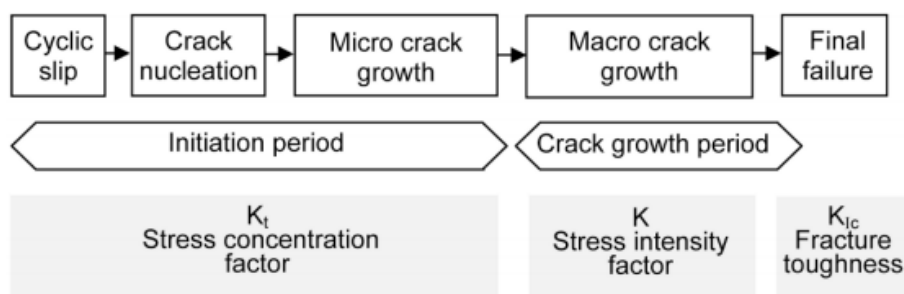


Figure 2.1: Phases of fatigue life [21]

In this section, the cyclic slip, crack nucleation and micro crack growth stages as shown in Figure 2.1 are explained. The fatigue process in this stage is described in detail in the paper of Sangid [22] and the book written by Schijve [21]. A summary of both references is given here. Crack initiation is formed due to the presence of initial dislocations, which are crystallographic defects, in the material. Dislocations move and multiply due to shear stresses and occur more at the material surface due to lack of constraints. The direction in which the defects move is close to 45° to the tensile direction, because it is primarily controlled by shear stress. When dislocations begin to glide after a critical shear stress is reached, it will continue during cyclic loading until an obstacle, for example a grain boundary, is reached. The strain concentrations at the grain boundaries is shown in the digital image correlation image in Figure 2.2. After further loading, the obstacle will be replaced by for example a kink or a cross-slip. During cyclic loading, the dislocations move along the same path, eventually forming persistent

slip bands, shown in Figure 2.3.

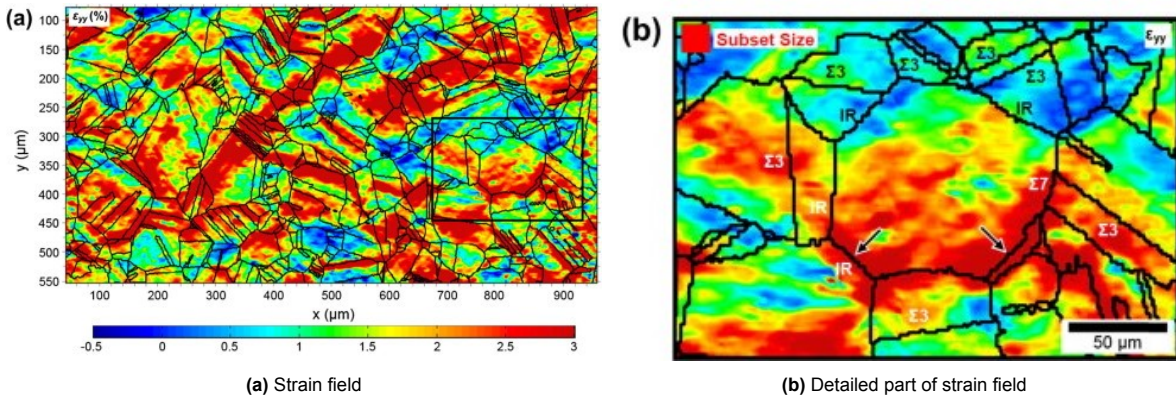


Figure 2.2: Strain field obtained from digital image correlation showing strain concentrations at the grain boundaries [22]

The dislocation density will increase, causing strain hardening. A stress concentration will also occur which causes slip in the neighbouring grain. Finally, when the cyclic plastic strain increases, the strain is localized in a small volume, resulting in initiation of micro-cracks. The micro-cracks grow due to tensile stresses. Because crack nucleation is dependent on the stress magnitude, an increase in stress due to geometric discontinuities or imperfections will reduce fatigue life. The stress concentration factor relates the stress at the hot spot to the nominal stress: $K_t = \frac{\sigma_{peak}}{\sigma_{nominal}}$.

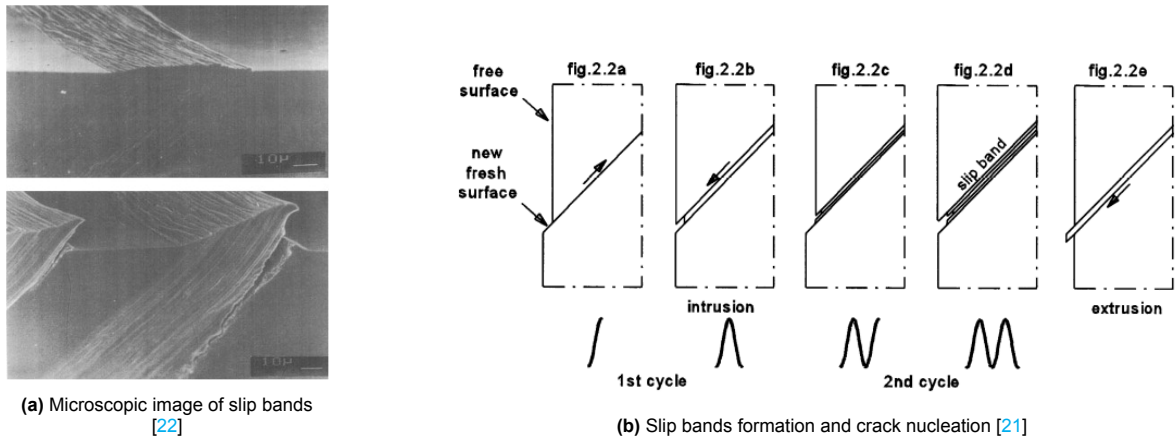


Figure 2.3: Microscopic image of slip bands and slip band formation due to cyclic slip

After the crack initiation stage, micro-cracks propagate or coalescence occurs until final failure. In this phase, the stress-state around the crack tip is related to the nominal stress by the stress intensity factor K (SIF). Fracture mechanics is the field of mechanics that studies the propagation of cracks. The relation between the crack growth rate da/dN and the stress intensity factor range ΔK is derived by Paris and Erdogan [23]. Paris' law is widely used to predict the crack remaining fatigue lifetime [22, 24, 21]. The relation is shown in equation 2.1 and in Figure 2.4.

$$\frac{da}{dN} = C(\Delta K)^m \tag{2.1}$$

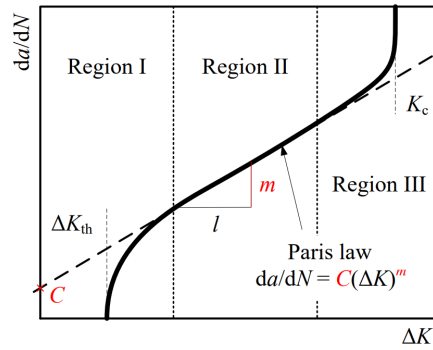


Figure 2.4: Paris' law [25]

2.2. Fatigue assessment methods

Several methods are available in the standards for fatigue resistance verification. Fatigue assessment of structural details can be done based on the nominal stress method, (geometric) hot-spot stress method or the effective notch stress method. Detail categories are available in NEN-EN1993-1-9 [13] and the IIW [26] recommendations. The Dutch national annex of NEN-EN1993-2 gives detail categories based on the nominal and hot-spot stress method for bridge details [27]. The ROK 2.0 [14] guideline gives additional bridge detail categories. The S-N curve of various detail categories in NEN-EN1993-1-9 is shown in Figure 2.5. The detail category $\Delta\sigma_c$ is defined as the stress range where the detail fails after $2E6$ cycles. The constant amplitude fatigue limit $\Delta\sigma_D$ is the stress range where the slope of the SN-curve changes from 3 to 5. The cut-off limit $\Delta\sigma_E$ is the stress range at which no fatigue damage occurs. The nominal stress method considers stress ranges in the undisturbed region, hot-spot stresses are the stresses at the weld toe due to geometric influences and effective notch stresses are stresses at notches with a radius of 1mm at the weld toe and root. Fatigue strength fulfills the requirements when the number of applied cycles does not exceed the number of cycles that can be resisted at the applied stress range. The number of cycles that can be resisted is obtained from the detail category and the slope of the SN curve. According to EN1993-1-9, the unity check for fatigue verification is calculated by equation 2.2.

$$\frac{\gamma_{Ff} \Delta\sigma_{E,2}}{\frac{\Delta\sigma_C}{\gamma_{Mf}}} \leq 1 \quad (2.2)$$

Where

- $\Delta\sigma_{E,2}$ = Equivalent applied constant amplitude stress range at $2E6$ cycles.
- $\Delta\sigma_C$ = Detail category. Stress range at which fatigue occurs after $2E6$ cycles.
- γ_{Ff} = Partial factor for equivalent stress range.
- γ_{Mf} = Partial factor for fatigue strength. The magnitude is depending on the assessment method (safe life or damage tolerant) and the consequence of failure.

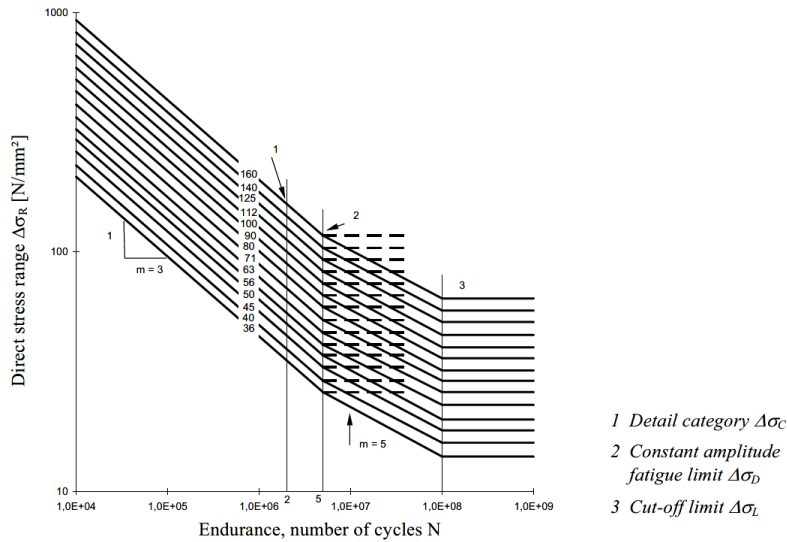


Figure 2.5: S-N curve in NEN-EN1993-1-9 with slope $m_1=3$ and $m_2=5$ [13]

In EN1991-2 [27], fatigue load models are given for bridge decks. The acting stress ranges can be obtained from simple hand calculation models or by FEA. Hot-spot stresses are determined by experiments or by extrapolating stresses obtained from FEA to the hot-spot.

2.3. Welding induced residual stresses

2.3.1. Formation process

During the welding process, the moving heat source causes high local temperatures. Due to the high temperature, the material expands. Because expansion is restrained by the surrounding, cooler, material, compressive stresses and plastic deformations develop. In Figure 2.6, plastic deformations are shown around the heat source, which moves from right to left. In front of the heat source, plastic compressive deformations develop, while plastic tensile deformations develop behind the heat source, due to restrained shrinkage during cooling [19]. The plastic shrinkage strains remain inside the weld, leading to residual tensile stresses [12]. The residual stress formation process is illustrated in Figure 2.7a and a general residual stress distribution in a butt weld in longitudinal and transverse direction is shown in Figure 2.7b.

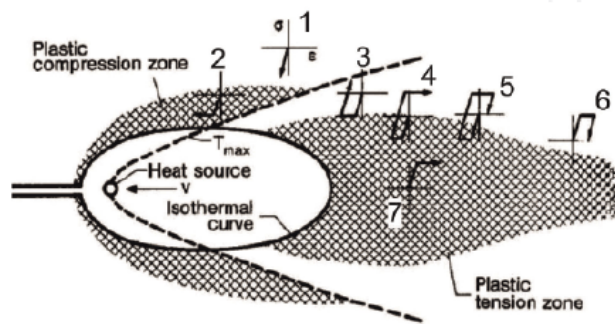
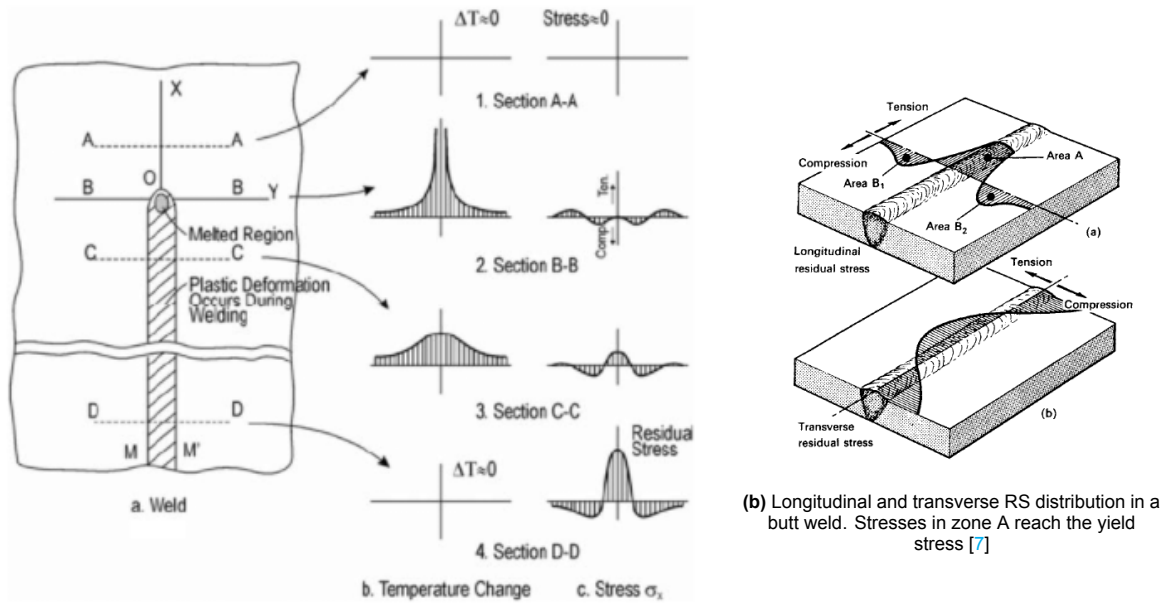


Figure 2.6: Local plastic deformations in the weld, HAZ and BM close to the heat source [19]



(a) Welding residual stress formation process [28]

Figure 2.7: Residual stress formation process and distribution in a butt weld

2.3.2. Effect on fatigue resistance

Tensile residual stresses have a detrimental effect on fatigue life by increasing the rate of crack growth in the crack initiation and propagation phase [5, 6, 29]. Residual compressive stresses have a beneficial effect on fatigue life [5, 7, 30]. Tensile residual stresses increase the mean of the effective stress range, defined as the superposition of the applied and residual stress range: $\sigma' = \sigma_{\text{applied}} + \sigma_{\text{residual}}$. The tensile part of the effective stress range contributes to fatigue damage [31]. This means that even when the applied stress range is entirely compressive, fatigue damage can occur even when the structure is only loaded in compression. In Figure 2.8, the effective stress range is illustrated for various internal stress conditions combined with a tension only fatigue loading. In design standards such as Eurocode 3 part 1-9 [13], the level of residual stress close to the yield stress is considered, but not the actual stress or the effect of the mean stress [30, 32]. When the mean stress is compressive, the Eurocode fatigue life estimate is conservative.

2.3.3. Relaxation

As mentioned in the previous section, the residual stress distribution has a large influence on fatigue resistance and should be considered in fatigue assessment. Stresses are tensile at some locations along the weld seam, while compressive stresses are present at the other locations along the weld seam and in the through thickness direction. Overall, the residual stresses are self-equilibrating. Due to fatigue loading, such as a local wheel load on a bridge deck, further plastic deformations will occur which results in a redistribution and relaxation of residual stresses [33]. The relaxation phenomenon makes the actual stress distribution harder to predict. Xie et al. [34] performed fatigue experiments on a small welded specimen made of 316L stainless steel and concluded that 45-60% of the maximum residual stresses were released during the first cycle with a further decrease in the subsequent cycles. The drastic relaxation is however limited to the first few cycles. In addition to experiments, the researchers proposed an analytical model to predict the relaxation which has been verified by the experimental data. Limited studies are however available on the relaxation of WRS. It is a complex phenomenon that is dependent on many factors including loading scenario, number of cycles and material properties [35].

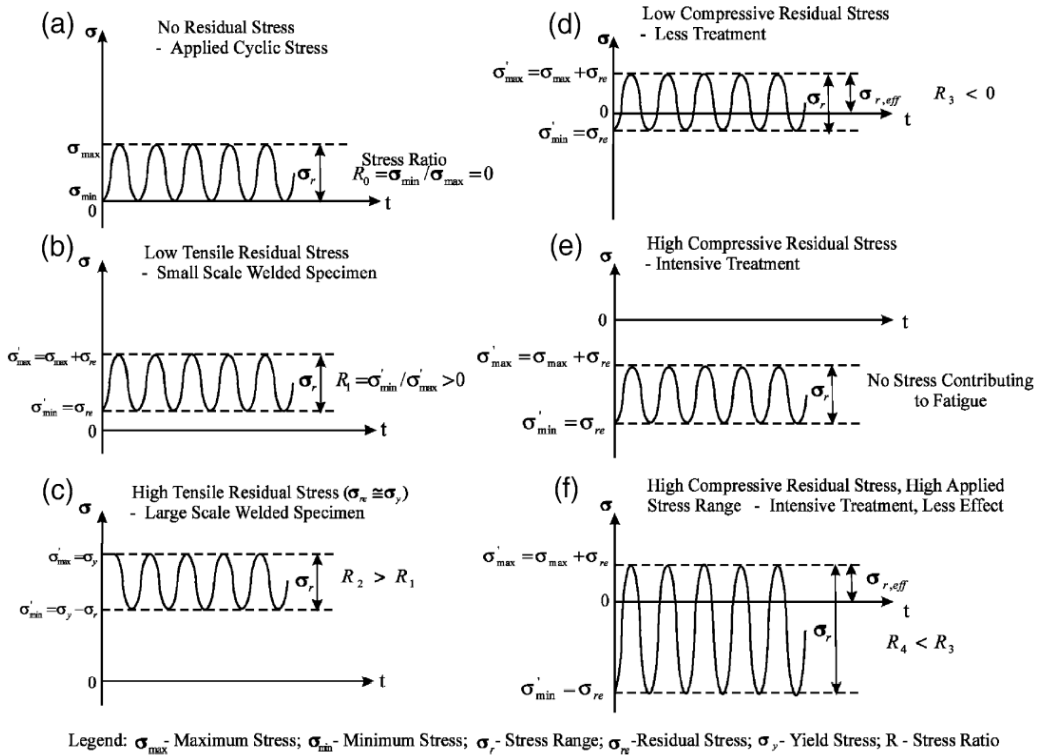


Figure 2.8: Effect of superposition of residual and applied stress range on the effective stress range [31]

2.3.4. Measurement methods

Many methods for measuring residual stresses have been developed in the past. These methods can be divided in a non-destructive category as well as a destructive category. An overview of methods found in the literature is shown in Table 2.1 [36, 17].

Table 2.1: Residual stress measuring methods [36]

Destructive methods	Nondestructive methods
Sectioning method	Barkhausen noise method
Contour method	Ultrasonic method
Hole-drilling method	X-ray and neutron diffraction method
Instrumented indentation method	

The destructive methods are based on the principle of making cuts in the material and measuring the deformations (relaxations). The most widely used method is the hole-drilling method. This method involves drilling a small hole in the surface and measuring the relaxation by strain gauges around the hole. This method is relatively cheap, has good reliability, has standardized procedures (ASTM E-837-08 [37]), is convenient to use and causes minimal damage [17]. However, the method can only be applied when the material behaviour is linear elastic. In practice, sufficiently accurate results are found when residual stresses do not exceed 60% of the yield strength [37]. Local plastic deformations occur due to welding. To overcome this, a correction procedure was developed by van Puymbroeck [6] by simulating the hole-drilling procedure with FEM.

The ASTM [37] standard provides equations to compute uniform stresses from the measured strains in a thin workpiece ($t < 0.4D$) with uniform stresses. In the workpiece, a hole is drilled through the entire thickness. Calibration constants \bar{a} and \bar{b} are provided in tables to account for the type of strain gauge rosette and hole diameter. The different types of strain gauge rosettes are shown in Figure 2.10a. In addition, equations to compute stresses within each hole depth in a thick workpiece are given.

Vishay [38] proposed that the equation for computing residual stresses in thin workpieces can be applied for thick workpieces as well when appropriate blind hole calibration constants are used. The calibration constants must then be obtained from experiments or numerical methods in contrary to theoretical considerations. The equations for calculating the maximum and minimum principle stress and their direction are given in Equation 2.3 [38, 39]. The direction is defined in Figure 2.10b.

The ASTM standard [37] recommends hole-drilling devices that drill a hole with a speed of 50000 to 400000 rpm to prevent machining-induced residual stresses. Standard hole-drilling devices are available such as the SINT MTS3000 and the Micro-Measurements RS-200 shown in Figure 2.11.

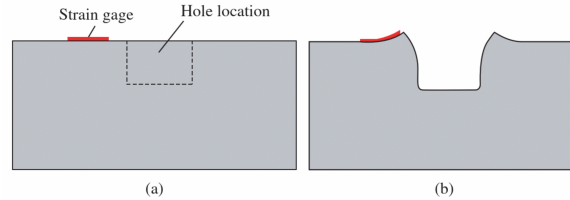


Figure 2.9: Local deformation after drilling a hole in a material with tensile residual stresses [17]

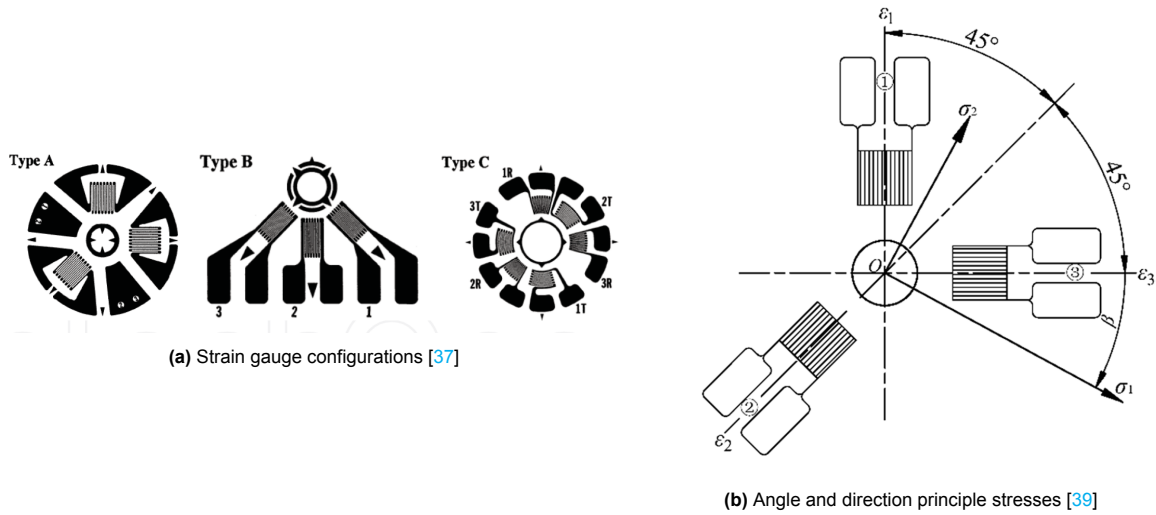


Figure 2.10: Strain gauge configurations and direction and angle of of principle stresses

$$\sigma_{1,2} = \frac{\epsilon_1 + \epsilon_3}{4A} \mp \frac{\sqrt{(\epsilon_3 - \epsilon_1)^2 + (\epsilon_1 + \epsilon_3 - 2\epsilon_2)^2}}{4B}, \quad (2.3)$$

$$\beta = 1/2 \arctan\left(\frac{\epsilon_1 - 2\epsilon_2 + \epsilon_3}{\epsilon_3 - \epsilon_1}\right)$$

Where

- $\sigma_{1,2}$ are the minimum and maximum principle stress
- β is the direction angle of the principle stress, defined in Figure 2.10b
- $\epsilon_{1,2,3}$ are measured strains in directions 0° , 45° and 90°
- A,B are calibration constants

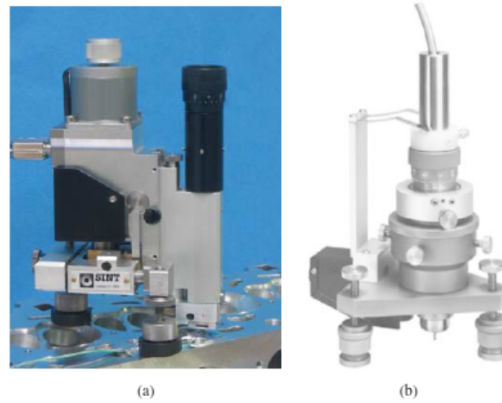


Figure 2.11: Hole drilling devices. (a) SINT MTS3000 and (b) Micro-Measurements RS-200 [17]

Diffraction methods are nondestructive methods which measure the distance between atomic planes in crystalline or poly-crystalline materials. When an X-ray beam, for example, is sent to the specimen, the beam is then diffracted from the specimen. By measuring the angle of diffraction, the distance between atomic planes can be calculated by Bragg's law, as shown in Equation 2.4. The distance between the diffracting planes d gives an indication of the strain in the material. The stresses can then be obtained by Hooke's law.

$$n\lambda = 2d \sin \theta \quad (2.4)$$

Where:

- θ is the diffraction angle
- λ is the wavelength
- n is an integer
- d is the distance between diffracting planes.

Other available non-destructive methods are magnetic, ultrasonic, thermoelastic or indentation methods. However, because the hole-drilling is the most practical and widely applied, these methods will not be further elaborated [17].

2.3.5. Prediction models

Measuring residual stresses can be very costly and time consuming. Furthermore, when nondestructive methods are preferred, the scale and mass of the specimen is limited. Therefore, numerical methods are used to predict residual stresses. Predicting welding induced residual stresses can be very challenging. The arc physics, fluid flow, phase transformations, grain size and deformations are complex phenomenon and difficult to model [19, 18]. The residual stresses can be considered at the macroscopic or microscopic level. At the macroscopic level, the problem can be considered a thermo-mechanical problem. At this level, the transient temperature, stress and strain will be computed. At the microscopic level, phase transformations, dissolution and precipitation will occur. Complex interactions occur between the thermal, mechanical, metallurgical and fluid processes. For engineering purposes, only the macroscopic level is being considered [36]. In most welding simulations found in the literature, the real heat source is substituted by an equivalent heat source distribution. Various distributions have been proposed including a Gaussian surface flux, hemi-spherical power density and the Goldak [20] double ellipsoid heat source model (DEHSM).

The Goldak DEHSM is shown in Figure 2.12. The power distribution at the front and back of the heat source are described by Equation 2.5 and 2.6, respectively. The Goldak DEHSM is used in most welding simulations found in the literature among which Gu et al. [39], Spyridoni [40] and van den Berg [29].

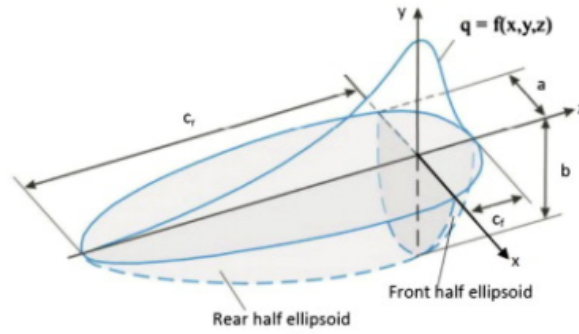


Figure 2.12: Goldak double ellipsoid heat source model and parameters [41]

$$q_f(x, y, z, t) = \frac{6\sqrt{3}f_f Q}{abc_f \pi \sqrt{\pi}} \exp\left(-3\left(\frac{x^2}{a^2} + \frac{y^2}{b^2} + \frac{z + v(\tau - t)^2}{c_f^2}\right)\right) \quad (2.5)$$

$$q_r(x, y, z, t) = \frac{6\sqrt{3}f_r Q}{abc_r \pi \sqrt{\pi}} \exp\left(-3\left(\frac{x^2}{a^2} + \frac{y^2}{b^2} + \frac{z + v(\tau - t)^2}{c_r^2}\right)\right) \quad (2.6)$$

Where:

- q_f and q_r are the power densities for the front and rear ellipsoid in $\frac{W}{m^3}$
- a, b are width and depth parameters that can be taken as half the width of the weld and the depth of the molten zone, respectively.
- f_f, f_r are input parameters for the fraction of the power in each ellipsoid. The sum $f_f + f_r$ is equal to 2.
- c_f, c_r are the length of the front and rear ellipsoid and can be taken as $c_f = a$ and $c_r = 2.33a$
- v is the welding speed
- τ is the time lag factor

The heat transfer simulation can be performed in the commercially available FE-software Abaqus ©. The solid body heat conduction analysis is based on the basic energy balance shown in Equation 2.7 [42]. This equation is generally written in terms of specific heat $c(\theta) = \frac{dU}{d\theta}$ in $\frac{J}{kg \cdot K}$ and heat conduction $f = -k \frac{\partial \theta}{\partial x}$, where k is the conductivity in $\frac{W}{m \cdot K}$. Boundary conditions can be a prescribed temperature, body or surface heat flux, surface convection and radiation. Surface convection and radiation are based on Newton's cooling law, shown in equation 2.8, and the Stefan Boltzman law shown in equation 2.9, respectively.

$$\int_V \rho \dot{U} dV = \int_S q dS + \int_V r dV \quad (2.7)$$

Where

- V is the volume of the material
- ρ is the density
- \dot{U} is the material time rate of internal energy
- S is the surface area
- q is the heat flux per unit area of the body, flowing into the body
- r is the heat supplied internally into the body per unit volume

$$q = h(\theta - \theta^0) \quad (2.8)$$

Where:

- h = the film coefficient in $Wm^{-2}K^{-1}$
- θ^0 = the sink temperature

$$q = \epsilon \cdot \sigma \cdot ((\theta - \theta^Z)^4 - (\theta^0 - \theta^Z)^4) \quad (2.9)$$

Where:

- ϵ = is the emissivity
- σ = The Stefan Boltzman constant: $5.67 * 10^{-8} Wm^{-2}K^{-4}$
- θ^Z is the absolute zero temperature

Finally, the placement of the filler material can be simulated in Abaqus by the model change command from the interaction module. Initially, the weld elements are deactivated. The elements are subsequently step-by-step reactivated while the heat source moves over the weld material. This step-by-step procedure is generally referred to the birth/dead principle in the literature and has been applied by many researchers including Xin and Veljkovic [43], Spyridoni [40] and van den Berg [29].

2.4. Experimental and numerical results

2.4.1. Hole-drilling method

Hole-drilling measurements on a 8.2m x 4.1m bridge deck specimen were performed in the pHd research by van Puymbroeck [44]. The specimen was made of S235 and had 6 closed trapezoidal longitudinal and 4 transverse stiffeners. Because hole-drilling is a linear-elastic measurement method, reliable results were only achieved up to 80% of the yield strength. A correction procedure was performed based on a simulation of the hole-drilling procedure. Holes up to a depth of 1mm were drilled at 22 locations on the deck plate and stiffener. Tensile stresses up to the yield stress were found in longitudinal direction close to the weld. The obtained results were similar to FEM results. Compressive stresses of the FEM results were found larger than hole-drilling results. Deviations were explained by the fact that stresses were measured near the yielding zone, which results in a larger error margin with the hole-drilling method. Other explanations were errors in hole-drilling execution, such as measurement location misalignment and the smaller size of the numerical model.

Gu et al. [39] measured residual stresses in a segment of an orthotropic steel deck by the hole-drilling method and compared the values to results of a thermo-numerical welding simulation with the Goldak DEHSM. The results showed peak values of around the yield strength in the weld direction. The values reduce to compressive values of around 15% of the yield stress in approximately 50mm. The experimental model is shown in Figure 2.13 and the stresses in the direction of welding in Figure 2.14.

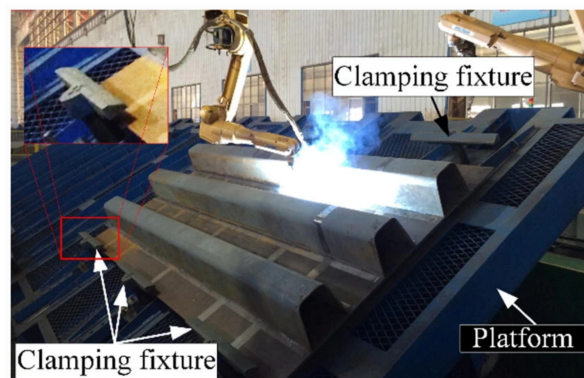


Figure 2.13: Welding setup of a specimen consisting of a deck plate and three ribs [39]

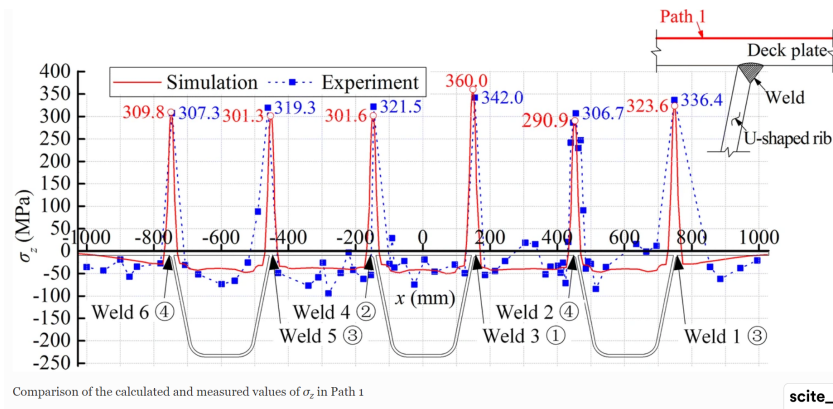


Figure 2.14: Results from hole-drilling measurements in and comparison with numerical simulation of the specimen by Gu et al. [39]

2.4.2. Distortion measurements

Spyridoni [40] validated a numerical welding simulation model by thermal measurements and welding distortion measurements on a T-connection. Distortion measurements of various points on the T-connection were performed by a laser sensor, shown in Figure 2.15a. Predicted values found good agreement with experimental results. The depth parameter in the Goldak DEHSM was altered to obtain better agreement. After validation, a welding simulation of a part of a OSD was performed. Tensile residual stresses close to the yield strength were found. The residual stress distribution in the welding direction was similar to results found by Gu et al. [39] in Figure 2.14 and to results by predicted and HDM values by van Puymbroeck [6].

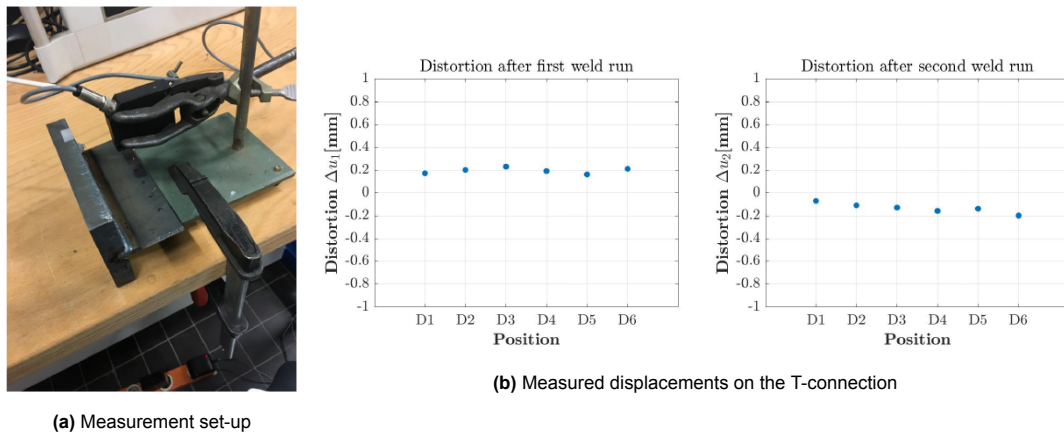


Figure 2.15: Distortion measurements by Spyridoni [40]

Measurements of welding distortions are useful to validate numerical models. Furthermore, distortions will decrease the strength of joints and reduce the accuracy in assembly [1]. Therefore, two other welding distortion measurement methods found in the literature are presented.

Deng et al. [1] measured and simulated welding distortion of a 3m x 1.5m specimen shown in Figure 2.16a. Coordinates were tracked by a 3D photography technique to determine the deformations. The results along line 1 and 2 are shown in Figure 2.16. Along line 2, the sides of the plate moved upwards to 8mm relative to the location of the weld. A numerical simulation based on a thermo-mechanical analysis with the Goldak DEHSM was performed. The obtained displacements found good correspondence with the experimental results.

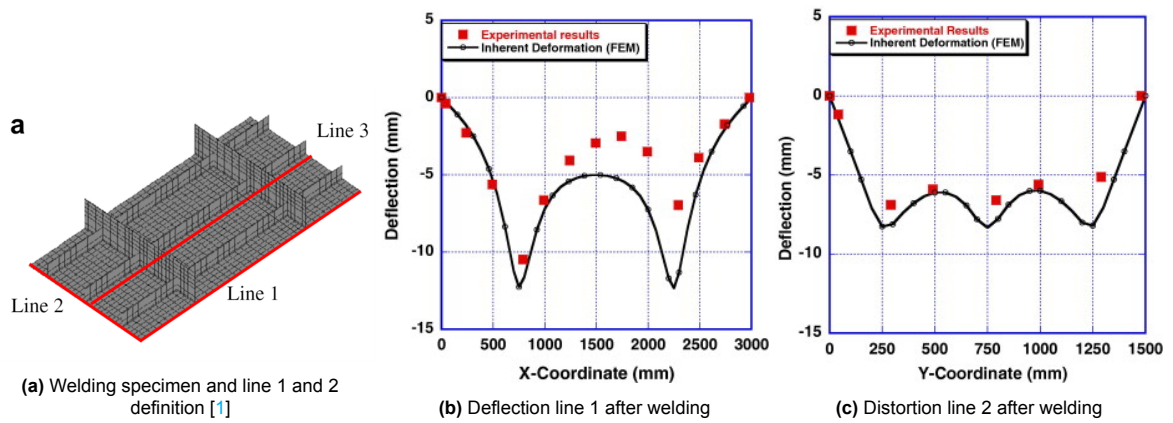


Figure 2.16: Deflection along line 1 and 2 after welding [1]

Sim et al. [9] measured welding distortions of various points on a 10x3m bridge deck with four transverse stiffeners by a laser tracking system. The OSD is shown in Figure 2.17a. The results are shown in Figure 2.17b. Upward displacements of 10 mm of the sides of the deck plate were found in transverse direction.

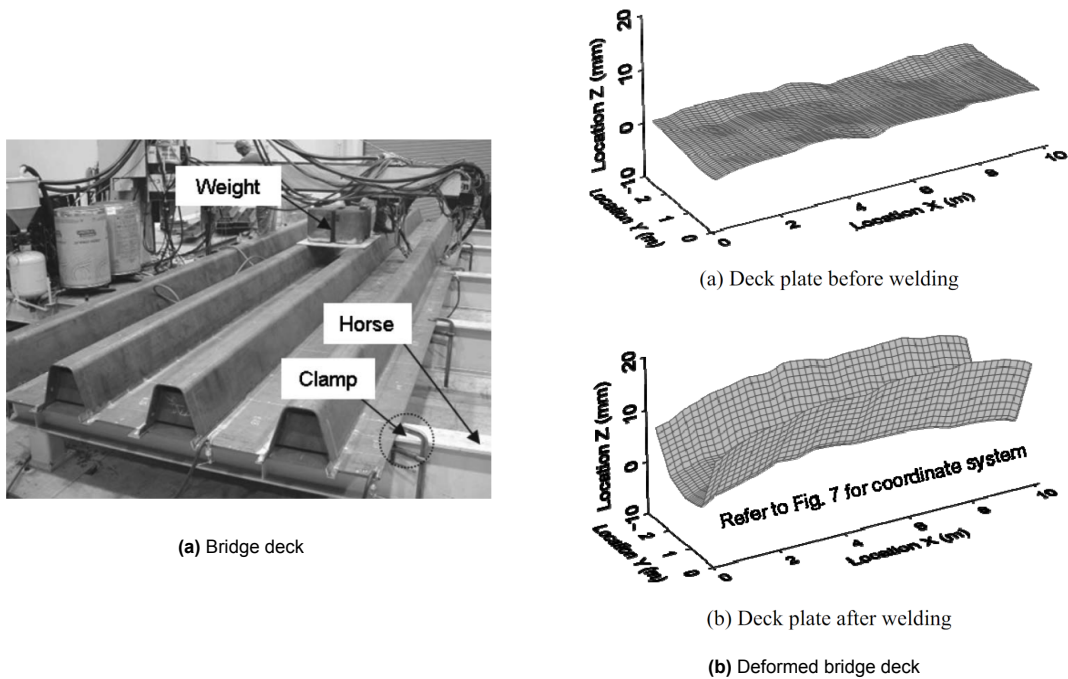


Figure 2.17: Distortion after welding [9]

3

Welding experiment

3.1. Introduction

In the previous chapter, it was concluded that the residual stress distribution has a large influence on fatigue life. Incorporating residual stresses in fatigue life prediction models is required to improve their accuracy. The distribution depends on many factors including welding parameters, welding speed, resulting weld geometry and the chemical composition of steel. Not all parameters can accurately be determined and included in numerical welding simulation models. Therefore, simplifications and assumptions need to be made [3]. To gain confidence in the chosen assumptions and simplifications, experimental validation is required. In this chapter, a welding experiment on a segment of an OSD is performed. The main objective is to create a database of temperature gradients and welding distortions to optimize welding processes, control distortions and validate welding and fatigue life prediction models. The second objective is to establish an experimental methodology for obtaining welding distortions by use of a handheld 3D scanner. In Chapter 4, a numerical model of the welding experiment will be made and results will be validated with the obtained experimental results. A paper about this experiment has been published in the IABSE 2022 conference proceedings and can be found in Appendix A.

3.2. Specimens, equipment and experimental set-up

Three specimens were fabricated at steel constructor Hollandia Infra in Krimpen aan den IJssel. The specimens represented a segment of an OSD and consisted of a deck plate, a trapezoidal stiffener and a crossbeam web with a Haibach cope hole. The dimensions are shown in Figure 3.1a. The specimens were made out of S355J2+N. The welding procedure was gas metal arc welding (GMAW). The shielding gas consisted 80% out of Argon and 20% out of CO₂. The gas flow rate was between 15 and 20 L/min. The used filler wire type was Diamondspark® 52RC (1.2mm) for the vertical passes and Outershield® MC715H (1.2mm) for all other passes, except for Specimen 2, where Diamondspark 52RC was used for all passes.

Thermal measurements were performed by a FLIR® E96 thermal camera and was placed on a tripod during the experiment as shown in Figure 3.1b. The camera had a resolution of 640x480 pixels. Radiometric video was recorded, meaning that each pixel in each frame contained a temperature reading. The accuracy of the results is $\pm 2\text{ }^{\circ}\text{C}$ or $\pm 2\%$ of the reading, according to the manufacturer [45]. Three temperature recording ranges could be selected, $-20\text{-}120\text{ }^{\circ}\text{C}$, $0\text{-}650\text{ }^{\circ}\text{C}$ and $300\text{-}1500\text{ }^{\circ}\text{C}$. The temperature ranges $0\text{-}650\text{ }^{\circ}\text{C}$ and $300\text{-}1500\text{ }^{\circ}\text{C}$ were used during the experiment to capture the entire temperature range. During welding, the sensor was covered to protect it from the high radiation emitted by the welding torch. After welding, the sensor was uncovered to measure the temperature directly after welding.

The Artec® LEO handheld 3D scanner, shown on the workbench in Figure 3.1b, was used to measure the geometry of the specimens before and after welding. Distortions were obtained by comparing the geometry scans before and after welding. It captures up to 3 million data points per second with an

accuracy of up to 0.1mm [46]. Frames are reconstructed from these points, from which a 3D model is made. The HD scanning algorithm was enabled, which uses more polygons per frame for data processing, leading to denser and higher quality 3D data. A 3D resolution of up to 0.2 mm can be achieved with this mode. In the scanner settings, HD mode was enabled and set to 1/8, meaning that for every 8 frames, one frame was reconstructed in HD mode [47].

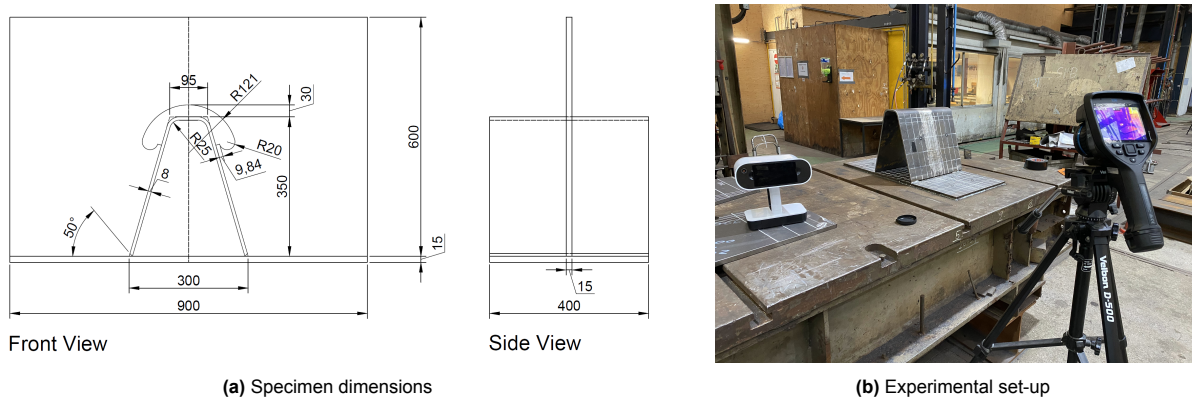


Figure 3.1: Specimen dimensions and experimental set-up

3.3. Experimental procedure

The actions performed during the experiment are given in chronological order in Table 3.1. The welding passes are defined in Figure 3.3a. Before welding, the sides of the deck plate were welded to the workbench to simulate neighbouring bridge deck behaviour. Due to flexibility of the deck plate in a full-scale bridge deck, these welds between the workbench and deck plate led to over constraint. Therefore, for Specimen 3, the welds of 400 mm long were removed, and the effect of the boundary conditions was investigated.

The tack welds before welding and after fitting the crossbeam are shown in Figure 3.2. Lengths and distances are rounded. The length of the tack welds in Figure 3.2a varied with ± 3 mm. Pictures of the welds can be found in Figure 3.6. The measured weld geometry is shown in Figures 3.7 and 3.8. The distance Y is given in Figure 3.2b. This distance varies per specimen. The exact location and length of the tack welds of Specimen 2 & 3 are given in Appendix F. Specimen 1 was not scanned after fitting the crossbeam, so no exact dimensions are known.

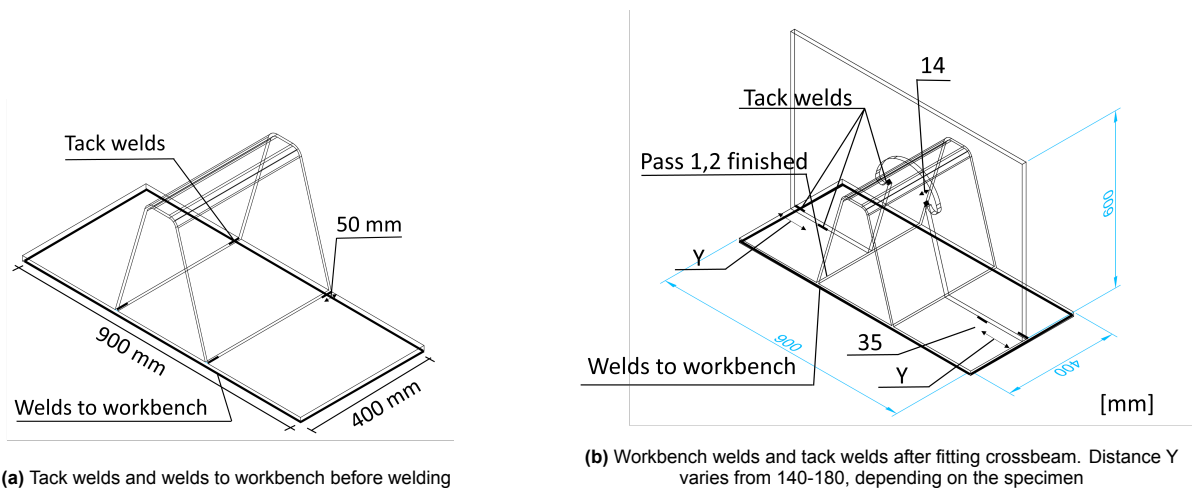
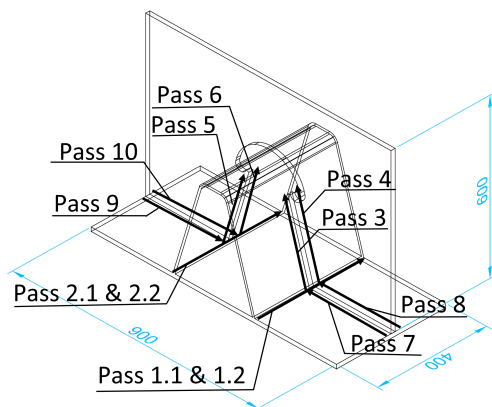


Figure 3.2: Location and length of tack welds before welding and after fitting crossbeam

Table 3.1: Experimental procedure

Step	Action	Explanation
1	Draw grid lines on the specimen	This helps to identify possible misalignment of frames in post-processing.
2	Weld the sides of the deck plate to workbench	
3	Place tack welds of approx. 50mm	See Figure 3.2a
4	Scan 3D geometry	
5	(Specimen 3) remove workbench welds of 400mm	
6	Weld passes 1.1-2.2	See Figure 3.3a. Pass 1.1 and 2.1 are filling passes in between the tack welds, while 1.2 and 2.2 are capping passes
7	Scan 3D geometry	
8	Fit crossbeam, place tack welds	See Figure 3.2b
9	Scan 3D geometry	
10	Weld passes 3-10	See Figure 3.3a
11	Scan 3D geometry	
12	Remove welds connecting the deck plate to workbench	
13	Scan 3D geometry	



(a) Welding passes



(b) Finished specimen

Figure 3.3: Welding passes definition and welded specimen

The documented welding- and cooling time, power input and wire feeding speed, as well as temperature recording range of Specimen 1 are shown in Table 3.2. This data will be used in the numerical model in Chapter 4. The documentation of Specimen 2 and 3 are given in Appendix F.

Table 3.2: Documentation specimen 1

Action	Duration [mm:ss]	Voltage [V]	Current [A]	Wire feeding speed [mm/min]	Wire type	Recorded temp range [°C]
Pass 1.1	00:45	26.2	251	9.5	MC715H	0-650
Cooling 1.1	02:14					
Pass 1.2	01:10	26.2	251	9.5	MC715H	0-650
Cooling 1.2	06:00					
Pass 2.1	00:46	26.2	251	9.5	MC715H	0-650
Cooling 2.1	02:39					
Pass 2.2	01:15	26.2	251	9.5	MC715H	0-650
Cooling 2.2	25 days					
Pass 3	01:29	23.2	238	8.5	52RC	300-1500
Cooling 3	02:56					
Pass 4	01:13	23.2	238	8.5	52RC	300-1500
Cooling 4	12:07					
Pass 5	01:21	23.2	238	8.5	52RC	300-1500
Cooling 5	02:37					
Pass 6	01:20	23.2	238	8.5	52RC	0-650
Cooling 6	22:00					
Pass 7	01:02	26.2	274	10.5	MC715H	300-1500
Cooling 7	02:22					
Pass 8	00:58	26.2	274	10.5	MC715H	300-1500
Cooling 8	03:56					
Pass 9	00:58	26.2	274	10.5	MC715H	300-1500
Cooling 9	01:16					
Pass 10	00:59	26.2	274	10.5	MC715H	300-1500

3.4. Data processing

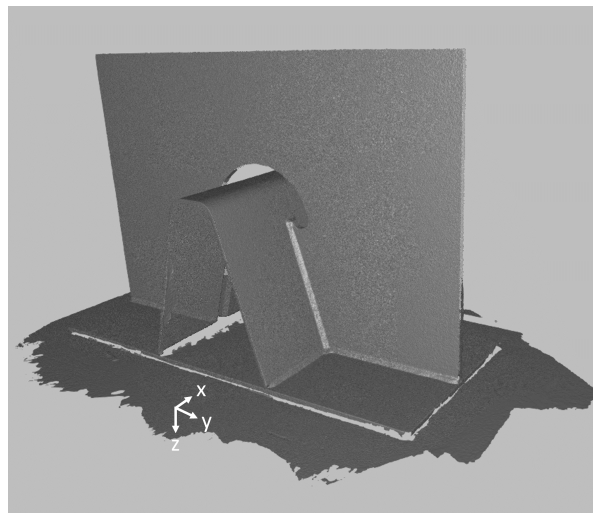
Radiometric video has been processed in FLIR research studio 2.0 software [48]. In the software, thermal images of each frame can be exported, and the temperature range and colour palette can be changed. Various regions of interest (ROI) can also be defined, such as a point, a line, a rectangle or a circle. Temperature values 1.8 seconds after welding along a line perpendicular and parallel to Pass 1.1 have been exported, as well as a maximum temperature as a function of time in a box around the melting pool.

The geometry scans were post-processed in the Artec Studio 16 Professional software [47]. The post-processing steps and settings are given in Table 3.3. The resulting 3D model after welding and after releasing constraints consisting of 74 million polygons is shown in Figure 3.4. The location of the coordinate system is also shown.

Table 3.3: Post-processing steps & settings in Artec Studio Professional 16, see documentation [47]

Step	Function	Settings & Explanation
1	Import scan	Set HD data density to 4x.
2	Global registration	This algorithm converts all one-frame surfaces into a single coordinate system - Features: Geometry & texture - Search features within: 5 mm
3	Outlier removal	Removes 3D noise - 3D noise level: 3 - Resolution: 0.2mm
4	Sharp fusion	This fuses all frames in a single polygonal 3D model - 3D resolution: 0.2 mm - Fill holes with radius ≤ 5 mm
5	Positioning tool	Rough positioning tool - Specify three points on workbench surface to specify the XY plane. - Invert z-axis
6	Transformation tool	Translate and rotate the model to align the coordinate system more precisely to the location shown in Figure 3.4
7	Export meshes	Export an .stl file containing coordinates of all polygonal nodes in mm

With the NumPy-stl package in Python [49], the z-coordinates of the polygonal nodes were extracted from the .stl file and plotted along three paths. The paths are defined in Figure 3.12b. For Path 1, coordinates with x-values between 20 and 21mm from the plate edge were extracted. For path 2, coordinates with y-values between 10 and 11mm from the weld toe were extracted and for Path 3, coordinates with y-values between 10 and 11mm from the plate edge were extracted. The raw data was filtered in Python with the Savitzky-Golay algorithm [50].

**Figure 3.4:** Specimen 1 after sharp fusion and location of coordinate system

Detailed images of the weld geometry from the 3D scan in Artec studio are shown in Figure 3.5 and corresponding pictures are shown in Figure 3.6 for comparison. The location of the tack weld of Specimen 3 shown in Figure 3.5b was 30mm from the deck plate edge. The other tack welds in Specimen 3 and in the other specimens were between 5 and 15mm from the plate edge.

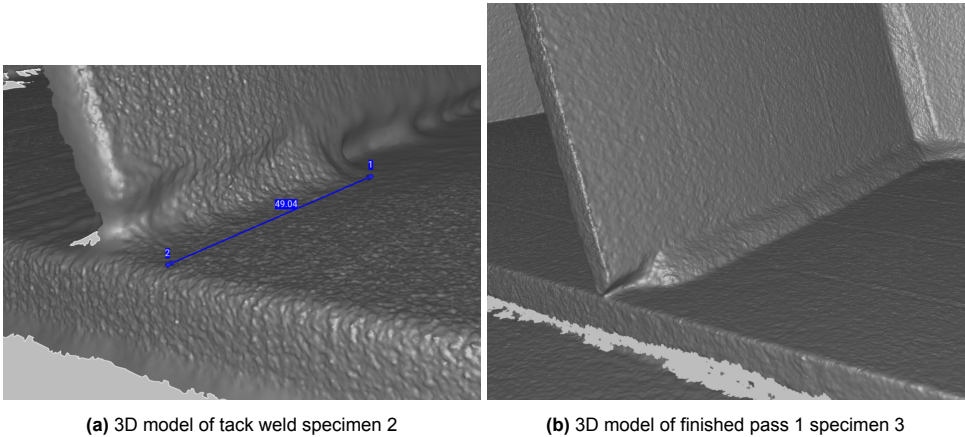


Figure 3.5: Weld geometry captured by the scanner

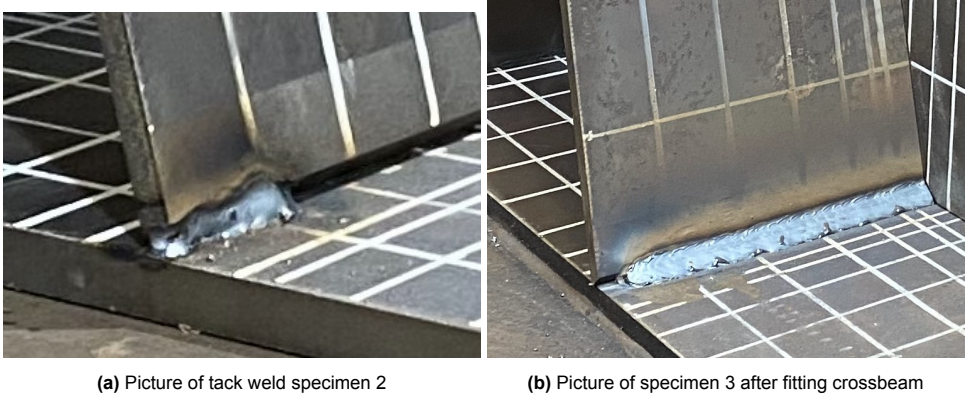


Figure 3.6: Picture of welds for comparison with scan

The dimensions of the tack weld and the capping pass at the rib-to-deck connection in Specimen 1 are shown in Figure 3.7.

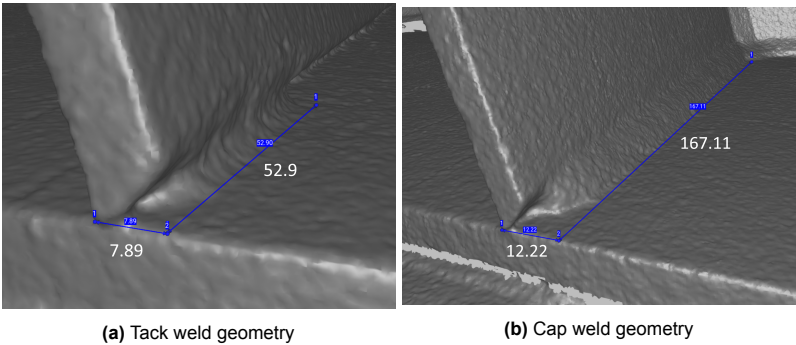


Figure 3.7: Weld geometry at the rib-to-deck connection of Specimen 1 (mm)

The weld geometry around the copehole and at the crossbeam-to-deck connection are shown in Figure 3.8.

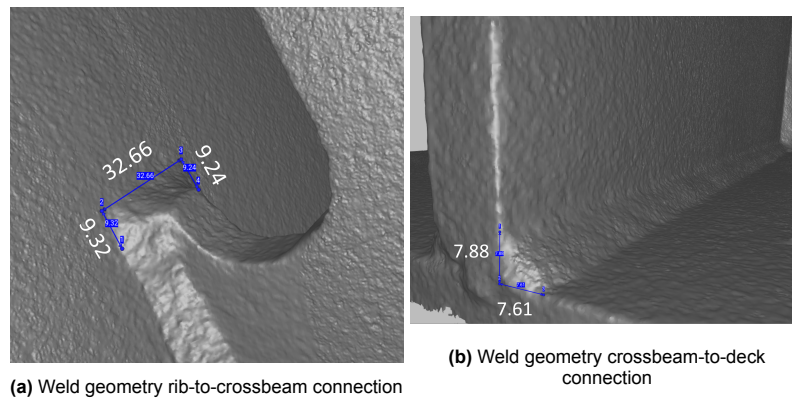


Figure 3.8: Weld geometry at the rib-to-crossbeam and crossbeam-to-deck connection of Specimen 1 (mm)

3.5. Results

3.5.1. Temperature

A thermal image 1.8s after pass 1.1 in Specimen 3 is shown in Figure 3.9. The maximum recorded temperature was 1042 °C, which is around the melting point of steel. In the figure, the coordinate system is defined, where the x-direction is parallel to Pass 1.1 and the y-direction is perpendicular to that. The box B1 around the melting pool has also been defined.

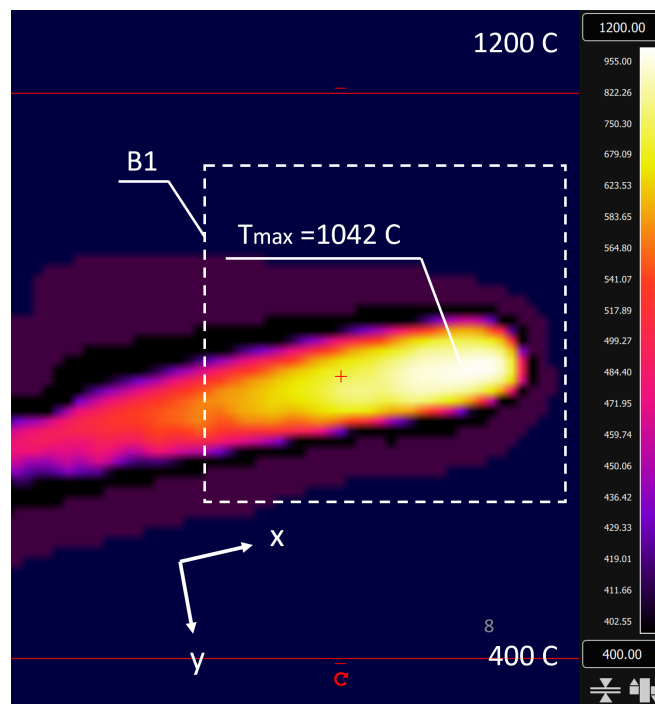
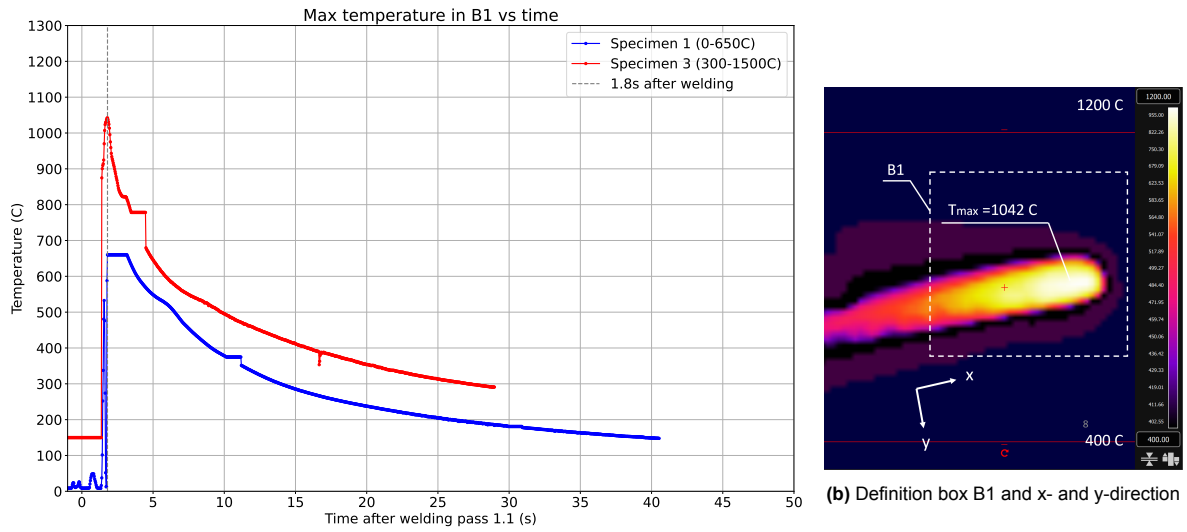


Figure 3.9: Thermal image specimen 3 1.8s after welding

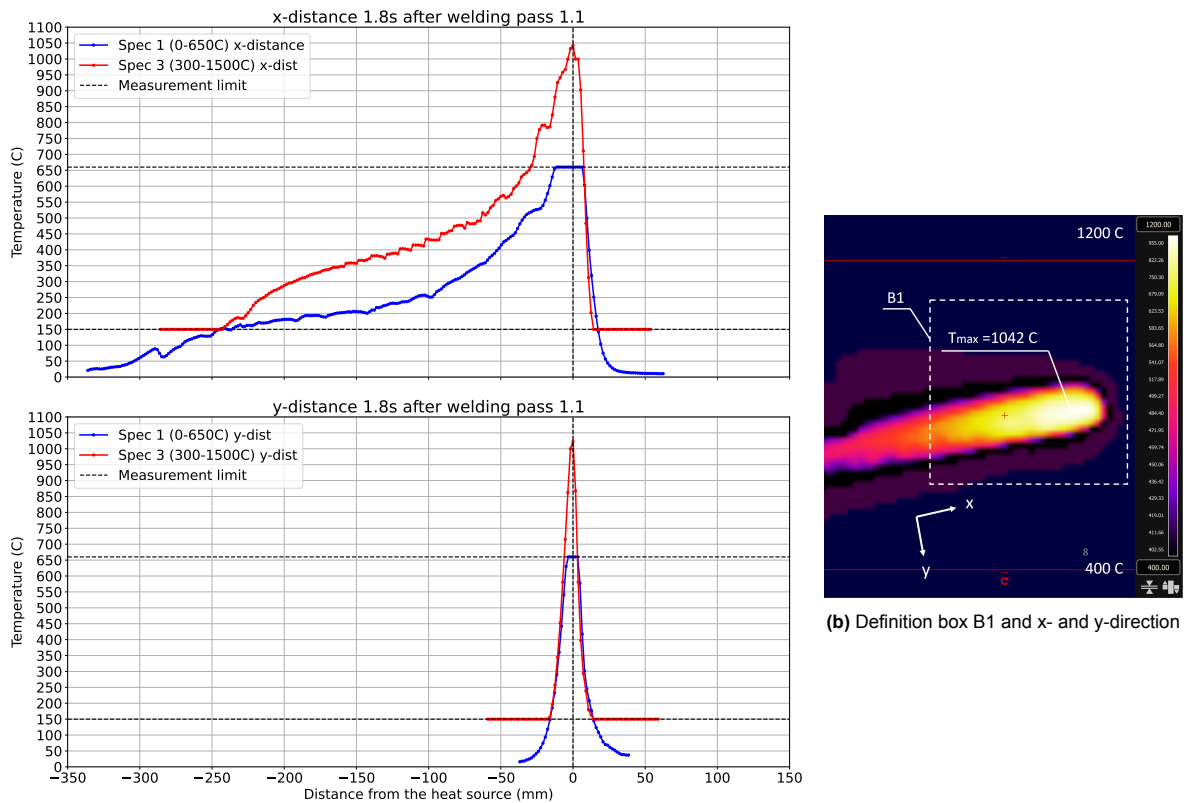
The maximum temperature in box B1 as a function of time is shown in Figure 3.10a. The temperature distribution around the last position of the heat source 1.8s after welding is shown in Figure 3.11a. While the temperature recording range was set to 300-1500C for Specimen 3, values up to 150C were recorded. Values in Specimen 3 are significantly larger at a distance of -250 to -50 mm from the heat source compared to Specimen 1. In Specimen 1, the measured values are closer to the expected values. Both recording ranges have an accuracy of $\pm 2\%$, according to the manufacturer [45]. Focusing issues might occur in the high temperature recording range, or the camera is not well calibrated for

recording temperatures below 600°C. The range requires special attention and a double-check with alternative equipment.



(a) Temperature at distance x and y from the heat source 1.8s after welding and maximum temperature vs time in specimen 1 and 3

Figure 3.10: Temperature distribution and thermal image specimen 3 1.8s after welding



(a) Temperature at distance x and y from the heat source 1.8s after welding

Figure 3.11: Temperature distribution and thermal image specimen 3 1.8s after welding

3.5.2. Distortions

The raw data of the z-coordinates of the top of the deck plate along the three paths is shown in Appendix B. The scatter was approximately 0.25 mm. In post-processing, the data points at the location of the stiffener were removed. With the Savitzky Golay algorithm [51], a 3rd degree polynomial was fitted in a sampling window. It was found that a window size of 1999 points in Path 1 showed a smooth curve without losing meaningful data. For Path 2 & 3, a window size of 599 points was used. The resulting geometry of Path 1 is shown in Figure 3.12 and the geometry of Path 2 & 3 in Figure 3.13 and 3.14, respectively. The top figure shows the geometry with a large z-axis scale, while only a small scale is presented in the bottom figure. Geometry of Specimen 2 has not been considered due to misalignment of frames in the scan after welding.

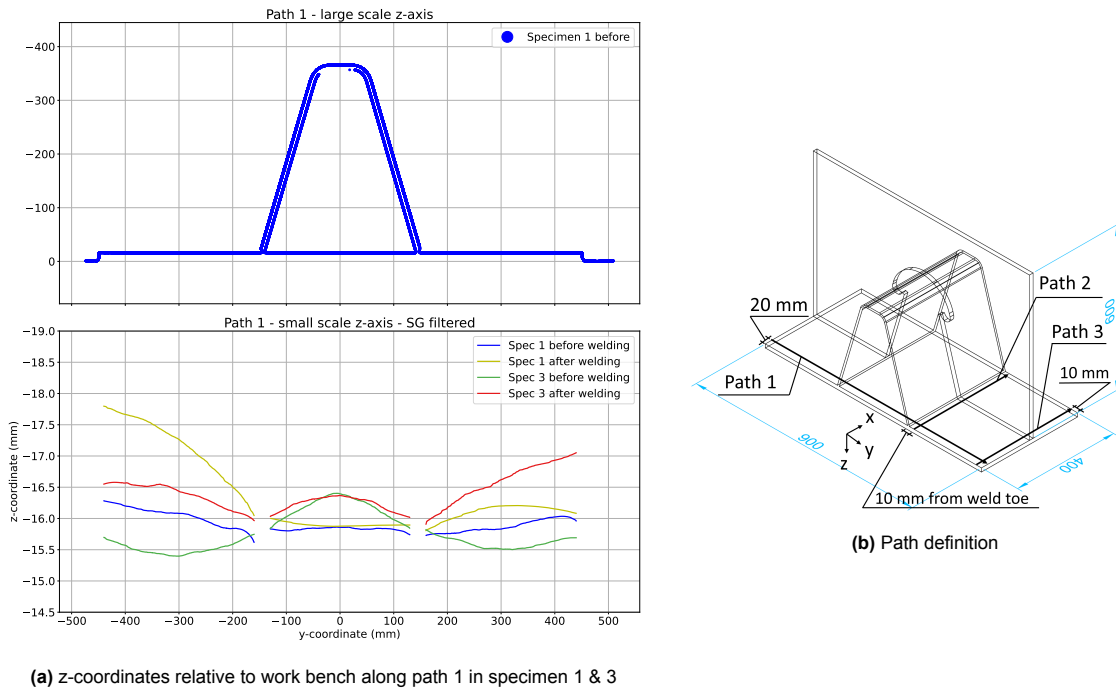
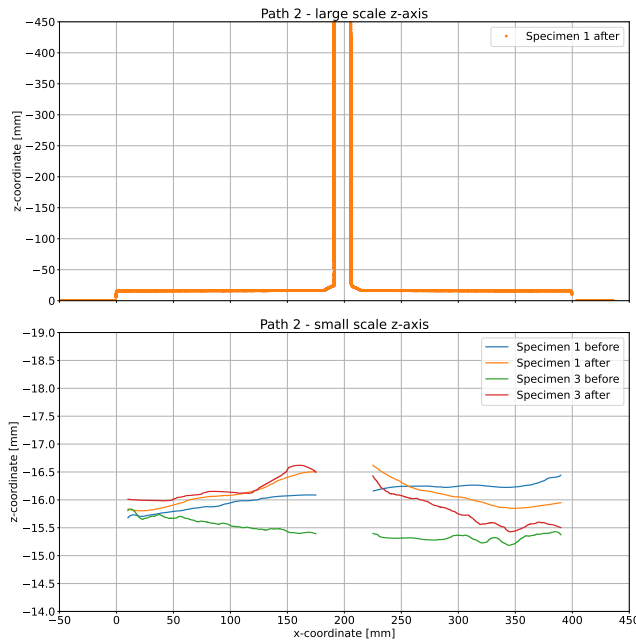
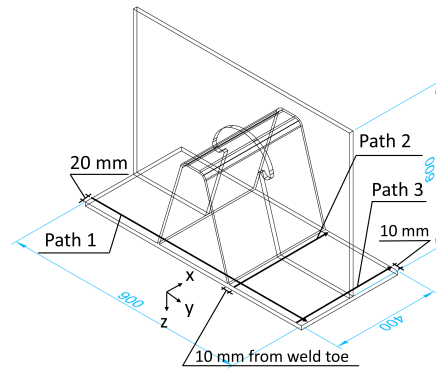


Figure 3.12: z-coordinates of top of deck plate before and after welding along path 1 in specimen 1 & 3

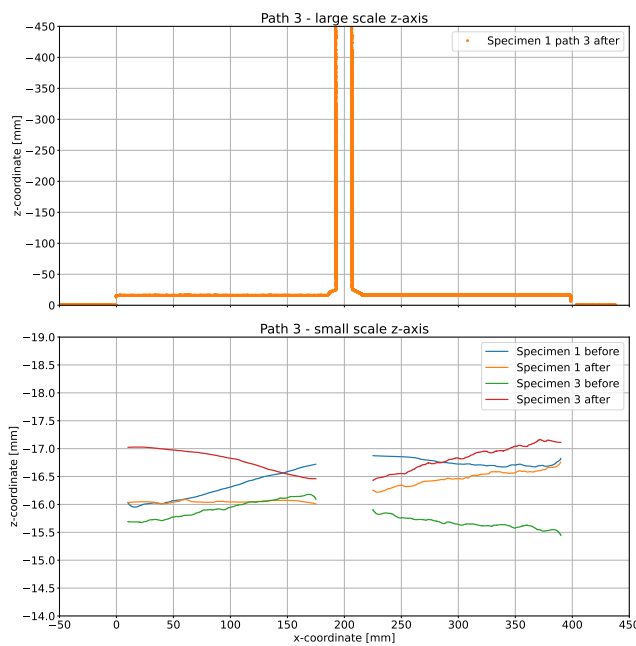


(a) z-coordinates relative to work bench along path 2 in specimen 1 & 3

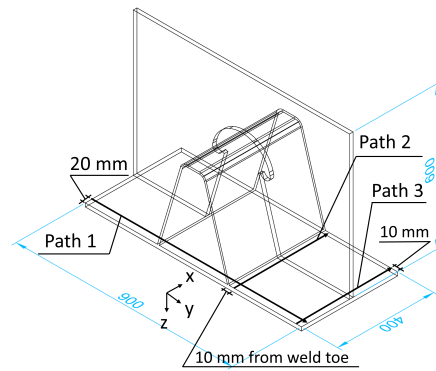


(b) Path definition

Figure 3.13: z-coordinates of top of deck plate before and after welding along path 2 in specimen 1 & 3



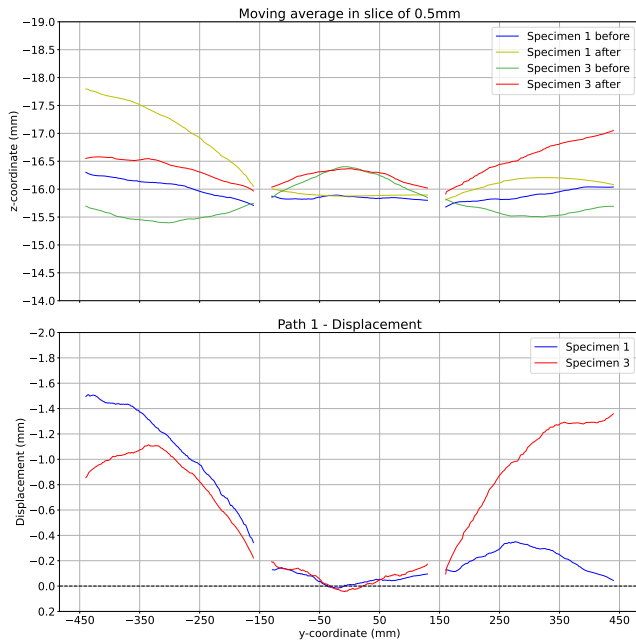
(a) z-coordinates relative to work bench along path 3 in specimen 1 & 3



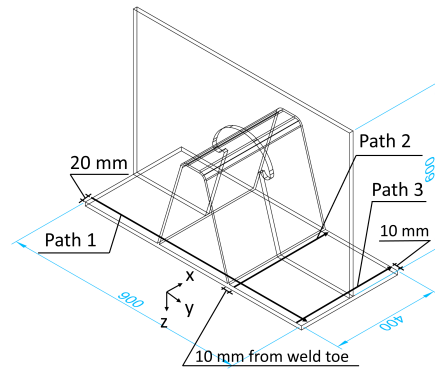
(b) Path definition

Figure 3.14: z-coordinates of top of deck plate before and after welding along path 3 in specimen 1 & 3

Distortions were obtained by subtracting the array containing the z-coordinates of the deck plate before welding from the array after welding. In order to subtract the arrays, the arrays must have equal length and the z-coordinates must have the same x or y-coordinate, depending on the path. Therefore, the paths were divided in slices of 0.5mm and the mean of the z-coordinate and x or y-coordinate were calculated in each slice. The resulting geometry and deformation of Path 1, 2 and 3 are shown in Figure 3.15, 3.16 and 3.17, respectively.

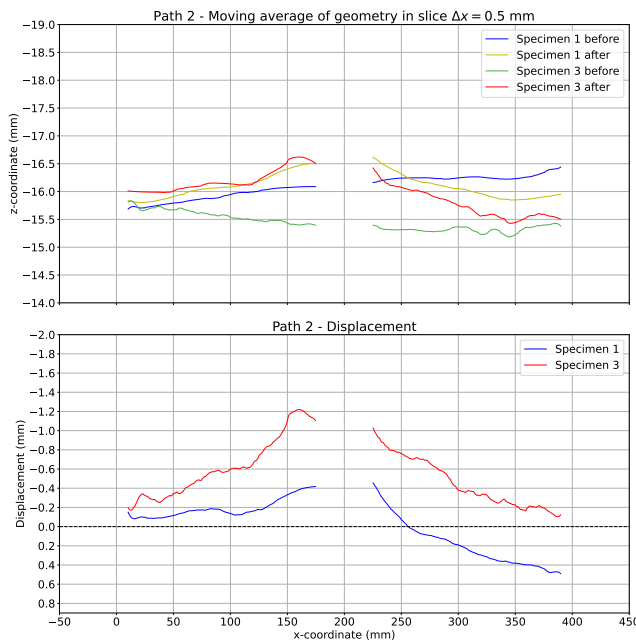


(a) Geometry top of deck plate and displacements along path 1

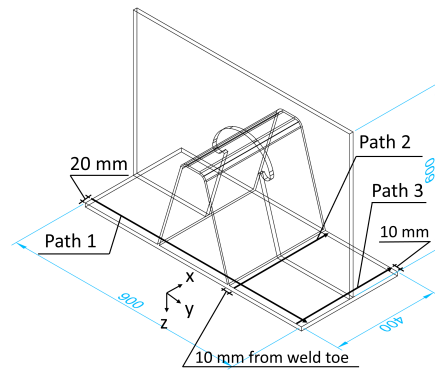


(b) Path definition

Figure 3.15: Geometry relative to workbench and displacements along path 1 in specimen 1 & 3



(a) Geometry top of deck plate and displacements along path 2



(b) Path definition

Figure 3.16: Geometry relative to workbench and displacements along path 2 in specimen 1 & 3

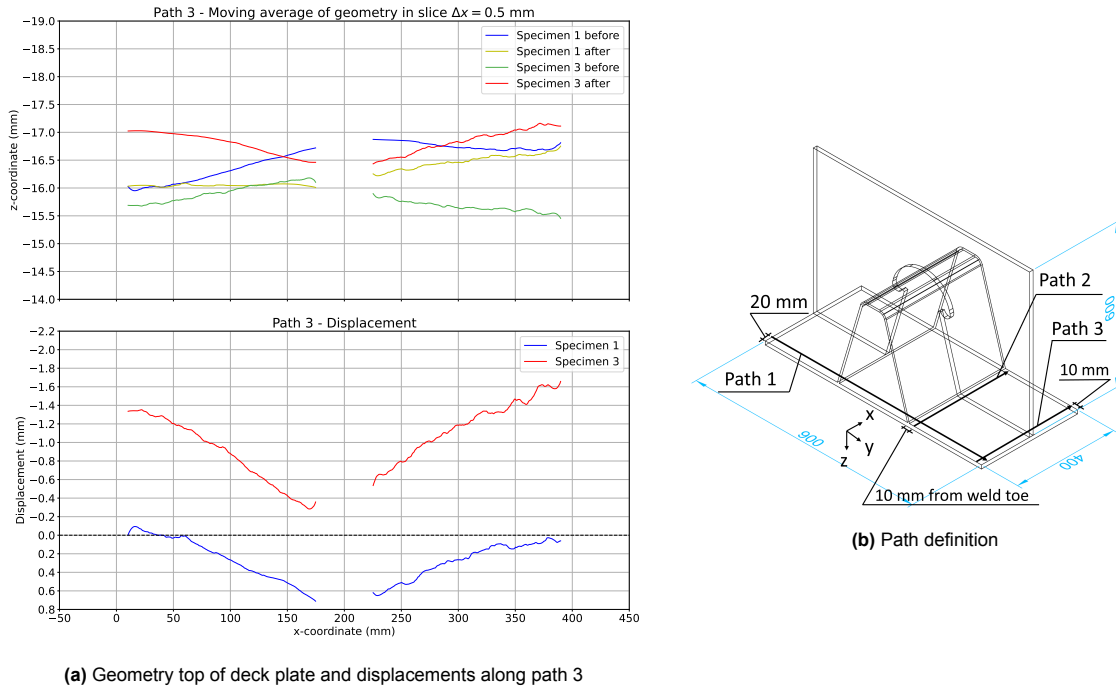


Figure 3.17: Geometry relative to workbench and displacements along path 3 in specimen 1 & 3

The maximum upward displacement occurs in Path 3 in Specimen 3 and is equal to 1.6 mm. While the deformation shapes of path 2 and 3 are similar, a vertical shift between the results of specimen 1 and 3 is found. The displacements of Specimen 1 also appears to be rotated clockwise in Path 2. This can be caused by a difference in the location and orientation of the reference coordinate system in the before and after scan. The order of magnitude and deformation shape is comparable to deformations of the rib-to-deck specimens used in the research of Sim et al. [9], where four trapezoidal stiffeners without crossbeams were investigated as shown in Figure 3.18. The measured vertical displacement of five points in transverse direction are shown in Figure 3.19. In the research, Specimen 1 was non-pre-cambered and is, therefore, the most comparable to results in this thesis. The displacement of Specimen 1 between 0.1 and 0.4m is approximately 3mm. Adding a crossbeam will reduce this displacement and the slope will be shallower. The values cannot directly be compared, due to differences in geometry, welding procedure and material properties, but the order of magnitude is comparable. The measured displacements will be compared to numerical results in Chapter 4.

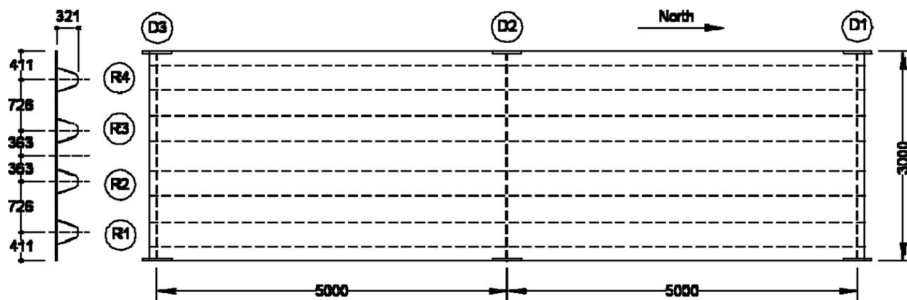


Figure 3.18: Dimensions of the specimen in research of Sim et al. [9]

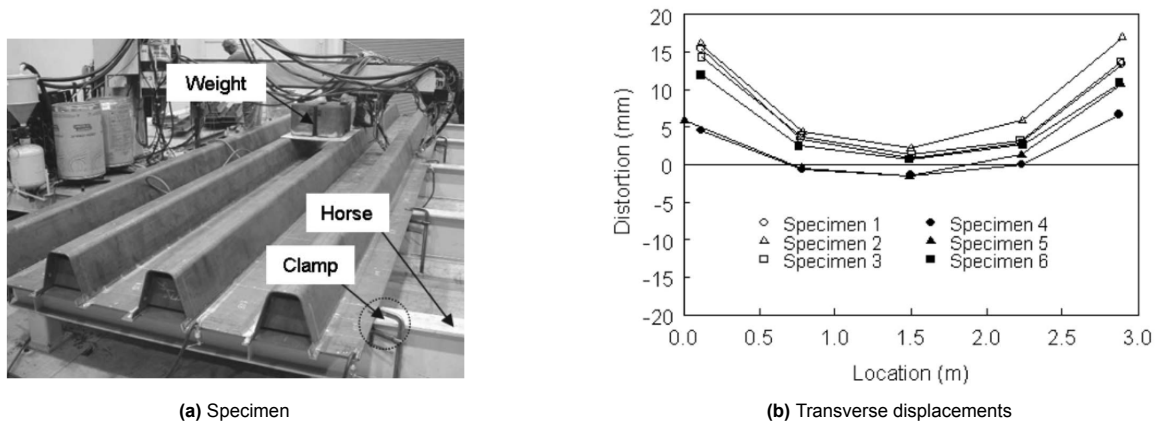


Figure 3.19: Specimen and welding induced transverse displacements by Sim et al. [9]

3.6. Conclusions

Experimental investigations of deformations and temperature distribution due to welding were performed on the full-scale segment of an OSD. These data are required to optimize the welding procedure, limit distortions and improve the understanding of the residual stress state in welded details derived from the deformation field. A new distortion measurement methodology has been established using an advanced handheld 3D scanner. The conclusions from the experiment are listed below.

1. A maximum temperature of 1042 ° C 1.8s after welding was recorded.
2. The temperature 150mm behind the heat source 1.8s after welding reduces to 200 ° C. In front and perpendicular to the heat source, the temperature decreases to room temperature at 50 and 150mm, respectively.
3. The maximum measured upward displacement of the 900x400 deck plate was 1.6mm.
4. The order of magnitude of the deformation is comparable to research by Sim et al. [9]. However, no crossbeam was used in that research. In addition, a different welding procedure and material properties were used, so no strict comparison is justified. Adding a crossbeam would decrease deformation values and reduce the slope, which is in line with the obtained results.
5. The maximum scatter in vertical coordinates along a path was approximately 0.25mm.
6. The established methodology for measuring distortions with the 3D scanner is accurate and easy to perform, but scanning must be done carefully to prevent misalignment of frames and at least 64GB of computer memory is required to post-process results. The origin and orientation of the reference coordinate system in the scan must be defined very carefully to minimize shift and rotation of the deformation graph.

3.7. Discussion

The obtained deformation shape and order of magnitude is comparable to research by Sim et al.[9]. However, no crossbeam was used in that research. In addition, a different welding procedure and material properties were used, so no strict comparison is justified. Adding a crossbeam will decrease deformation values and the slope will be shallower, which is in line with obtained results. The following factors have an influence on the overall accuracy.

1. The accuracy of the Artec Leo scanner. According to the manufacturer, it can reach a 3D point accuracy of up to 0.1mm [46]. Chosen settings such as HD density will affect the accuracy. The exact accuracy with the current settings is unknown and needs to be studied in more detail.
2. Frame misalignment and surface reflections occurring during scanning.
3. Inaccuracies in placement and orientation of the reference coordinate system in the Artec software. These will occur when the workbench surface is not completely flat. The location and

orientation of the coordinate system in the before and after scan must be exactly the same, but deviations can occur due to visual errors.

4. Post-processing steps and parameters. In the raw data, a scatter of approximately 0.25 mm in z-coordinates along each path was found. The data has been filtered with the SG algorithm, which parameters affect the accuracy.

3.8. Recommendations

In future work, the use of more accurate scanners, such as the Artec Spider, or alternative equipment such as laser- or 3D photography equipment is recommended to investigate the accuracy. Furthermore, the data can be used to improve welding simulation and fatigue life prediction models. Finally, the accuracy of the chosen boundary conditions in simulating a full-scale bridge deck can be investigated by measuring distortions in a full-scale bridge deck. These findings could help reduce the size of numerical models.

4

Numerical simulation of the welding experiment

4.1. Introduction

In this chapter, the numerical simulation of the welding experiment is explained. The simulation consists of a subsequently coupled thermal and mechanical analysis in the commercially available Abaqus® FE-software. In the thermal analysis, the Goldak [20] double ellipsoid heat source model (DEHSM) is used to simulate the heat input from the welding torch. In the mechanical analysis, the obtained thermal results are predefined. The main objective is to determine the accuracy of the numerical model. The experiment has been simulated as accurately as possible by incorporating the weld geometry, power input, welding speed and cooling times of each pass of specimen 1 in the model. The model is validated by the thermal and displacement measurements obtained in Chapter 3 and residual stresses are presented.

4.2. Units

Abaqus does not consider units, so the units of the geometry, material properties and loading need to be consistent. Results for stresses and displacements are preferred to be in MPa and mm, since the experimental data is also in mm. To obtain this, the SI [mm] format is used as shown in Table 4.1. The multiplier to convert regular SI units to SI [mm] units is also shown in the table.

Table 4.1: SI (mm) units format

Quantity	SI	SI (<i>mm</i>)	Multiplier
Length	<i>m</i>	<i>mm</i>	10 ³
Force	<i>N</i>	<i>N</i>	1
Mass	<i>kg</i>	<i>tonne</i>	10 ⁻³
Time	<i>s</i>	<i>s</i>	1
Stress	<i>N/m²</i>	<i>N/mm²</i>	10 ⁶
Energy	<i>J</i>	<i>mJ</i>	10 ³
Density	<i>kg/m³</i>	<i>tonne/mm³</i>	10 ⁻¹²
Conductivity	<i>W/m.K</i>	<i>mW/mm.K</i>	1
Specific heat	<i>J/kg.K</i>	<i>mJ/tonne.K</i>	10 ⁶
Convection	<i>W/m².K</i>	<i>mW/mm².K</i>	10 ⁻³
Stefan-Boltzmann constant	<i>W.m⁻².K⁻⁴</i>	<i>mW.mm⁻².K⁻⁴</i>	10 ⁻³

4.3. Model

The full-scale specimen is modelled in Abaqus/2019© FEA software. The dimensions are given in figure 4.1a and all welding passes from the experiment are simulated. The passes are defined in figure 4.1b

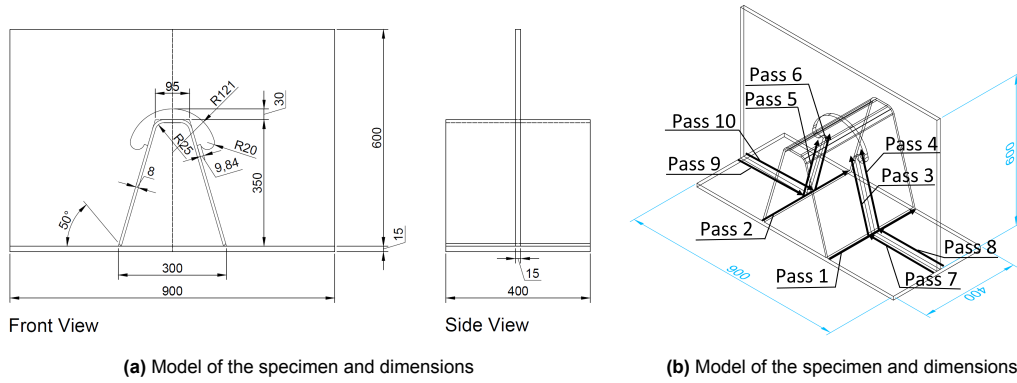


Figure 4.1: Dimensions specimen and welding passes

The model consists of three parts: Part 1 - local; Part 2 - global; and, Part 3. The three parts are shown in Figure 4.2a, 4.2b and 4.2d, respectively. The parts are connected by tie constraints. The assembled model is shown in Figure 4.2e.

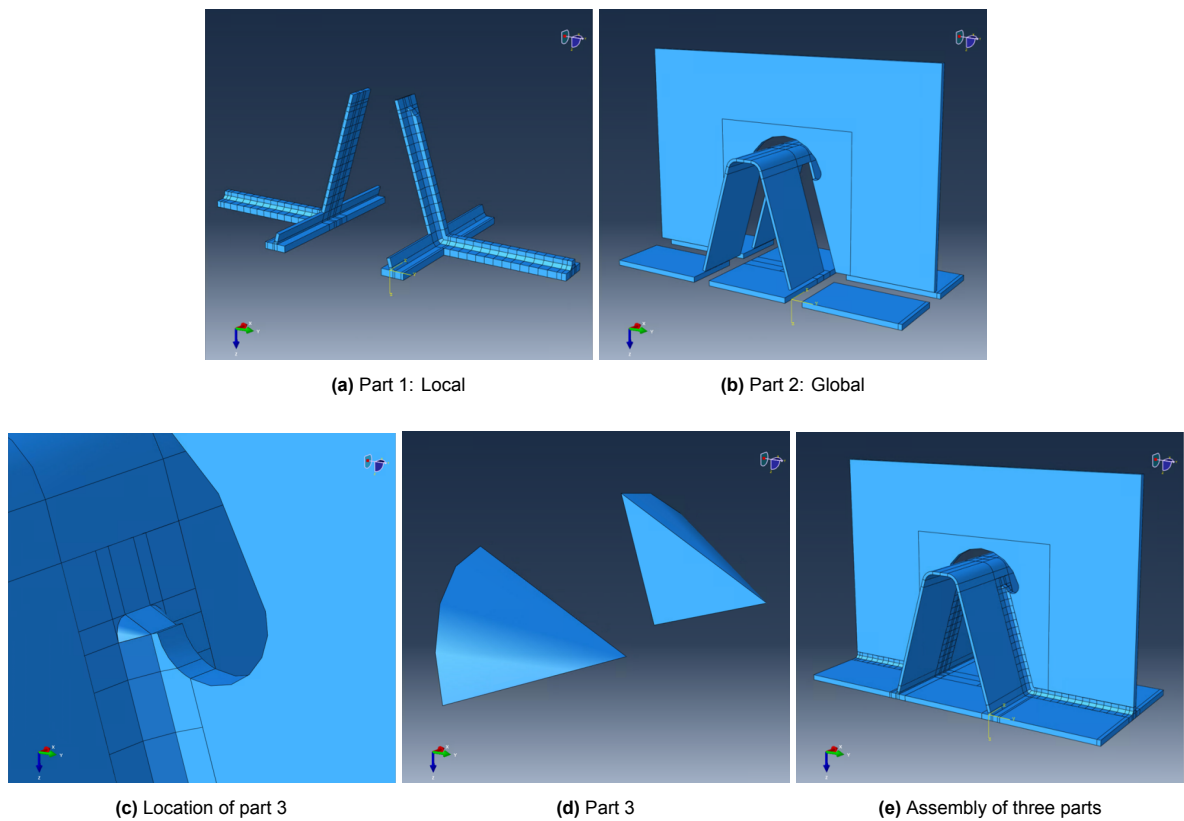


Figure 4.2: Crossbeam model consisting of three parts

A fine mesh is used in the local part to obtain accurate results regarding step temperature, stress and displacement gradients close to the weld. A coarser mesh is used in the global part to save computation time. The local and global part result from merging sub-parts, which were created by the extrusion or

sweep feature in Abaqus. Part 3 was not merged with part 2 due to its complex geometry. Tetrahedral elements were used in part 3 due to its complex geometry and hexagonal elements were used in part 2. The parts were not merged, but connected by tie constraints to ensure a good mesh transition. In the local part, partitions were made to divide the vertical passes in 15 equal steps of 19.37 mm and the horizontal passes 7-10 in 15 equal steps of 20.144 mm.

The geometry of part 1 is shown in Figure 4.3.

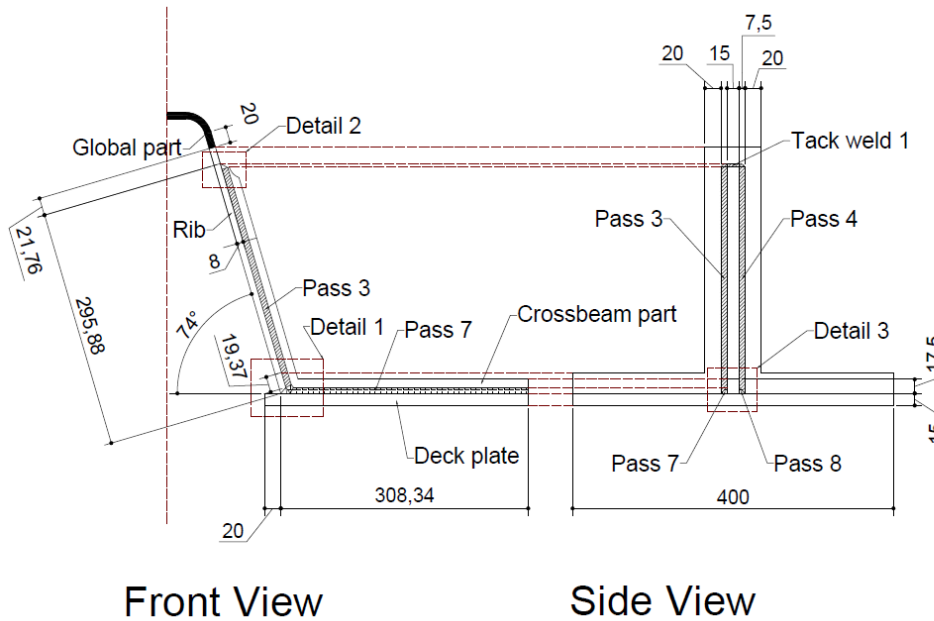


Figure 4.3: Geometry part 1

The weld geometry is obtained from scans of specimen 1. The weld shape is modelled as accurately as possible, but some simplifications need to be made. The weld shape and size are idealized. In Figure 4.4, a comparison between measured and modelled weld dimensions at the rib-to-crossbeam connection is shown.

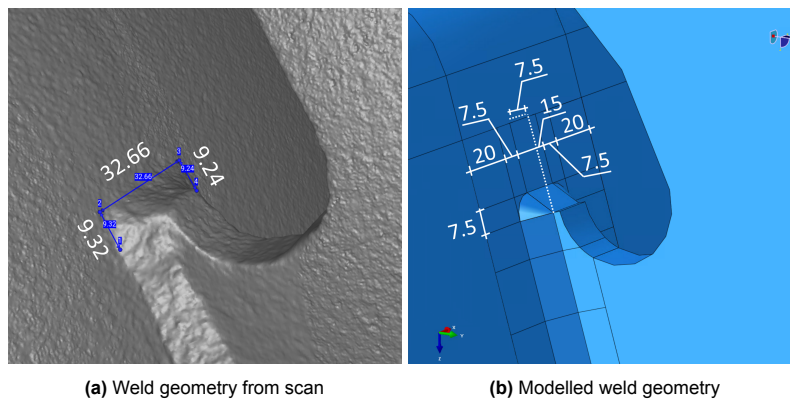


Figure 4.4: Modelled weld geometry and comparison to scanner data of rib-crossbeam connection

In Figure 4.5, a comparison between the measured and modelled weld geometry of the tack weld at the rib-to-crossbeam connection, pass 1.2 and the crossbeam-deck connection are shown.

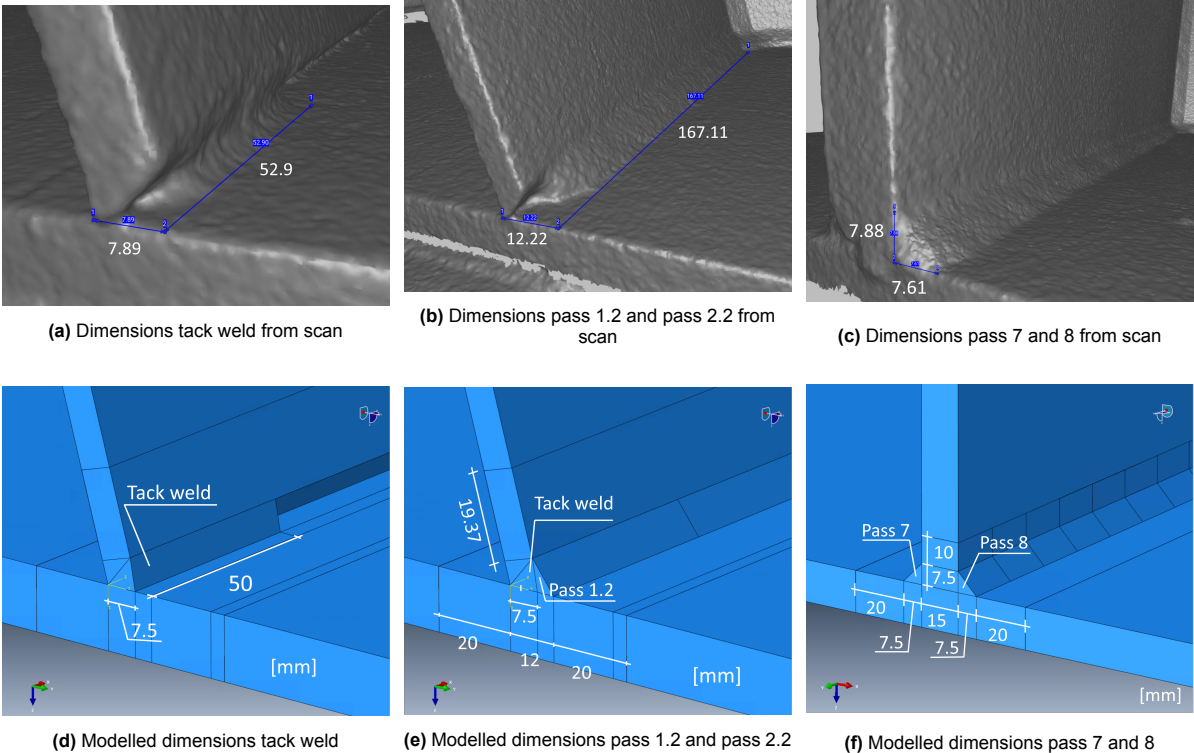


Figure 4.5: Modelled weld geometry and comparison to scanner data

4.4. Model details

4.4.1. Mesh

The mesh size of the thermal and the mechanical models are equal. The mesh size is 2.5 mm in part 1 - local and 20 mm in part 2 - global. The mesh of the entire model is shown in Figure 4.6.

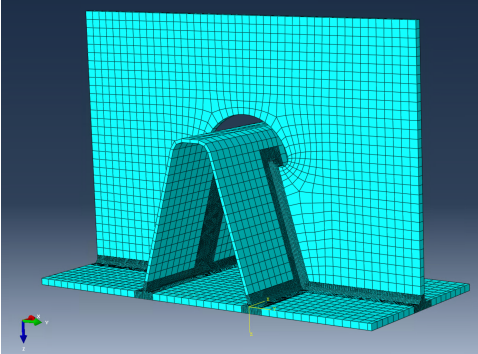


Figure 4.6: Mesh of full model

Detailed images of the mesh at the rib-to-deck, rib-to-crossbeam and crossbeam-to-deck connection are shown in Figure 4.7.

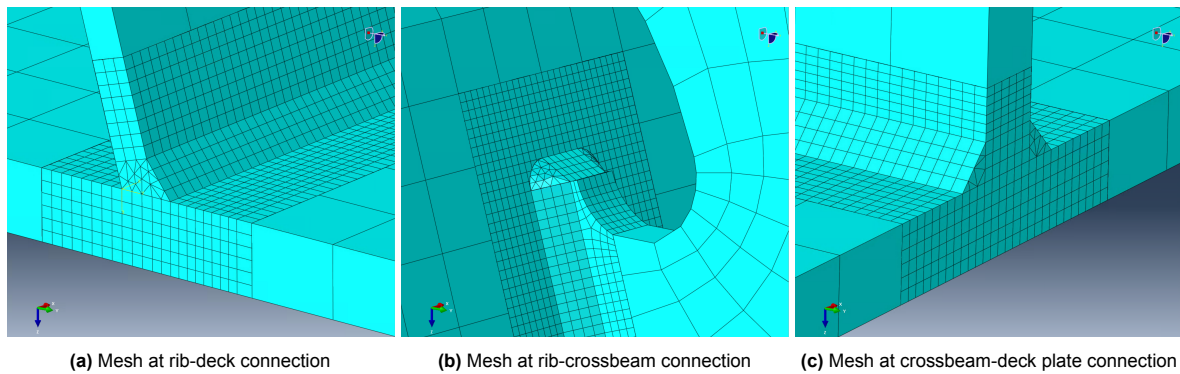


Figure 4.7: Close-up view of mesh

In the thermal model, wedge shaped DC3D6 heat transfer elements are used for the weld elements to prevent element distortion. Tetrahedral DC3D4 elements are used in part 3 due to its complex geometry. The other elements are hexahedral DC3D8 elements. The total number of nodes is 174821. The total number of elements is 149633, consisting of 403 linear tetrahedral elements of type DC3D4, 131784 linear hexahedral elements of type DC3D8 and 17446 linear wedge elements of type DC3D6. In the mechanical analysis, the corresponding 3D stress elements C3D6, C3D4 and C3D8 are used.

4.4.2. Steps

The simulation steps and their duration are given in Table 4.2.

Table 4.2: Simulation steps and step time

Step	Name	Time (s)	Step	Name	Time (s)
1	Pre-step	1e-5	107-121	Pass 4	73
2-21	Pass 1.1	45	122	Cooling 4	727
22	Cooling 1.1	134	123-137	Pass 5	81
23-42	Pass 1.2	70	138	Cooling 5	157
43	Cooling 1.2	360	139-153	Pass 6	80
44-63	Pass 2.1	46	154	Cooling 6	1320
64	Cooling 2.1	159	155-169	Pass 7	62
65-84	Pass 2.2	75	170	Cooling 7	82
85	Cooling 2.2	4000	171-185	Pass 8	58
86	Pre-step-CB	1e-5	186	Cooling 8	236
87	Heating TW 1	3	187-201	Pass 9	58
88	Cooling TW 1	20	202	Cooling 9	76
89	Heating TW 2	3	203-217	Pass 10	59
90	Cooling TW 2	20	218	Cooling 10	4000
91-105	Pass 3	89	219	Unclamping	1
106	Cooling 3	176			

In step 1, Pre-step, the welds and crossbeam elements are deactivated with the model change command from the interaction module. The model after Pre-step is shown in Figure 4.16a. After that, Pass 1.1 up to and including Pass 2.2 are reactivated in 20 steps, followed by a cooling step after each pass. This results in a weld increment size of 15 mm for Pass 1.1 and 2.1 and 20 mm for Pass 1.2 and 2.2, as shown in Figure 4.16b. To study the effect of the weld increment size on the residual stresses, the weld increments are reduced to 10mm per step in the next section, in which the part of the experiment up to and including the step Cooling 2.2 is simulated.

In step 86, Pre-step-CB, the crossbeam elements and tack welds are reactivated. The location of the tack welds and their length are shown in Figure 4.8.

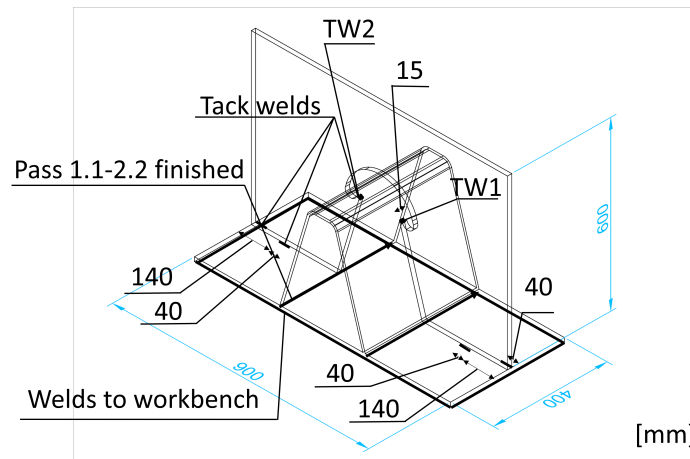


Figure 4.8: Location and length of tack welds reactivated in step 86

To simulate the application of the tack weld at the rib-to-crossbeam connection, a static heating step is introduced in step 87, Heating TW1, as shown in Figure 4.16e.

After the addition of the crossbeam, passes 3-10 are reactivated in 15 steps followed by a cooling step after each pass. Passes 3-6 are reactivated in 15 steps of 19.37 mm. Passes 7-10 are reactivated in 15 steps of 20.144 mm. Finally, an unclamping step is created in the mechanical model in which the workbench welds are removed and the unclamping boundary conditions shown in Figure 4.9 are introduced.

A Python script was used to create the welding steps and to deactivate and reactivate weld elements. The script for the thermal model can be found in appendix C and the script for the mechanical model in appendix D.

4.4.3. Boundary conditions

Thermal

In the thermal model, convection and surface radiation were defined. The convection coefficient was defined as $15W/m^2$ [44] and the emissivity as 0.5, which is the average of the temperature dependent values presented by Frewin & Scott [52].

Mechanical

The mechanical boundary conditions are shown in Figure 4.9.

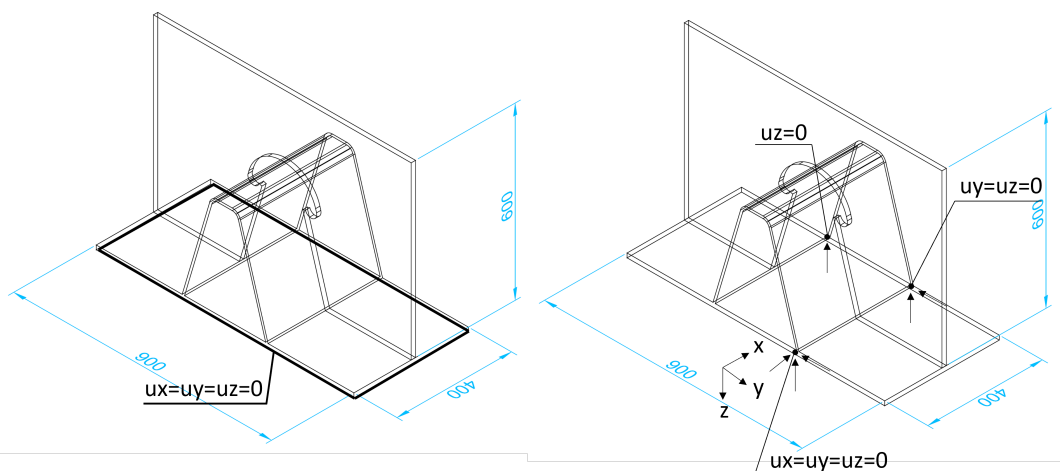


Figure 4.9: Boundary conditions during welding and unclamping

During welding, displacements of the sides of the deck plate are restrained by the workbench welds. Therefore, displacements u_x , u_y and u_z of the bottom sides of the deck plate are defined as zero.

In the unclamping step, some boundary conditions need to be defined to get a converging solution and to prevent global translations and rotations. A minimum of three points is required to prevent global translations and rotations. The points defined in the figure are expected to have no displacement in z-direction, since shrinkage close to the weld results in upward displacements further away from the weld, relative to the defined points. The defined points can't displace downwards into the workbench. Therefore, the vertical displacements are zero. During unclamping, the specimen must displace freely and no additional internal stresses must be generated. Therefore, the reaction forces were checked after running the analysis. All reaction forces were in the order of $1 \cdot 10^{-10}$ N. Therefore, the specimen can displace freely. Other boundary conditions have been investigated where all four corners were restrained in z-direction. This results in symmetry around the x-axis and will prevent the introduction of additional residual stresses [44]. However, this led to reaction forces of $600N$ in z-direction. Finally, the sequence of removing the workbench welds might have an influence on the residual stress distribution. However, the removing sequence has not been documented during the experiment, so a single unclamping step is introduced. The developed model is proven to be working and boundary conditions can be easily adjusted. Therefore, in future studies, the influence of unclamping boundary conditions and the workbench weld removal sequence on the residual stress distribution can be investigated.

4.5. Heat input

The Goldak double ellipsoid heat source model (DEHSM) is defined as a load in the thermal analysis via a Dflux subroutine. The subroutine is written in Fortran and can be found in appendix E. The DEHSM is shown in Figure 4.10.

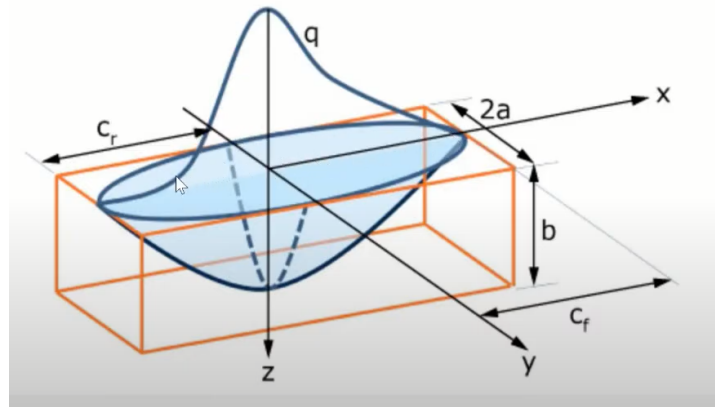


Figure 4.10: Goldak double ellipsoid heat source model [53]

The front and rear part of the heat source are described by Equation 4.1 and 4.2, respectively. The heat source parameters a , b , c_f , and c_r are related to the weld geometry.

$$q_f(x, y, z, t) = \frac{6\sqrt{3}f_f Q}{abc_f \pi \sqrt{\pi}} \exp\left(-3\left(\frac{x^2}{c_f^2} + \frac{y^2}{a^2} + \frac{z^2}{b^2}\right)\right) \quad (4.1)$$

$$q_r(x, y, z, t) = \frac{6\sqrt{3}f_r Q}{abc_r \pi \sqrt{\pi}} \exp\left(-3\left(\frac{x^2}{c_r^2} + \frac{y^2}{a^2} + \frac{z^2}{b^2}\right)\right) \quad (4.2)$$

Where:

- f_f is the fraction of the power at the front of the heat source, generally taken as 0.6
- f_r is the rear fraction, generally taken as 1.4

- Q is the power input from the welding torch calculated by $\eta * U * I$, where η is the efficiency, U is the voltage and I is the current.
- $2a$ is the width of the heat source, taken as the length of the hypotenuse of the weld
- b is the depth of the heat source, taken as the depth of the weld
- cr is the length of the front part ($x > 0$) of the heat source, generally taken as $2.33a$
- cf is the length of the rear part ($x < 0$) of the heat source, generally taken as a

The parameters for Pass 1.1 and 1.2, tack weld 1 and Pass 7 and 8 are shown in the detail drawings in Figure 4.11. The heat source was rotated by the angles specified in the figure.

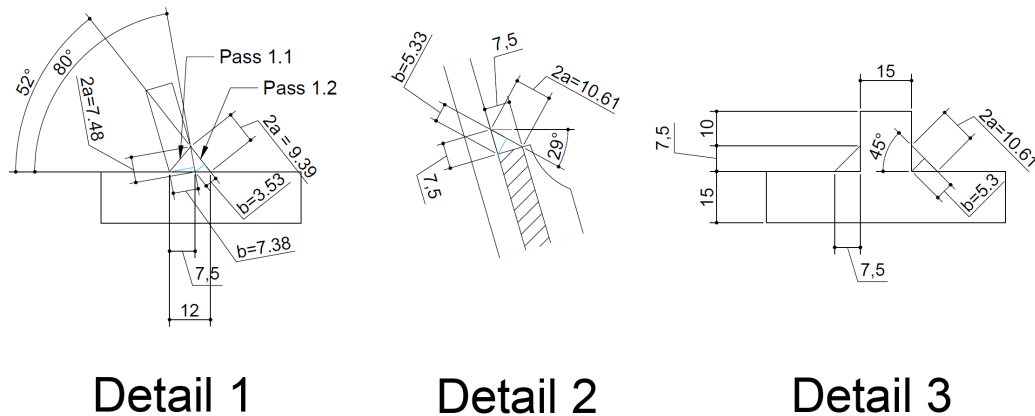


Figure 4.11: Detail drawings from Figure 4.3 with Goldak DEHSM parameters for pass 1.1 & 1.2, tack weld 1 and pass 7 & 8, respectively

4.6. Material properties

Temperature dependent material properties of steel are a topic of interest in welding journals and fire safety engineering. In welding journal, Frewin & Scott [52] proposed temperature dependent properties of thermal conductivity, specific heat, emissivity and density up to 2860 °C. In the same journal, Brown & Song [54] proposed temperature dependent mechanical properties of yield stress, Young's modulus and the thermal expansion coefficient up to 5000 °C. Temperature dependent stress-strain curves have been measured in research of Boko, Toric and Peros [55] for determining the resistance of steel structures exposed to fire. Finally, thermal and mechanical temperature dependent material properties for fire design are given in Eurocode 3 part 2 [56]. However, the values provided in EN1993-1-2 [56] are an approximation for fire engineering purposes and the values do not reach temperatures higher than 1600 °C. Therefore, the values have not been considered.

The material properties used in the model are shown in Figure 4.12. Constant values for conductivity and specific heat are defined, because the thermal analysis with temperature dependent thermal properties takes a significant amount of computation time with the current model size. It is assumed that this simplification will not affect the deformations and residual stresses significantly. This hypothesis will be justified by comparing results with another model which simulates the experiment up to and including the step Cooling 2.2 with temperature dependent thermal properties. In the refined model, the values proposed by Brown & Song [54] are used. These values are also shown in Figure 4.12.

The stress-strain curve definition in Abaqus is shown in Figure 4.13. In the figure, the curve provided in EN1993-1-2 and the curve obtained from experiments by Boko, Toric and Peros [55] are shown for comparison. The Eurocode values show a large deviation from experiments at higher temperatures. Therefore, these values have not been used in Abaqus. The experimental data from Boko, Toric and Peros [55] show more realistic behaviour. However, at higher strains, stress values at higher temperatures become lower than stress values at lower temperatures. For example, at a strain of 0.14, the stress at 400 °C is 200 MPa, while the stress at 500 °C is 290 MPa. This behaviour is unrealistic and therefore, the values have been modified.

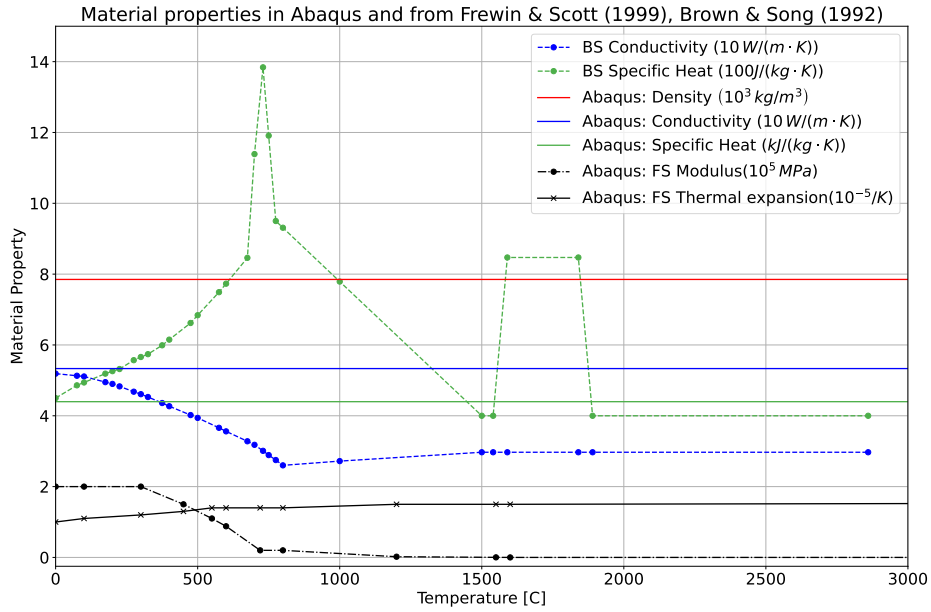


Figure 4.12: Material property definition in Abaqus and comparison to Brown & Song [54] (BS) and Frewin & Scott [52] (FS)

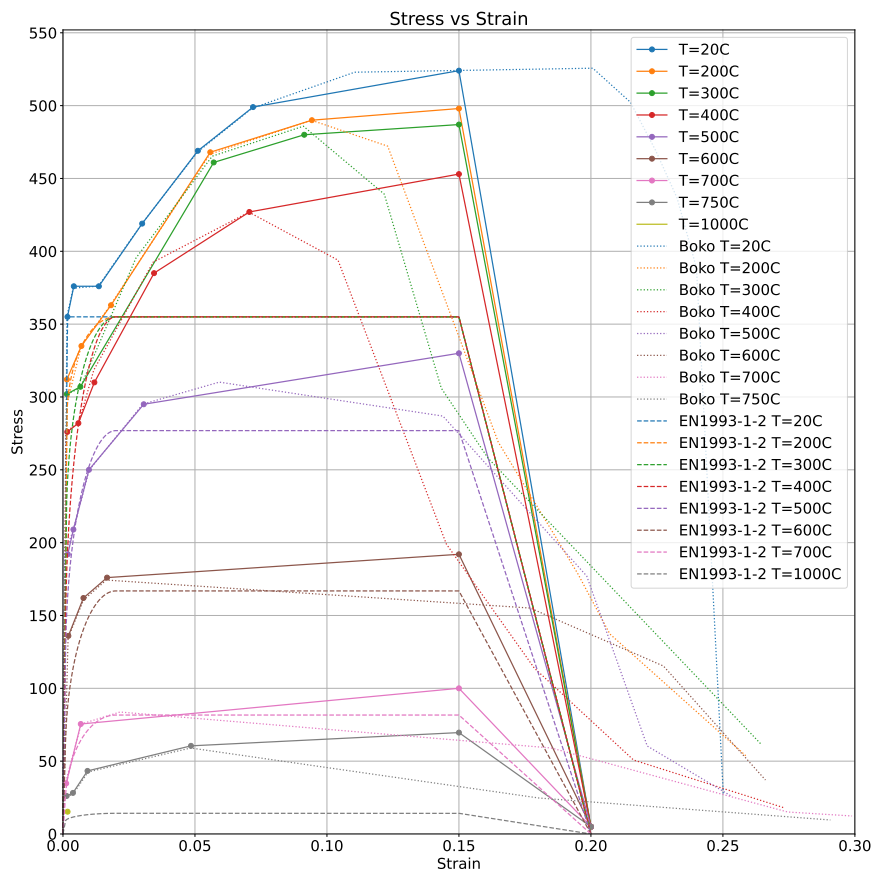


Figure 4.13: Stress-strain curve definition of S355 in Abaqus and comparison to Boko, Toric and Peros [55] and EN1993-1-2 [56]

Finally, an anneal temperature of 1000 °C has been specified in the plastic material property definition.

When the anneal temperature is reached, the plastic strain will be set to zero.

4.7. Parametric study

As mentioned in the previous section, the effect of temperature dependent thermal properties on the temperature, deformations and residual stresses is investigated by comparing the crossbeam model with a more refined model. The refined model simulates the experiment up to and including the step Cooling 2.2 with temperature dependent thermal properties. Values for specific heat and conductivity proposed by Brown & Song [54] are defined in the model. The other material properties remain unchanged. In addition, the influence of the weld increment size is investigated. In the refined model, the weld increment size is reduced from 15 and 20 mm for pass 1.1 and 1.2, respectively, to 10 mm per step. Finally, the mesh size of the global part is reduced from 20 mm to 10 mm. The local and global part are shown in Figure 4.14.

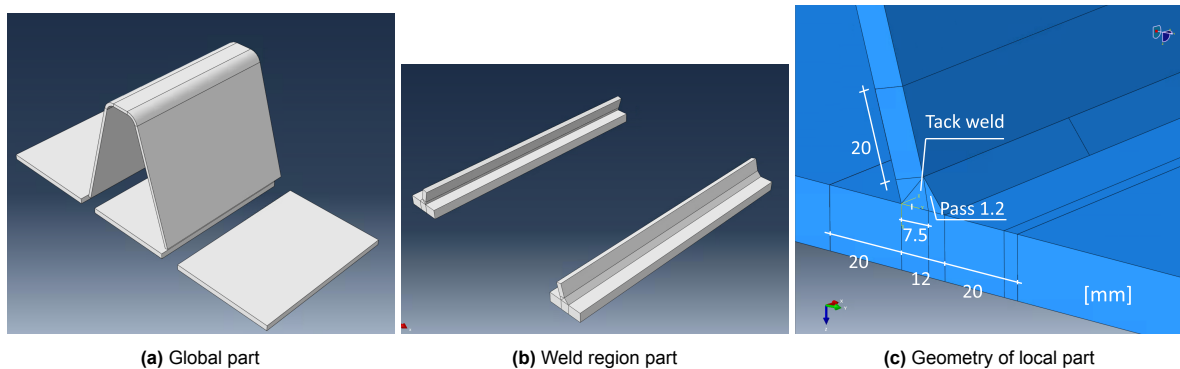


Figure 4.14: Global part and local weld part

The mesh is shown in Figure 4.15. The global mesh size is reduced from 20 to 10mm, compared to the crossbeam model by changing the local seed size of the entire model in Abaqus. The element size in the local model and the element types remain unchanged.

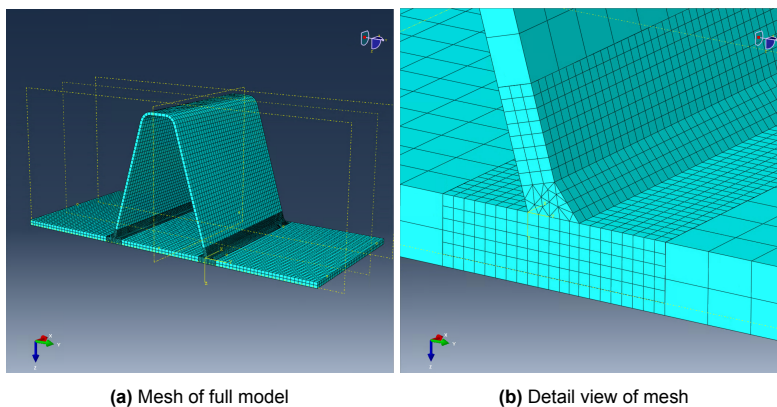


Figure 4.15: Mesh of the rib-to-deck model

The steps are given in Table 4.3.

Table 4.3: Simulation steps and step time

Step	Name	Time (s)	Step	Name	Time (s)
1	Pre-step	1e-5	74-103	Pass 2.1	46
2-31	Pass 1.1	45	104	Cooling 2.1	159
32	Cooling 1.1	134	105-144	Pass 2.2	75
33-72	Pass 1.2	70	145	Cooling 2.2	4000
73	Cooling 1.2	360	146		

The steps and the element activation and deactivation is done with a modified version of the python scripts given in Appendix C and D.

Temperature, displacements and residual stresses are compared with experimental data and with the simulation of the full experiment in the next section.

4.8. Results

4.8.1. Temperature

The temperature distribution around the heat source for various passes is shown in Figure 4.16.

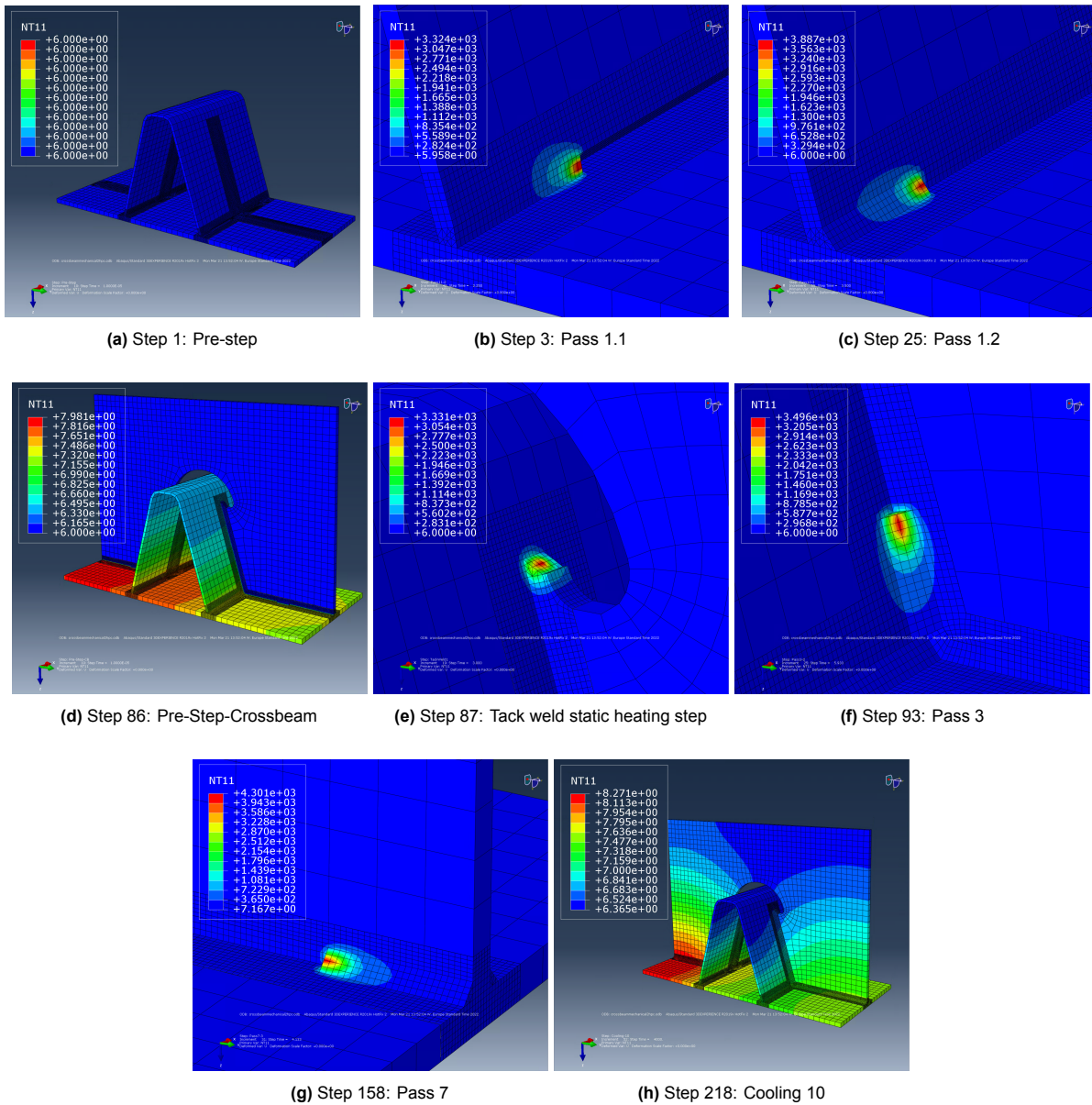


Figure 4.16: Temperature distribution at end of step 1, 3, 25, 86, 87, 93, 158 and 218

The maximum temperature in the weld pool resulting from the thermal analysis is between 3000-4000 °C and it decreases quickly to approximately 1400 °C 10mm behind the heat source and 5 mm perpendicular to the heat source.

When using temperature dependent thermal properties, higher maximum temperatures are obtained, as shown in the comparison in Figure 4.17.

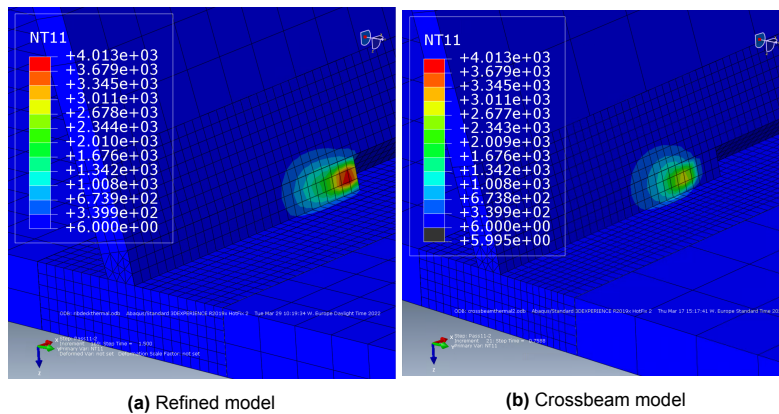
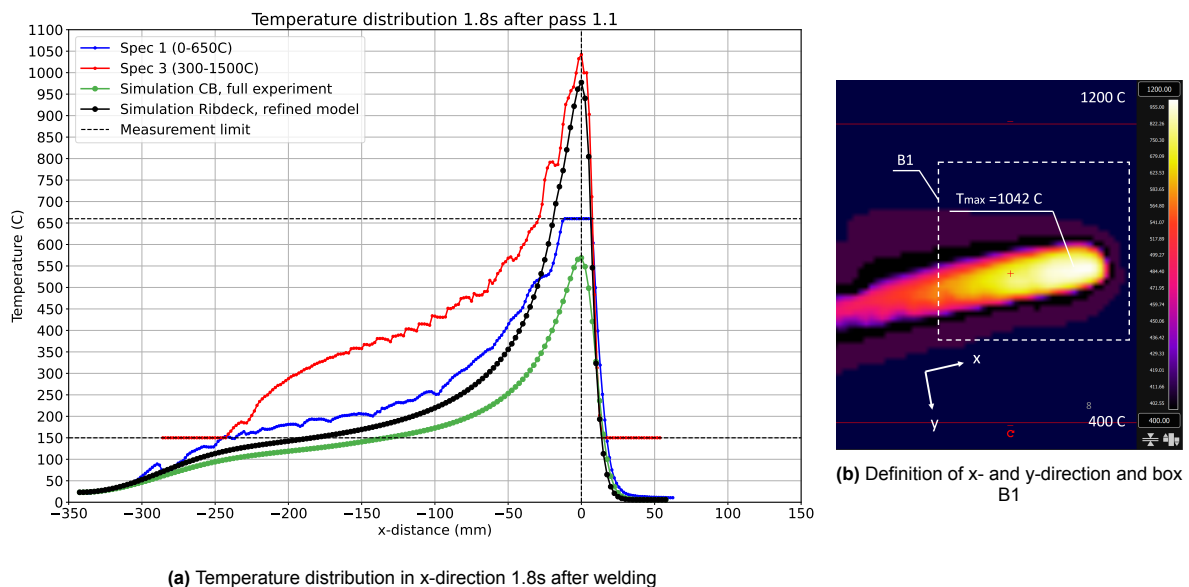


Figure 4.17: Temperature distribution around the heat source 3s since start pass 1.1

The temperature distribution around the heat source is further quantified in Figure 4.18. In the figure, the temperature 1.8s after Pass 1.1 at a distance x is presented, where the positive x -direction is the welding direction. As mentioned in Chapter 3, Specimen 3 shows deviations compared to expected values in the $-250 < x < -50$ range. The same deviations are found in other passes when the recording range was set to $300 - 1500\text{C}$. The results of Specimen 1 are closer to expected values. The temperature distribution resulting from the simulation with temperature dependent thermal properties is close to the measured values of Specimen 1 for temperature values below 650C and of Specimen 3 for temperature values above 650C . Temperatures are lower when using temperature independent thermal properties. The use of temperature dependent thermal properties has a significant influence on the temperature distribution.



(a) Temperature distribution in x-direction 1.8s after welding

Figure 4.18: Mesh of the rib-to-deck model

In Figure 4.19, the maximum temperature in box B1 as a function of time is shown. Box B1 is defined in Figure 4.18b. Predicted values with temperature dependent thermal properties show better correspondence to experimental data compared to temperature independent properties. However, deviations start to occur 4s after welding. This can be explained by a deviation of the film coefficient or emissivity. Specimen 3 again shows inaccurate values after 3s of welding. Finally, temperature independent thermal properties show a faster temperature decay compared to Specimen 1 and the simulation with temperature dependent thermal properties.

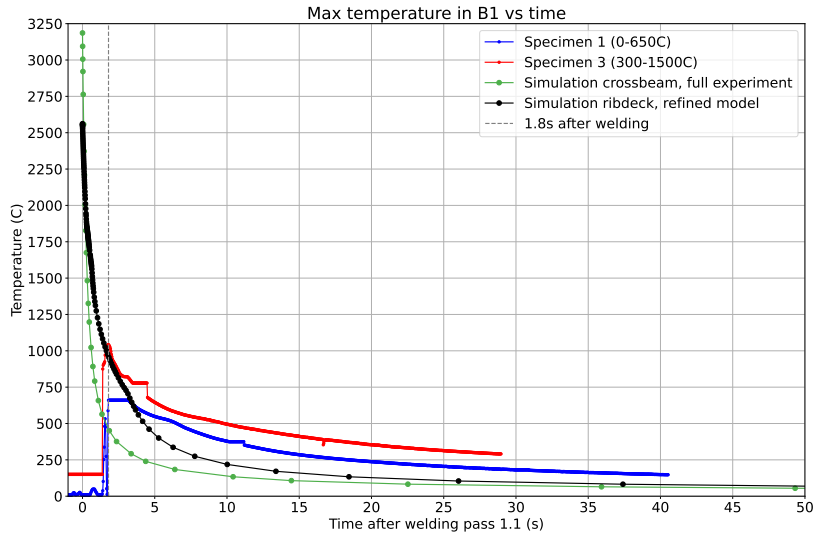
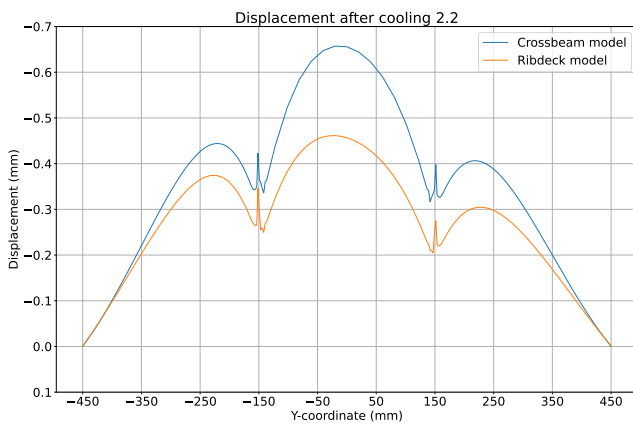


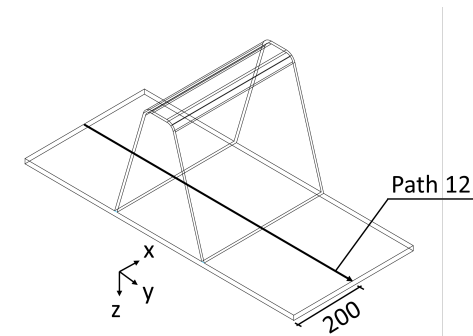
Figure 4.19: Maximum temperature after welding pass 1.1

4.8.2. Displacements

A comparison between displacements resulting from the simplified crossbeam model and the refined ribdeck model is shown in Figure 4.20. After step Cooling-2.2, the crossbeam model with temperature independent thermal properties resulted in larger values compared to the refined model with temperature dependent thermal properties. The simplifications increase the maximum deviation by 0.2mm. The relative difference is 44%, which is significant. However, the absolute difference is not significant. It is assumed that the absolute difference after the step Unclamping is also not significant. To increase the certainty, the entire model must be modelled with temperature dependent thermal properties, which increases the computation time and model size significantly. It can be investigated in future studies.



(a) Displacements after cooling 2.2



(b) Path definition

Figure 4.20: Displacements after cooling 2.2 along path 12 resulting from the refined and from the simplified model

A contour plot of the crossbeam model showing displacements in z-direction after the steps Cooling-2.2, Pre-step-crossbeam, Cooling-10 and Unclamping are shown in Figure 4.21. Displacements are magnified by a factor of 30 in the figure to improve identification of the deformation shape. The displacement magnitudes corresponding to the colors are given in the legend in mm.

Numerical values of the displacements are plotted along three paths. The paths are defined in Figure 4.22b. The displacements along Path 1 are shown in Figure 4.22a. The displacement shape and

order of magnitude corresponds well to experimental data. Deviations are found between $-150 < y < 150$, where an upward curvature is found in the numerical model and a downward curvature in the experiment. The numerical model is more in line with expectations. The deviation can be caused by initial imperfections or an error margin in the measured data. Measured displacements in Specimen 3 correspond best to the numerical results. In Specimen 1, deviations are found at $y > 150$. This can also be caused by initial imperfections. Another cause could be the removal sequence of workbench welds. In the model, it is performed in a single step, while during the experiment, workbench welds were removed one at the time.

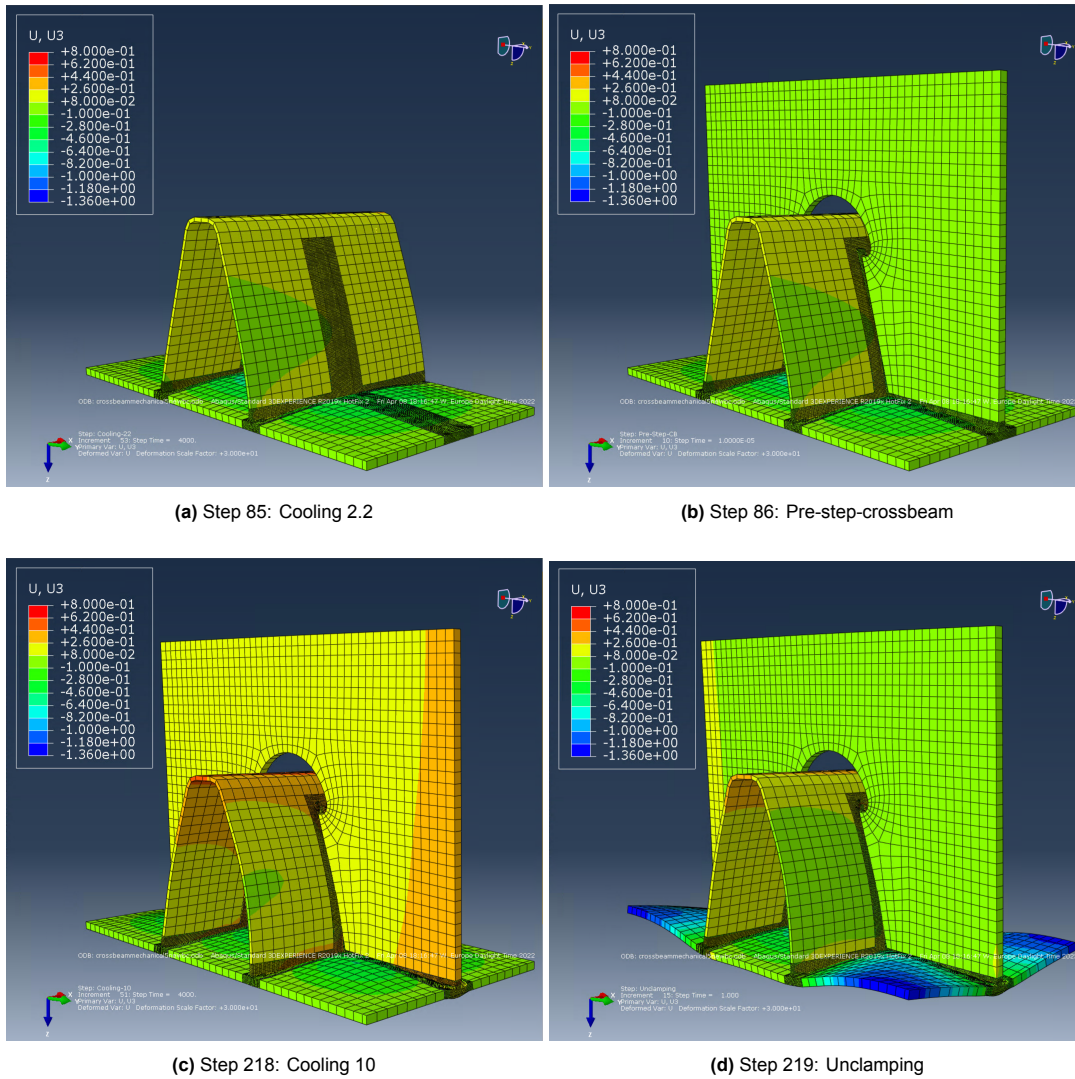
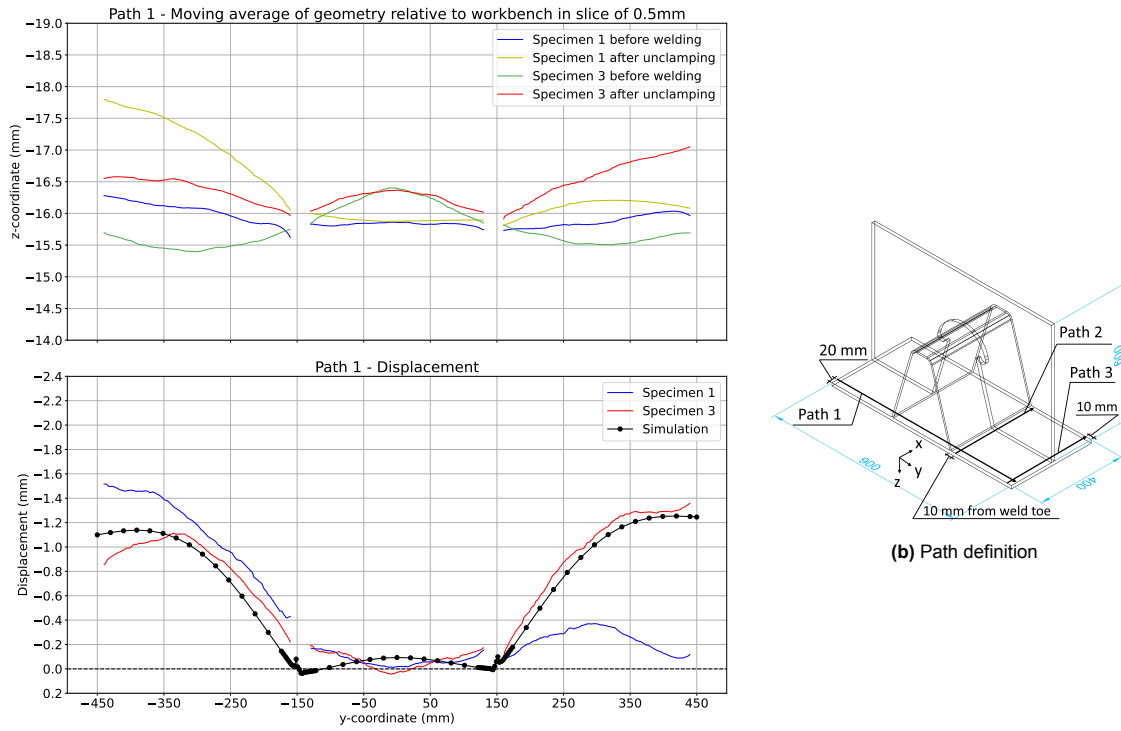


Figure 4.21: Vertical displacements after step 85, 86, 218 and 219. Displacement shape amplified by scale factor 30

Displacements along Path 2 and 3 are shown in Figure 4.23. The geometry before welding of Specimen 1 appears to be inclined, as shown in Figure 4.23a. This results in negative displacements at $x > 270mm$, as shown in Figure 4.23c, which is unrealistic. This can be caused by a difference in the location and orientation of the reference coordinate system in the before and after welding scan. The reference coordinate system is defined manually in Artec Studio and has to be aligned perfectly on the workbench. Deviations can occur due to visual errors. This is a limitation of the methodology and can only be resolved by using a perfectly flat workbench. In practice, this is not the case, so the experimental results are calibrated to the numerical results by translating and rotating the displacement graph. The calibrated results for Specimen 1 are indicated by the green line in Figure 4.23c and d. The calibrated results of Specimen 3 are indicated by the yellow line.



(a) Displacement along path 1 after unclamping

Figure 4.22: Displacement along path 1 and comparison to experimental data

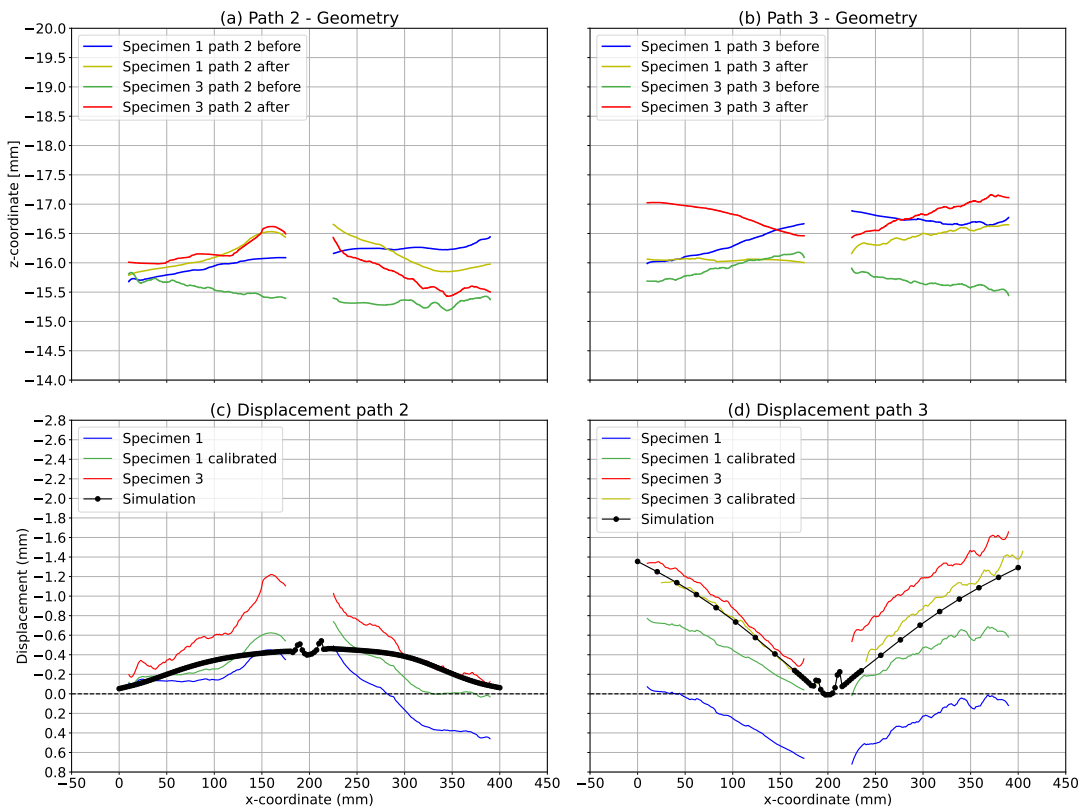


Figure 4.23: Displacement along path 2 & 3 and comparison to experimental data

Calibrated results of Specimen 3 in Path 3 correspond best to numerical results. In Path 2, the shape is similar, but magnitudes are different. This can be caused by local heat induced micro-structure changes, which are not incorporated into the model, or by differences in the modelled and actual weld geometry.

Due to good correspondence of numerical and experimental results, especially in Specimen 3, the numerical model is validated with satisfactory accuracy. Therefore, residual stresses will be presented in the next section. The influence of the temperature dependent thermal properties on the residual stress distribution will be presented as well.

4.8.3. Residual stresses

Residual stresses are shown along 8 paths as defined in Figure 4.24.

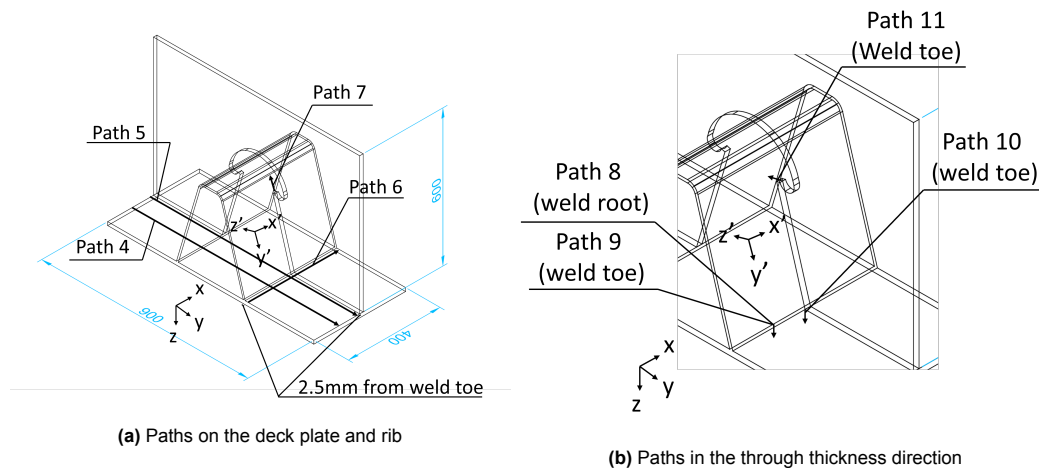


Figure 4.24: Paths along which residual stresses will be presented

Path 4, 5, 6 and 7 are located on the plate surface, while path 8, 9, 10 and 11 are in the through thickness direction. High residual tensile stresses are present along these paths and cracks may originate from locations within the paths. Therefore, the chosen paths will improve the understanding of the residual stress distribution in the specimen. Furthermore, results can be used to improve the accuracy of crack growth rate prediction at critical fatigue details. The location of path 8 represents the detail category at the rib-to-deck connection where a crack originates from the weld root and propagates into the deck plate at a location in between the crossbeams e.g. detail category 100 in table NB.7 of Eurocode 3 part 2 [27]. Path 7 and 11 represent the fatigue detail category at the location of the rib-to-crossbeam connection where a crack originates from the weld toe and propagates into the rib e.g. detail category 80 in Eurocode 3 [13] and detail 3a in the design recommendation ROK 2.0 [14].

Residual stresses after the steps Cooling 2.2, Cooling 10 and Unclamping along Path 4 and 5 are presented in Figure 4.25. Residual tensile stresses of 500 MPa are found at the location of the rib-to-deck connection in path 4 before unclamping and 355 MPa after unclamping. Comparing the residual stress distribution after Cooling 2.2 and after Cooling 10 shows that the addition of the crossbeam has no significant influence on the residual stress distribution. Therefore, stresses in Path 4 can be used to predict fatigue crack growth for the fatigue detail category in between the crossbeams. In Path 5, similar peak residual tensile stresses are present as in Path 4. A constant distribution of tensile stresses of 410 MPa are found near the weld toe of Pass 7 and 9. After Unclamping, the tensile stresses reduce and turn into compressive stresses at the deck plate edges.

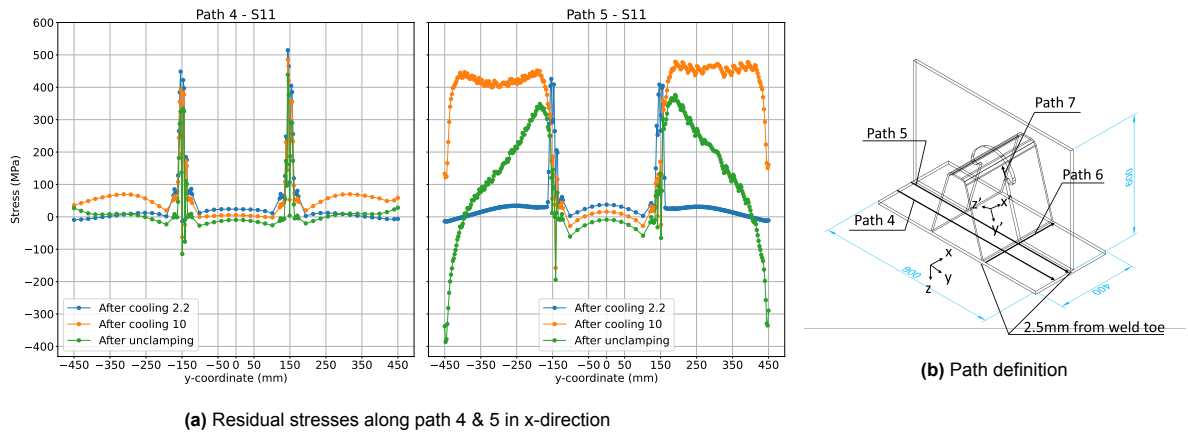


Figure 4.25: Residual stresses along path 4& 5 and path definition

Residual stresses in y-direction along path 6 are presented in Figure 4.26. Stresses along path 6 are also compared to the refined model. High peaks at the location of the crossbeam are found. The peak at 700 MPa is higher than expected and likely a singularity. Comparing results of the refined model and the crossbeam model after Cooling 2.2 shows no significant differences (± 50 MPa).

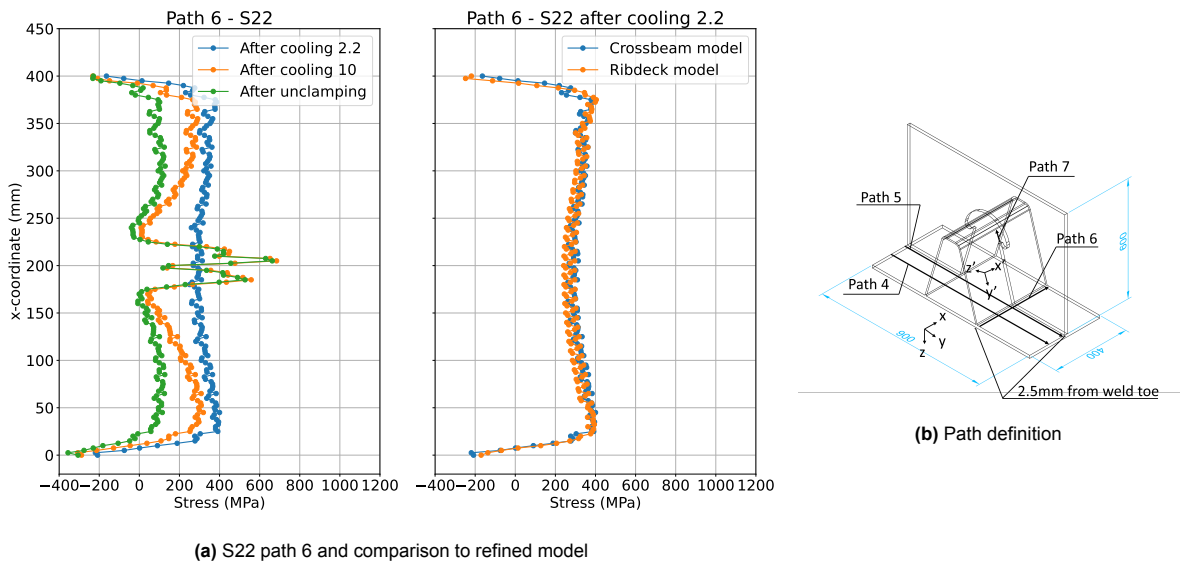


Figure 4.26: Residual stresses along path 6

Stresses along Path 7 in the local y (S_{22}, y') and local z (S_{33}, z') direction are presented in Figure 4.27. High tensile stresses, even higher than the yield strength, are found in y' -direction at the weld toe. The stresses reduce to 40 MPa 40mm in local y direction. In z-direction, the stresses are lower than in y' -direction. At the weld toe, the stress is 80 MPa.

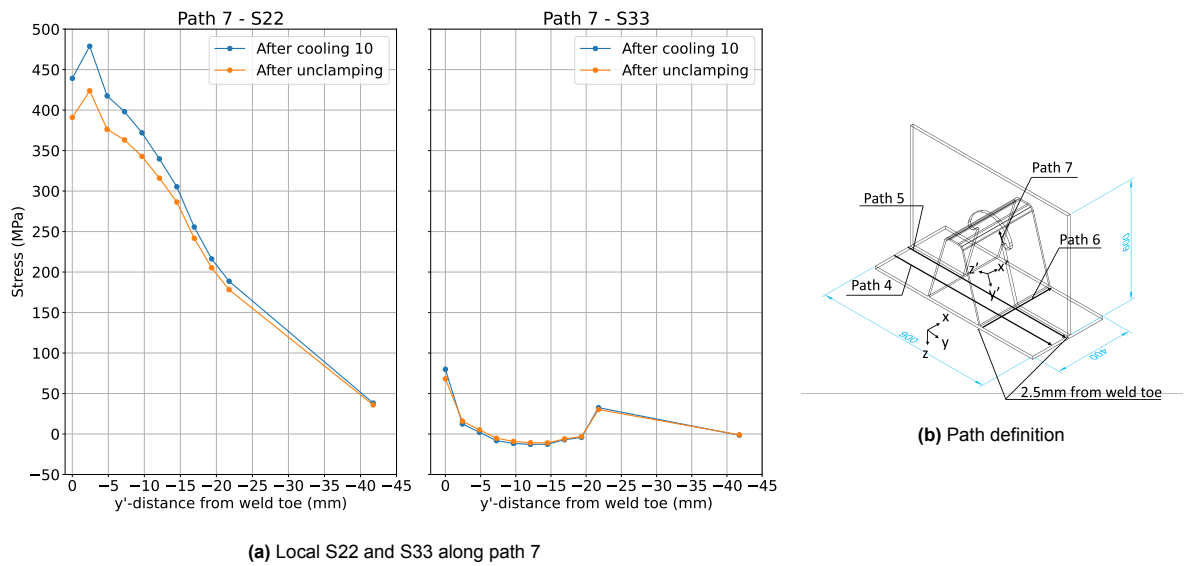


Figure 4.27: Residual stresses along path 7

Residual stresses along Path 8 and 9 are presented in Figure 4.28. S22 stresses are shown in the through-thickness direction. Close to the surface, residual stresses of approximately 250 MPa are found after Cooling 2.2. The stresses are compensated by compressive stresses at larger z-coordinates to make equilibrium. The maximum compressive stress after Unclamping occurs at $z = 7.5\text{mm}$ and is equal to -100 MPa.

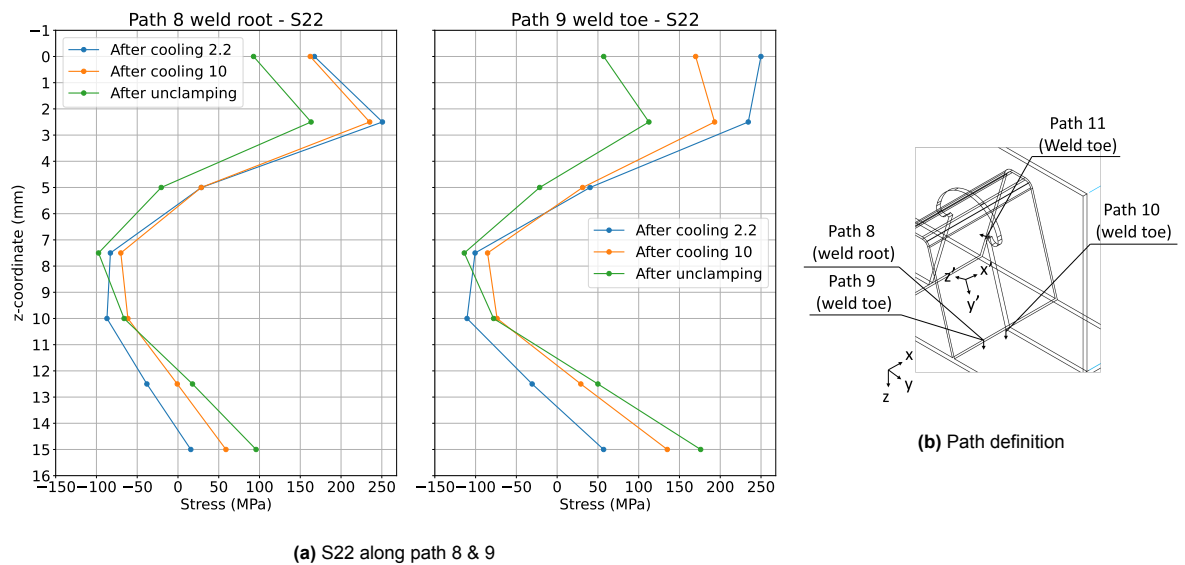


Figure 4.28: Residual stresses along path 8 and 9

The influence of temperature dependent properties along Path 8 and 9 is shown in Figure 4.29. Larger differences are found compared to Figure 4.26. The largest difference occurs at the surface and is equal to 75 MPa. At larger values for z-coordinates, the stresses are similar.

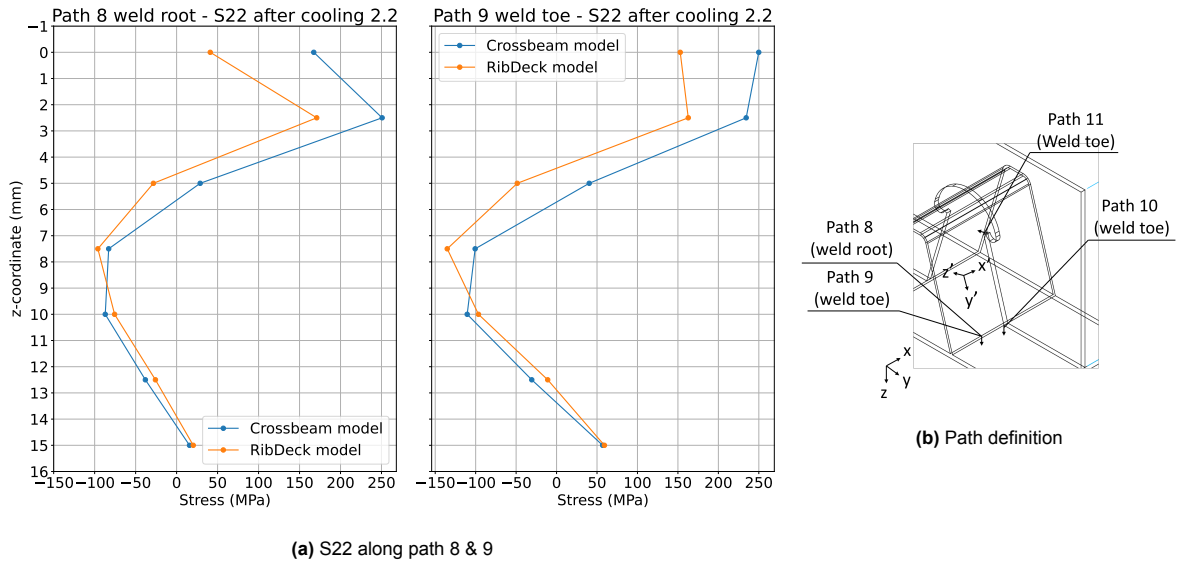


Figure 4.29: Influence temperature dependent thermal properties on residual stresses

Residual stresses along Path 10 in y and z direction are shown in Figure 4.30. Path 10 is at the location of the intersection of pass 1.2 and 7. High tensile stresses in y and z-direction are found. Near the surface, up to 600 MPa in y-direction is obtained. The stresses are tensile over the entire thickness after step Cooling 10 and Unclamping.

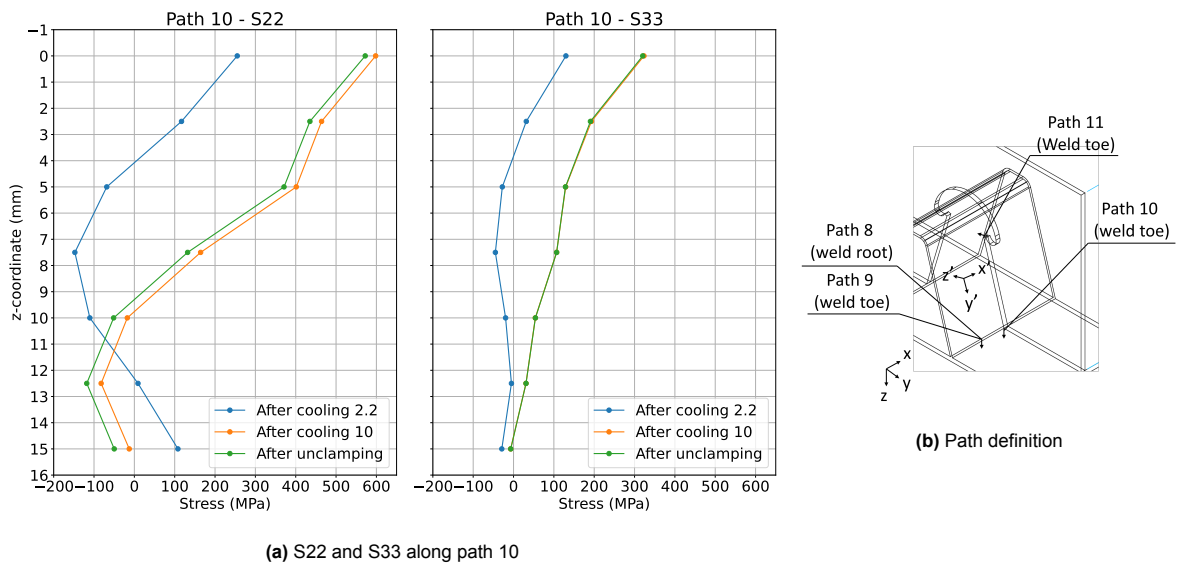


Figure 4.30: S22 and S33 stresses along path 10

Residual stresses along Path 11 in local y (s22, y') and local z-direction (S33, z') are presented in Figure 4.31. Similar to the other paths, residual tensile stresses of yield strength magnitude are found after Unclamping.

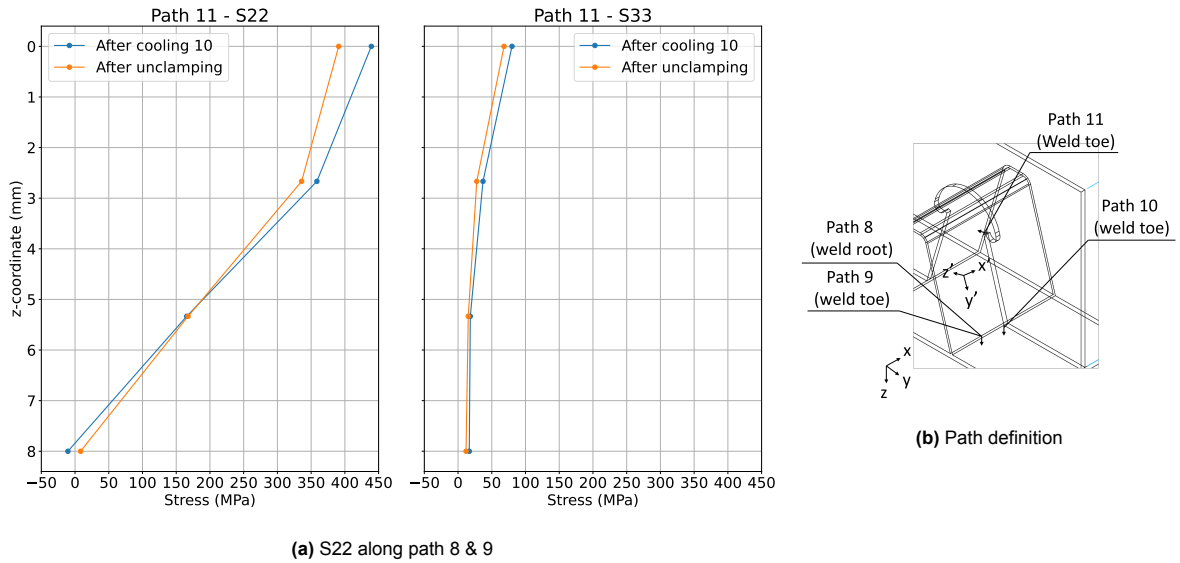


Figure 4.31: S22 and S33 stresses along path 11

Finally, stresses along Path 12 in x-direction are presented and the influence of temperature dependent properties is investigated (see Figure 4.32). The largest deviation is 60 MPa and it occurs at $y = -150$. Small deviations of approximately 25 MPa also occur at $y = -100$ and $y = -160$. Overall, the difference is not significant.

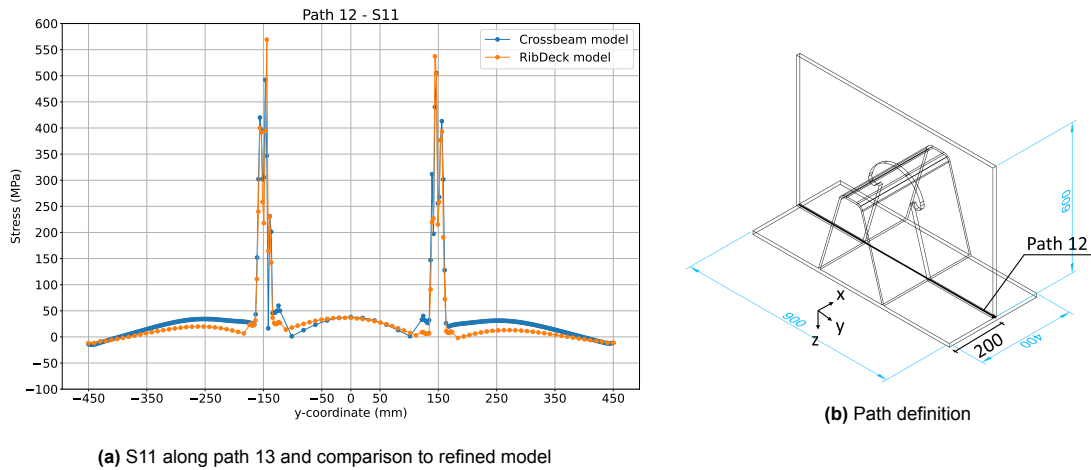


Figure 4.32: S11 along path 12 after cooling 2.2

4.9. Conclusions

A numerical model of the welding experiment has been made in Abaqus FEA. The simulation consisted of a subsequently coupled thermal and mechanical analysis. In the thermal analysis, the heat input from the welding torch was simulated by the Goldak [20] double ellipsoid heat source model (DEHSM) via a user-defined Dflux subroutine. Temperature dependent mechanical properties and temperature independent thermal properties were used. All sides of the 900mmx400mm deck plate were constrained during welding to simulate the welding experiment of Specimen 1. The results were compared to a numerical simulation of the experiment up to the addition of the crossbeam with temperature dependent thermal properties to justify the simplification. The model was validated by temperature and distortion measurements obtained in Chapter 3. Results were also compared to displacements measured in Specimen 3, which was only restrained on the 900mm sides during welding. The conclusions are

listed below.

- Thermal results 1.8s after welding with temperature dependent thermal properties corresponded well to the experimental data. A maximum deviation of 25 °C was found at distances larger than 25 mm behind the last position of the heat source in specimen 1. At the last location of the heat source, a deviation of 65 °C was found compared to the values measured in Specimen 3.
- The recording range of 300-1500C showed best correspondence to predicted values close to the heat source (<20 mm), while the 0-600C range showed best correspondence further away from the heat source.
- Simplifying the model by defining temperature independent properties compared to temperature dependent properties significantly reduced the computation time. Significant differences were found in the temperature distribution 1.8s after welding (480 °C), but no significant differences were found in the deformations before unclamping (0.2 mm) and in the residual stress distribution in the through thickness direction (max. 75 MPa) and in the longitudinal direction (max. 60 MPa).
- The predicted displacements after unclamping corresponded well to experimental data. Measured values in Specimen 3 showed the best correspondence, with a maximum deviation of 0.2 mm. An upward curvature was predicted in between the ribs of the trapezoidal stiffener, while a downward curvature was measured.
- A maximum upward displacement of 1.4mm was obtained from the numerical model.
- At the rib-to-deck connection, stresses reached values of 1.15 times the yield strength before unclamping and the yield strength (355 MPa) after unclamping in longitudinal direction (parallel to the welding direction),
- In the through thickness direction, perpendicular to the welding direction, stresses reached 0.45 times the yield strength (160 MPa) at the weld root after unclamping 2.5mm ($t_{dp}/6$) in the through thickness direction. The stresses are compressive at 7.5mm ($t_{dp}/2$) in the through thickness direction to ensure equilibrium.
- At the rib-to-crossbeam connection, yield stress values were obtained perpendicular to the weld toe after unclamping. The stresses reduced to zero in the through thickness direction.

4.10. Discussion

Large differences (150 °C) were found between the thermal measurements recorded in the 300-1500 °C range and the predicted results at distances larger than 20mm from the last position of the heat source. The thermal measurements recorded in the 0-650 °C range showed significantly better correspondence. This is caused by measurement errors in the 300-1500 °C range. Similar differences were found when comparing results to data from other passes. The 300-1500 °C range is found to be inaccurate for recording temperatures lower than 600 °C in welding scenarios. This can be caused by focusing errors or by calibration errors for lower temperatures or steep temperature gradients. Deviations between predicted and measured displacements were also found. Specimen 1 showed larger deviations to the predicted displacements compared to Specimen 3. This can be caused by initial imperfections in Specimen 1. Another cause could be an inaccuracy in the chosen boundary conditions in the unclamping step. The unclamping is performed in a single step which might favor the less restrained Specimen 3. Unclamping the specimen in four steps, where one workbench weld is removed in each step, might improve the correspondence of displacement values in Specimen 1.

Conclusions & Recommendations

5.1. Conclusions

The main objective of this master thesis is to determine the accuracy of a numerical welding simulation model which predicts welding induced temperature gradients, distortions and residual stresses in a segment of an orthotropic steel deck (OSD). Knowledge about the residual stress distribution is required to increase the accuracy of fatigue life prediction models. The fatigue life prediction was not included in the scope of this thesis. The numerical welding simulation model consists of a subsequently coupled thermo-mechanical analysis. The heat input of the welding torch was substituted by the Goldak double ellipsoid heat source model (DEHSM). Temperature dependent mechanical properties and temperature independent thermal properties were specified. The effect of using temperature independent thermal properties compared to temperature dependent thermal properties on the residual stress distribution was investigated. The model was validated by experimental data. A welding experiment was performed on three specimens consisting of a 900x400mm deck plate, a 350mm deep trapezoidal stiffener and a 600x15mm crossbeam web with a Haibach cope hole. The segment was made of S355 and welded by the gas metal arc welding (GMAW) procedure. During welding, all deck plate sides of Specimen 1 & 2 were constrained. To improve the boundary conditions for representing a full-scale bridge deck, only the 900mm sides were constrained in Specimen 3. Temperatures were recorded by a FLIR® E96 thermal camera during welding. Welding distortions were measured by subtracting the geometry before welding from the geometry after welding. The geometries were obtained by the Artec® LEO 3D scanner. The scans were post-processed in the Artec® studio software and data was extracted with the NumPy-stl package in Python. The raw data was then filtered with the Savitzky-Golay filter. The conclusions are listed below.

- Thermal results 1.8s after welding with temperature dependent thermal properties corresponded well to the experimental data. The maximum recorded temperature was 1042 °C, while the maximum predicted temperature was 975°C. At distances larger than 20mm behind the last position of the heat source, temperatures recorded in the 0-650°C range showed a maximum deviation of 25 °C compared to predicted results, while temperatures recorded in the 300-1500°C range showed a maximum deviation of 175°C.
- Simplifying the model by defining temperature independent properties compared to temperature dependent properties significantly reduced the computation time. Significant differences were found in the temperature distribution 1.8s after welding (480 °C), but no significant differences were found in the deformations before the addition of the crossbeam (0.2mm) and in the residual stress distribution. The relative difference in displacements before the addition of the crossbeam was large (44%). After unclamping, the maximum difference in the residual stress distribution was 75 MPa (0.2 times the yield strength) in the through thickness direction of the deck plate and rib. A difference of 60 MPa (0.17 times the yield strength) was found in the longitudinal direction on the deck plate surface.
- The predicted displacements after unclamping corresponded well to experimental data. Mea-

sured values in Specimen 3 showed the best correspondence, with a maximum deviation of 0.2mm. An upward curvature was predicted in between the ribs of the trapezoidal stiffener, while a downward curvature was measured. The maximum predicted upward displacement was 1.4mm. The maximum upward displacement of Specimen 1 and 3 were 1.5 and 1.39mm, respectively.

- At the rib-to-deck connection, residual stresses on the deck plate reached values of 1.15 times the yield strength before unclamping and the yield strength (355 MPa) after unclamping in longitudinal direction (parallel to the welding direction). Compressive stresses of 25 MPa (0.07 times the yield strength) were found at a distance of 190mm (0.2 times the plate width) from the weld.
- In the through thickness direction, perpendicular to the welding direction, stresses reached 0.45 times the yield strength (160 MPa) at the weld root after unclamping. This value occurred at a distance of 2.5mm ($t_{dp}/6$) in the through thickness direction. Compressive stresses are present at 7.5mm ($t_{dp}/2$) in the through thickness direction to ensure equilibrium.
- At the rib-to-crossbeam connection, yield strength values were obtained in the direction perpendicular to the weld toe after unclamping. The stresses reduced to zero in the through thickness direction.

5.2. Discussion

The recorded temperature range of 300-1500°C showed large deviations for temperatures lower than 600°C compared to the recorded temperature range of 0-650°C and numerical results. This is caused by measurement errors and occurs in all passes. The cause of the measurement errors can be focusing issues or the camera was not well calibrated in this range for measuring lower temperatures or steep temperature gradients. In the measured displacement field, an upward curvature was predicted in between the ribs of the trapezoidal stiffener, while a downward curvature was measured. This can be caused by initial imperfections or by measurement errors, since the differences in this region are within 0.19mm. The spread of the raw data obtained from the scanner was approximately 0.2mm and the parameters used in post-processing and the Savitzky-Golay filter have an influence on the overall result. On one side of the deck plate of Specimen 1, large deviations (1.4mm) between results of Specimen 3 and predicted results were found. This can also be caused by initial imperfections. Another cause can be inaccurate modelling of the unclamping procedure. In the model, a single unclamping step is defined, while the workbench welds were ground side-by-side during the experiment. Defining four unclamping steps in the model will improve the accuracy of the results. However, the sequence was not documented during the experiment. Specimen 3 was only constrained on the 900mm sides. This can cause the better correspondence with predicted results compared to Specimen 1. In Specimen 1, a vertical shift in displacement values was found on the plate edge in longitudinal direction. The values were calibrated to the predicted results and better correspondence was found. The cause for the vertical shift is a difference between the location of the reference coordinate system in the before and after scan. The coordinate system was visually aligned on the workbench surface. It was assumed that workbench surface level was the same in the before and after scan, so subtracting geometries would not lead to a vertical shift. Deviations could have occurred due to visual errors, measurement errors or due to local variations in the workbench surface level. This is a limitation of the methodology and can be resolved by including a levelled surface in the scan to place the reference coordinate system on. Finally, temperature independent thermal properties were used in the model to decrease the computation time. A more refined model with temperature dependent thermal properties showed no significant absolute difference in displacements before the addition of the crossbeam (0.2mm), but it showed a large relative difference (44%). It is assumed that the absolute difference after unclamping is also not significant, but the analysis must be performed to improve certainty. The effect on the residual stress distribution is not significant, so this is only relevant for validation purposes.

5.3. Recommendations

With the obtained results, the following recommendations are made for future research.

- In welding simulation models, the temperature dependent thermal properties can be substituted for temperature independent properties to decrease the computation time when the residual stress distribution is of interest. The maximum difference in the residual stress distribution was

± 0.17 - 0.2 times the yield strength. The difference between displacements before the addition of the crossbeam showed no significant difference in absolute values (0.2mm), but the relative difference was significant (44%). The difference in the temperature distribution 1.8s after welding was significant (480 °C).

- The Artec scanner is a useful and easy to use tool for measuring welding distortions. It is recommended to include a levelled surface in the scan to ensure the location of the reference coordinate system in the before and after scan is the same. The spread of the raw data can be compared to alternative scanners in future research to determine the accuracy.
- The obtained residual stress distribution at the location of the rib-to-crossbeam connection can be predefined in crack propagation simulations to determine the remaining fatigue life. With the obtained fatigue life, the accuracy of the the rib-to-crossbeam fatigue detail in the Schipholbrug can be determined and the requirement for HFMI post weld treatment can be evaluated. In the simulation, the residual stresses can be combined with traffic loading.
- Welding distortions can be measured in a full-scale bridge deck to determine the accuracy of the chosen boundary conditions representing the neighbouring bridge deck. Welding all deck plate sides to the workbench led to over constraint. Fixating four corners at the rib-to-deck connection might be sufficient, because the deck plate of the full-scale bridge deck can move upwards due to its flexibility.
- The accuracy of the numerical model can be improved by decreasing the mesh size. The results can be compared to a model with 8 elements in the thickness direction of the deck plate in the local part and 2 elements in the global part.
- Alternative boundary conditions in the unclamping step could be investigated. The residual stress distribution and the distortion field resulting from the chosen boundary conditions can be compared to symmetric boundary conditions. Second, the removal sequence of the workbench welds can be modelled more accurately. The unclamping phase should consist of four steps. In each step, one workbench weld will be removed. This might improve the fit of the experimental data of Specimen 1 with the numerical results. Finally, a seam can be created between the deck plate and the crossbeam. This will make the mesh between the thermal and mechanical model incompatible, but the residual stress distribution at the weld root of the rib-to-deck joint at the location of the crossbeam can be determined. Cracks were found at this location in the van Brienoordbrug.
- The effect of different welding parameters and geometries on the residual stress distribution and distortion field can be investigated. The objective would be to optimize the welding process for the geometry to minimize the introduction of residual tensile stresses.

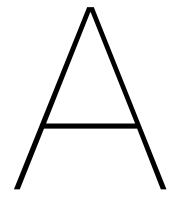
References

- [1] Dean Deng, Hidekazu Murakawa, and Wei Liang. "Numerical simulation of welding distortion in large structures". In: *Computer Methods in Applied Mechanics and Engineering* 196.45 (2007), pp. 4613–4627. ISSN: 0045-7825. DOI: <https://doi.org/10.1016/j.cma.2007.05.023>. URL: <https://www.sciencedirect.com/science/article/pii/S0045782507002320>.
- [2] Koichi Masubuchi. *Analysis of Welded Structures - Residual stresses, distortion and their Consequences*. Oxford, England: Pergamon Press, 1980.
- [3] Asma Manai, Rüdiger Ulrich Franz von Bock und Polach, and Mohammad Al-Emrani. "A probabilistic study of welding residual stresses distribution and their contribution to the fatigue life". In: *Engineering Failure Analysis* 118 (2020), p. 104787. ISSN: 1350-6307. DOI: <https://doi.org/10.1016/j.engfailanal.2020.104787>. URL: <https://www.sciencedirect.com/science/article/pii/S1350630719317182>.
- [4] H. Xin and M. Veljkovic. "Effects of residual stresses on fatigue crack initiation of butt-welded plates made of high strength steel". English. In: *Advances in Engineering Materials, Structures and Systems*. Ed. by Alphose Zingoni. 7th International Conference on Structural Engineering, Mechanics and Computation, 2019 ; Conference date: 02-09-2019 Through 04-09-2019. CRC Press / Balkema - Taylor & Francis Group, 2019, pp. 1260–1265. ISBN: 9781138386969. DOI: [10.1201/9780429426506-218](https://doi.org/10.1201/9780429426506-218).
- [5] G.A. Webster and A.N. Ezeilo. "Residual stress distributions and their influence on fatigue lifetimes". In: *International Journal of Fatigue* 23 (2001), pp. 375–383. ISSN: 0142-1123. DOI: [https://doi.org/10.1016/S0142-1123\(01\)00133-5](https://doi.org/10.1016/S0142-1123(01)00133-5).
- [6] Evy Van Puymbroeck et al. "Residual weld stresses in stiffener-to-deck plate weld of an orthotropic steel deck". In: *Journal of Constructional Steel Research* 159 (2019), pp. 534–547. ISSN: 0143-974X. DOI: <https://doi.org/10.1016/j.jcsr.2019.05.015>. URL: <https://www.sciencedirect.com/science/article/pii/S0143974X18306837>.
- [7] S.J. Maddox. *Fatigue Strength of Welded Structures*. Series in Welding and Other Joining Technologies. Elsevier Science, 1991. ISBN: 9781855730137. DOI: <https://doi.org/10.1016/C2013-0-17455-7>.
- [8] Jean-Paul Lebet and Manfred A.Hirt. *Steel Bridges - Conceptual and Structural Design of Steel and Steel-Concrete Composite Bridges*. EPFL Press, 2013. ISBN: 978-1-4665-7297-3. DOI: <https://doi-org.tudelft.idm.oclc.org/10.1201/b15429>.
- [9] Hyoung-Bo Sim, Chia-Ming Uang, and Charles Sikorsky. "Effects of Fabrication Procedures on Fatigue Resistance of Welded Joints in Steel Orthotropic Decks". In: *Journal of Bridge Engineering* 14.5 (2009), pp. 366–373. DOI: [10.1061/\(ASCE\)1084-0702\(2009\)14:5\(366\)](https://doi.org/10.1061/(ASCE)1084-0702(2009)14:5(366)). eprint: [https://ascelibrary.org/doi/pdf/10.1061/\(ASCE\)1084-0702\(2009\)14:5\(366\)](https://ascelibrary.org/doi/pdf/10.1061/(ASCE)1084-0702(2009)14:5(366)). URL: [https://ascelibrary.org/doi/abs/10.1061/\(ASCE\)1084-0702\(2009\)14:5\(366\)](https://ascelibrary.org/doi/abs/10.1061/(ASCE)1084-0702(2009)14:5(366)).
- [10] F.B.P de Jong. "Overview fatigue phenomenon in orthotropic bridge decks in the Netherlands". In: *2004 Orthotropic Bridge Conference* (2004).
- [11] Johan Maljaars, Frank van Dooren, and Henk Kolstein. "Fatigue assessment for deck plates in orthotropic bridge decks". In: *Steel Construction* 5.2 (2012), pp. 93–100. DOI: <https://doi.org/10.1002/stco.201210011>. eprint: <https://onlinelibrary.wiley.com/doi/pdf/10.1002/stco.201210011>. URL: <https://onlinelibrary.wiley.com/doi/abs/10.1002/stco.201210011>.
- [12] Wim Nagy. "Fatigue Assessment of Orthotropic Steel Decks Based on Fracture Mechanics". <http://hdl.handle.net/1854/LU-8602473>. PhD thesis. Universiteit Gent, May 2017.
- [13] CEN. *Design of steel structures - Part 1-9: Fatigue*. Tech. rep. Jan. 2006.
- [14] Jean-Luc Beguin, Sonja Fennis, and Bas Bongaerts. *Richtlijn ontwerp kunstwerken - ROK2.0 concept*. Rijkswaterstaat, 2021. URL: <https://standaarden.rws.nl/index.html>.

- [15] Chaminda S. Bandara et al. "Developing a full range S–N curve and estimating cumulative fatigue damage of steel elements". In: *Computational Materials Science* 96 (2015), pp. 96–101. ISSN: 0927-0256. DOI: <https://doi.org/10.1016/j.commatsci.2014.09.009>. URL: <https://www.sciencedirect.com/science/article/pii/S092702561400620X>.
- [16] Chuang Cui et al. "Strain Energy-Based Fatigue Life Evaluation of Deck-to-Rib Welded Joints in OSD Considering Combined Effects of Stochastic Traffic Load and Welded Residual Stress". In: *Journal of Bridge Engineering* 23.2 (2018), p. 04017127. DOI: [10.1061/\(ASCE\)BE.1943-5592.0001181](https://doi.org/10.1061/(ASCE)BE.1943-5592.0001181). eprint: <https://ascelibrary.org/doi/pdf/10.1061/%28ASCE%29BE.1943-5592.0001181>. URL: <https://ascelibrary.org/doi/abs/10.1061/%5C%28ASCE%5C%29BE.1943-5592.0001181>.
- [17] Gary S. Schajer. *Practical Residual Stress Measurement Methods*. Vancouver, Canada: John Wiley & Sons, Incorporated, 2013. ISBN: 9781118402825. URL: <http://ebookcentral.proquest.com/lib/delft/detail.action?docID=1380176>.
- [18] John A. Goldak and Mehdi Akhlaghi. *Computational Welding Mechanics*. New York, NY: Springer, 2005. ISBN: 978-0387-23287-4.
- [19] Kimiya Hemmesi and Majid Farajian. "Numerical Welding Simulation as a Basis for Structural Integrity Assessment of Structures: Microstructure and Residual Stresses". In: (). DOI: <http://dx.doi.org/10.5772/intechopen.74466>.
- [20] John Goldak, Aditya Chakravarti, and Malcolm Bibby. "A new finite element model for welding heat sources". In: *Metallurgical Transactions B* 15.2 (June 1984), pp. 299–305. ISSN: 1543-1916. DOI: [10.1007/BF02667333](https://doi.org/10.1007/BF02667333). URL: <https://doi.org/10.1007/BF02667333>.
- [21] Jaap Schijve. *Fatigue of Structures and Materials*. Springer, 2009. ISBN: 978-1-4020-6807-2. URL: <https://dx.doi.org/10.1007/978-1-4020-6808-9>.
- [22] Michael D. Sangid. "The physics of fatigue crack initiation". In: *International Journal of Fatigue* 57.10 (2013). Available at: <https://doi.org/10.1016/j.ijfatigue.2012.10.009>, pp. 58–72.
- [23] P. Paris and F. Erdogan. "A Critical Analysis of Crack Propagation Laws". In: *Journal of Basic Engineering* 85.4 (Dec. 1963), pp. 528–533. ISSN: 0021-9223. DOI: [10.1115/1.3656900](https://doi.org/10.1115/1.3656900). eprint: https://asmedigitalcollection.asme.org/fluidsengineering/article-pdf/85/4/528/5763569/528_1.pdf. URL: <https://doi.org/10.1115/1.3656900>.
- [24] Joseph. R. Davis. *Metals Handbook Desk Edition, 2nd edition*. ASM International, 1998. ISBN: 978-0-87170-654-6.
- [25] Željko Božić, Marijo Mlikota, and Siegfried Schmauder. "Application of the ΔK , ΔJ and $\Delta CTOD$ parameters in fatigue crack growth modelling". In: *Technical Gazette* 3.18 (2011), pp. 459–466.
- [26] A.F. Hobbacher. *Recommendations for Fatigue Design of Welded Joints and Components*. Available at: <https://doi.org/10.1007/978-3-319-23757-2>. 2019.
- [27] NEN. *Design of steel structures - Part 2: Steel bridges Dutch national annex*. Tech. rep. Dec. 2011.
- [28] H.E. Coules and P. Colegrove. "Characterising the effects of high-pressure rolling on residual stress in structural steel welds". PhD thesis. Cranfield University, 2012.
- [29] Niels van den Berg. "Effects of residual stresses on the fatigue crack propagation of an orthotropic steel bridge deck". Available at: <http://resolver.tudelft.nl/uuid:753e6f58-8dcd-431e-b20b-f32820d18ad8>. MA thesis. Delft University of Technology, 2020.
- [30] W. Nagy et al. "Measuring Residual Stresses in Orthotropic Steel Decks Using the Incremental Hole-Drilling Technique". In: *Experimental Techniques* 41.3 (June 2017), pp. 215–226. ISSN: 1747-1567. DOI: [10.1007/s40799-017-0169-2](https://doi.org/10.1007/s40799-017-0169-2). URL: <https://doi.org/10.1007/s40799-017-0169-2>.
- [31] Xiaohua Cheng et al. "Residual stress modification by post-weld treatment and its beneficial effect on fatigue strength of welded structures". In: *International Journal of Fatigue* (2003), pp. 1259–1269. ISSN: 0142-1123. DOI: <https://doi.org/10.1016/j.ijfatigue.2003.08.020>.
- [32] Youliang Ding et al. "Fatigue Life Evaluation of Welded Joints in OSD for Railway Bridges Considering Welding Residual Stress". In: *Journal of Performance of Constructed Facilities* 33.2 (2019), p. 04018111. DOI: [10.1061/\(ASCE\)CF.1943-5509.0001262](https://doi.org/10.1061/(ASCE)CF.1943-5509.0001262). eprint: <https://ascelibrary.org/doi/pdf/10.1061/%28ASCE%29CF.1943-5509.0001262>. URL: <https://ascelibrary.org/doi/abs/10.1061/%5C%28ASCE%5C%29CF.1943-5509.0001262>.
- [33] Philipp Rettenmeier, Eberhard Roos, and Stefan Weihe. "Fatigue analysis of multiaxially loaded crane runway structures including welding residual stress effects". In: *International Journal of*

- Fatigue* 82 (2016). 10th Fatigue Damage of Structural Materials Conference, pp. 179–187. ISSN: 0142-1123. DOI: <https://doi.org/10.1016/j.ijfatigue.2015.04.009>. URL: <https://www.sciencedirect.com/science/article/pii/S0142112315001255>.
- [34] Xue-fang Xie et al. “A model to predict the relaxation of weld residual stress by cyclic load: Experimental and finite element modeling”. In: *International Journal of Fatigue* 95 (2017), pp. 293–301. ISSN: 0142-1123. DOI: <https://doi.org/10.1016/j.ijfatigue.2016.11.011>. URL: <https://www.sciencedirect.com/science/article/pii/S0142112316303747>.
- [35] Chuang Cui et al. “Fatigue life evaluation of welded joints in steel bridge considering residual stress”. In: *Journal of Constructional Steel Research* 153 (Nov. 2018), pp. 509–518. DOI: [10.1016/j.jcsr.2018.11.003](https://doi.org/10.1016/j.jcsr.2018.11.003).
- [36] Roberto Montanari, Alessandra Fava, and Giuseppe Barbieri. “Experimental Techniques to Investigate Residual Stress in Joints”. In: (2018).
- [37] American Society for Testing and Materials. *ASTM E 837-95; Standard Test Method for Determining Residual Stresses by the Hole-Drilling Strain-Gage Method*. 1996.
- [38] Vishay. “Measurement of Residual Stresses by the Hole-Drilling Strain Gage Method”. In: (2010). URL: <http://www.vishaypg.com/docs/11053/tn503.pdf>.
- [39] Ying Gu et al. “Numerical Simulation and Measurement of Welding Residual Stresses in Orthotropic Steel Decks Stiffened with U-Shaped Ribs”. In: *International Journal of Steel Structures* 20.3 (June 2020), pp. 856–869. ISSN: 2093-6311. DOI: [10.1007/s13296-020-00327-3](https://doi.org/10.1007/s13296-020-00327-3). URL: <https://doi.org/10.1007/s13296-020-00327-3>.
- [40] Kallia Spyridoni. “Prediction of residual stress of an orthotropic plate due to welding”. Available at: <http://resolver.tudelft.nl/uuid:76087661-ed45-4df4-b7e6-8fc0cd6164da>. MA thesis. 2019.
- [41] Suraj Joshi et al. “Characterization of material properties and heat source parameters in welding simulation of two overlapping beads on a substrate plate”. In: *Computational Materials Science* 69 (2013), pp. 559–565. ISSN: 0927-0256. DOI: <https://doi.org/10.1016/j.commatsci.2012.11.029>. URL: <https://www.sciencedirect.com/science/article/pii/S092702561200688X>.
- [42] Simulia. *Abaqus 6.14 Documentation - Abaqus Theory Guide*.
- [43] Haohui Xin and Milan Veljkovic. “Residual stress effects on fatigue crack growth rate of mild steel S355 exposed to air and seawater environments”. English. In: *Materials & Design* 193 (2020). ISSN: 0264-1275. DOI: [10.1016/j.matdes.2020.108732](https://doi.org/10.1016/j.matdes.2020.108732).
- [44] Evy Van Puymbroeck. “Residual stresses in welded bridge components determined by the incremental hole-drilling method and finite element modelling”. eng. PhD thesis. Ghent University, 2019, p. 234. ISBN: 9789463552769.
- [45] FLIR. *Advanced thermal imaging camera - FLIR E96*. <https://www.flir.com/products/e96/>. Accessed: 18-Mar-2022. 2022.
- [46] Artec Group. *Wireless Handheld 3D scanner - Artec Leo*. <https://www.artec3d.com/portable-3d-scanners/artec-leo>. Accessed: 18-Mar-2022. 2022.
- [47] Artec Studio 16. Available at: <http://docs.artec-group.com/as/16/en/?msclkid=2792fb50a69911ec844581bf1c2c9951>. Artec Group. 2021.
- [48] FLIR. *FLIR Research Studio*. <https://www.flir.com/products/flir-research-studio/>. Accessed: 21-Mar-2022.
- [49] Rick van Hattem. *numpy-stl 2.16.3*. <https://pypi.org/project/numpy-stl/>. Accessed: 22-Mar-2022.
- [50] *scipy.signal.savgol_filter*. https://docs.scipy.org/doc/scipy/reference/generated/scipy.signal.savgol_filter.html. Accessed: 22-Mar-2022.
- [51] Abraham. Savitzky and M. J. E. Golay. “Smoothing and Differentiation of Data by Simplified Least Squares Procedures.” In: *Analytical Chemistry* 36.8 (1964), pp. 1627–1639. DOI: [10.1021/ac60214a047](https://doi.org/10.1021/ac60214a047). eprint: <https://doi.org/10.1021/ac60214a047>. URL: <https://doi.org/10.1021/ac60214a047>.
- [52] M. R. Frewin and D. A. Scott. “Finite Element Model of Pulsed Laser Welding”. In: *Welding Research Supplement* (1999), pp. 15–22. URL: <https://www.fdp.nl/cmsfiles/vulcanus/model.pdf%7D>.
- [53] *Goldak heat input model for Welding and Additive Manufacturing process*. <https://youtu.be/G1wsgnay8kA>. Accessed: 2022-Jan-4.

- [54] S. B. Brown and H. Song. "Implications of Three-Dimensional Numerical Simulations of Welding of Large Structures". In: *Welding Research Supplement* (1992), pp. 55–62. URL: https://app.aws.org/wj/supplement/WJ_1992_02_s55.pdf.
- [55] N. Torić, B. Peroš, and I. Boko. "Fire resistance analysis of steel structures". In: *GRAĐEVINAR* 64 (8 2012), pp. 631–640. DOI: <https://doi.org/10.14256/JCE.712.2011>.
- [56] CEN. *Eurocode 3: Design of steel structures - Part 1-2: General rules -Structural fire design*. Tech. rep. Apr. 2004.



IABSE conference paper

Experimental investigations of welding induced temperature gradients and distortions in a segment of an OSD

Arvid Maarleveld, David Malschaert, Milan Veljkovic

Faculty of Civil Engineering and Geosciences, Delft University of Technology, 2628CN, Delft, the Netherlands

Contact: a.maarleveld@student.tudelft.nl

Abstract

Orthotropic bridge decks are susceptible to fatigue cracks which are influenced by the thickness of their components, welding procedure, type of the weld, the position of the considered detail in relation to the local loading condition and by residual stresses due to welding. The above-mentioned parameters determine the detail category for fatigue resistance. This research focuses on an experimental investigation of the temperature distribution and distortions due to the welding of a connection between the deck plate, longitudinal stiffener and crossbeam. Three specimens were welded with dimensions of: 900x400 mm deck plate, 350mm deep trapezoidal longitudinal stiffener and 600mm long crossbeam in a workshop of a bridge fabricator. The crossbeams were manufactured with Haibach cope holes. The thickness of the deck plate and crossbeam was 15 mm, and the thickness of the longitudinal stiffener was 8mm. During the welding, the temperature was measured using a FLIR® E96 camera. The distortions were measured using an Artec Leo® scanner by comparing the initial state and the state after welding. 1.8 seconds after welding, steep temperature gradients were measured with a maximum of 1042°C. After cooling, a maximum upward displacement of 1.3 mm of the deck plate was measured. The main motivation of the experiments performed is to create a database for validation of a numerical model for the fatigue life prediction, which is left out of the scope of this paper. The order of magnitude of the deformation field is comparable to experiments found in the literature, although the results can not be directly compared due to geometry, welding, and material differences.

Keywords: residual stresses; welding; distortions; OBD; fatigue

1 Introduction

Due to their relatively high stiffness and low self-weight, orthotropic bridge decks (OBD) have been widely used in movable and long-span bridges [1]. An OBD consists of a deck plate, longitudinal stiffeners (rib), crossbeams and main girders, as shown in figure 2. Despite its advantages, the manufacturing process may lead to distortions and imperfections [2,3]. Furthermore, fatigue cracks have been observed in the welded connections in various bridges [4]. In figure 2 and 3, examples are

shown of cracks that have been detected in the rib-to-deck and the rib-to-crossbeam connection, including a Haibach cope hole. These cracks can be formed in locations of high-stress concentration and/or local defects and are influenced by residual stresses [5,6].

Welding induced residual stresses can reach the yield stress and are formed by steep temperature gradients and the restrained thermal shrinkage during the cooling [6,7]. Residual stresses have a large influence on fatigue life and therefore

knowledge of the distribution is required for accurate fatigue assessment [8]. Several experimental, as well as numerical methods have been established to determine residual stresses. The incremental hole-drilling method is popular due to its ease of use. It was used by many researchers including van Puymbroeck et. al [9] and Gu et al. [10]. In the latter research, results were compared to a finite-element model based on a subsequently coupled thermo-mechanical finite-element model where the heat source was substituted by the Goldak [11] double ellipsoid heat source model (DEHSM). Deviations between experimental and numerical results were within 20 MPa. Distortions have also been measured in recent research. This knowledge is required to take appropriate distortion control measures and to derive residual stresses from the deformation field. Deng et al. [2] measured distortions of a thin plated specimen by tracking coordinates of targets with a 3D photography technique, while Sim et al. [1] measured distortions in full-scale bridge deck specimens with a laser tracking system.

The residual stress distribution depends on many factors including welding parameters, welding speed, chemical composition of the steel, resultant weld geometry and weld toe radius [12]. To be able to gain confidence in reducing the complexity of finite element models by applying simplifications and/or assumptions, validation with experimental research is required.

This research aims to establish an experimental methodology and a database of temperature gradients and distortions in a segment of an OBD. Thermal measurements are performed by a FLIR E96 thermal camera. Distortions are derived from 3D geometry scans by use of an Artec Leo scanner.

Firstly, the specimen characteristics and experimental set-up are discussed followed by the methodology. Finally, thermal- and distortion results are presented.

2 Methodology

2.1 Specimen characteristics

Three specimens have been manufactured with dimensions shown in figure 4. Each specimen was made out of S355J2+N. The specimens were

welded by gas metal arc welding (GMAW). The shielding gas consisted 80% out of Argon and 20% out of CO₂. The gas flow rate was between 15 and 20 L/min. The used filler wire type was Diamondspark 52RC (1.2 mm) for the vertical passes and MC715H (1.2mm) for all other passes.

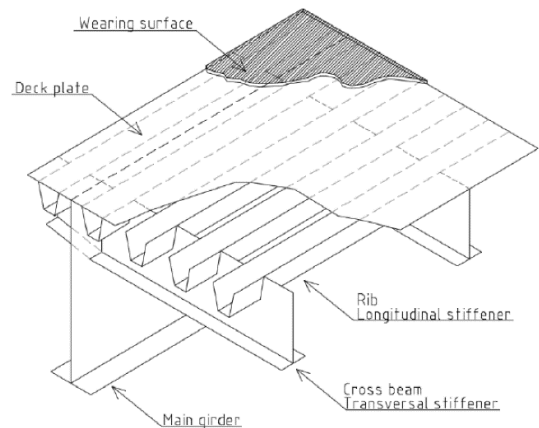


Figure 1. Orthotropic steel deck overview [13]

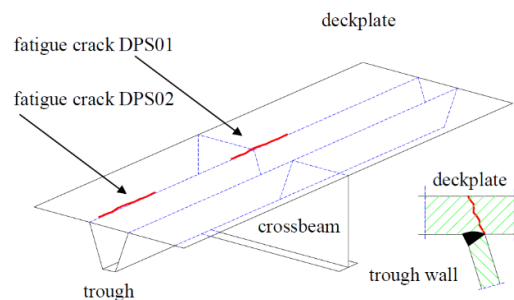


Figure 2. Crack in the rib-to-deck connection [4]

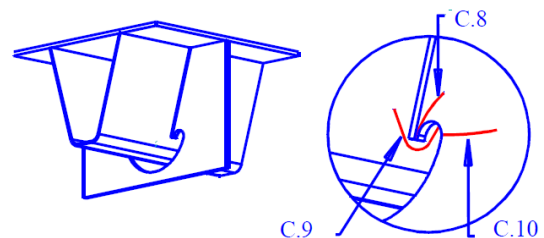


Figure 3. Crack in the rib-crossbeam connection with cope hole [4]

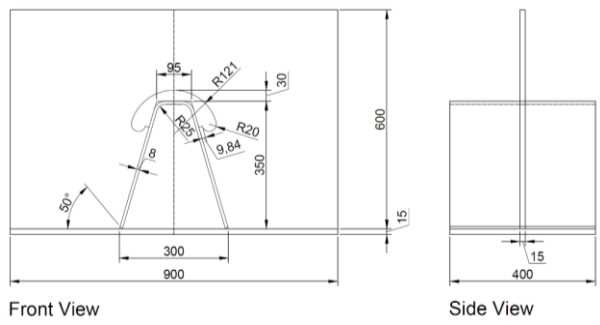


Figure 4. Specimen dimensions

2.2 Experimental set-up and measuring equipment

The experimental set-up is shown in figure 5. The temperatures were measured using a thermosensitive FLIR E96 camera which was placed on a tripod during the welding of specimens. Radiometric video was recorded at 30 fps with a resolution of 640x480 pixels. During welding, the sensor was covered to protect it from the high radiation emitted by the welding torch. After welding, the sensor was uncovered in order to measure the temperature directly after welding. The accuracy of the measurements is $\pm 2^\circ\text{C}$ or $\pm 2\%$ [14]. Three temperature ranges could be selected, -20°C to 120°C , 0°C to 600°C and 300°C to 1500°C . The temperature ranges of $0-600^\circ\text{C}$ and $300-1500^\circ\text{C}$ were used during the experiment to capture the entire temperature scale. For distortion measurements, an Artec LEO 3D scanner was used. The Artec Leo scanner captures 3 million data points per second with an accuracy of up to 0.1mm. Frames are reconstructed from these points, from which a 3D model is made. The HD scanning algorithm was enabled, which uses more polygons per frame for data processing, leading to denser and higher quality 3D data. A 3D resolution of up to 0.2mm can be achieved with this mode. In the scanner settings, HD mode was enabled and set to 1/8, meaning that for every 8 frames, one frame was reconstructed in HD mode [15]. By comparing scans before and after welding, distortions will be obtained.

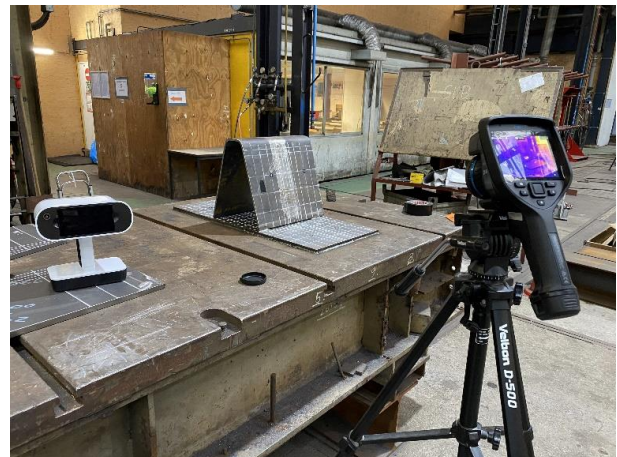


Figure 5. Experimental set-up

2.3 Experimental procedure

During the experiment, the welding- and cooling time, power input and wire feeding speed were documented. The temperature of all welding passes was recorded with the FLIR E96 thermal camera. During welding, the sides of the deck plate were constrained by welding it to the workbench to simulate neighbouring bridge deck behaviour. For representing an OBD part, these welds between the workbench and the deck plate lead to over constraint. Therefore, for specimen 3, the welds of 400 mm long were removed, and the effect of these boundary conditions was investigated. The following actions have been taken during the experiment for each specimen.

1. Welding of the deck plate to the workbench.
2. Applying tack welds (see figure 6).
3. Scanning of 3D geometry.
4. (Specimen 3) remove workbench welds of length 400 mm.
5. Weld pass 1.1-2.2 (see figure 7).
6. Scan 3D geometry.
7. Placing of the crossbeam and tack welds (see Figure 8).
8. Scan 3D geometry.
9. Weld passes 3-10.
10. Scan 3D geometry.
11. Removing of welds connecting specimen to workbench.

12. Scan 3D geometry.

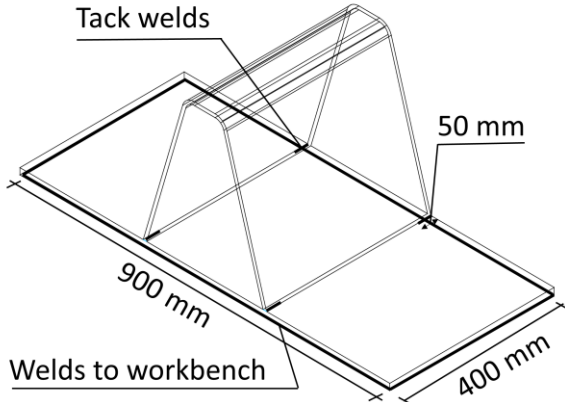


Figure 6. Location and length of tack welds before welding

2.4 Data processing

Radiometric video has been processed in FLIR research studio 2.0 software. In the software, thermal images of each frame can be exported, and the temperature range and color palette can be changed. Various regions of interest (ROI) can also be defined, such as a point, a line, a rectangle or a circle. Temperature values 1.8 seconds after welding along a line perpendicular and parallel to pass 1.1 have been exported, as well as a maximum temperature value in time in a box around the melting pool.

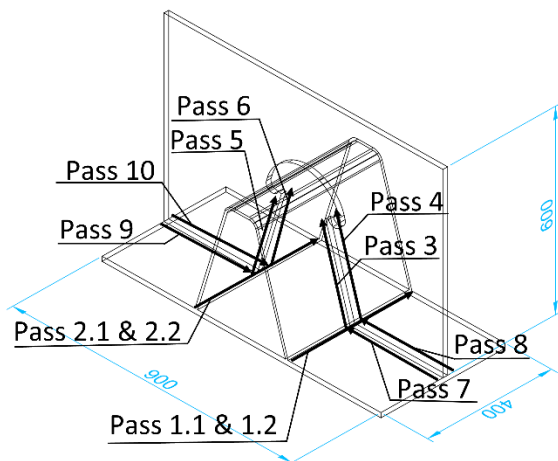


Figure 7. Welding procedure, passes

The geometry scans were post-processed in the Artec Studio 16 Professional software [15]. The post-processing steps and settings are as follows.

1. Import the scan, set HD data density to 4x.
2. Apply the global registration algorithm. This algorithm converts all one-frame surfaces into a single coordinate system.
 - a. Features: Geometry and texture
 - b. Search features within: 5mm
3. Apply the outlier removal algorithm. This removes 3D noise.
 - a. 3D-noise-level: 3
 - b. 3D resolution: 0.2mm
4. Apply sharp fusion. This fuses all frames in a single polygonal 3D model.
 - a. 3D resolution: 0.2mm
 - b. Fill holes with radius ≤ 5 mm
5. Use the positioning tool and the transformation tool to place the coordinate system on the work bench surface, with the x-direction in the direction of pass 1.1 and the z-direction downwards.

The resulting model consisting of 74 million polygons and the location of the coordinate system is shown in figure 9. Additional images of the weld geometry before and after welding are shown in figure 10 and 11. Finally, the polygonal 3D model was exported to an .stl file, which contains all coordinates of the polygonal nodes in millimeters.

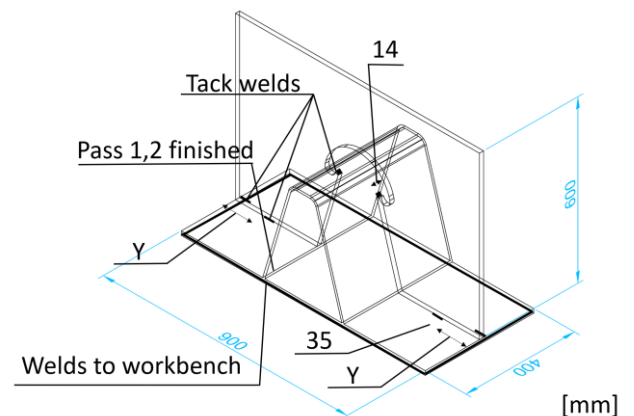


Figure 8. Tack welds after fitting the crossbeam. Distance Y is 140-180mm, depending on the specimen

With the NumPy-stl package in Python, the z-coordinates of the polygonal nodes were extracted

and plotted along three paths. The paths are shown in figure 15.

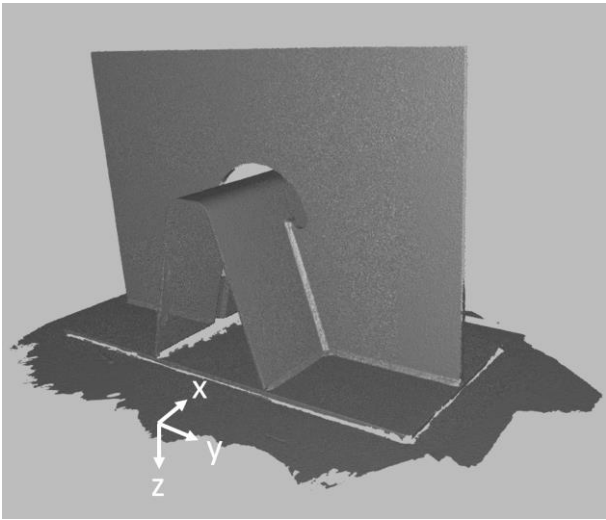


Figure 9. Polygonal 3D model in Artec studio software

This resulted in approximately 13000 points along path 1. The scattered data was filtered in Python with the Savitzky-Golay algorithm with a window size of 1999 points and a 3rd degree polynomial. The result can be found in figure 16.

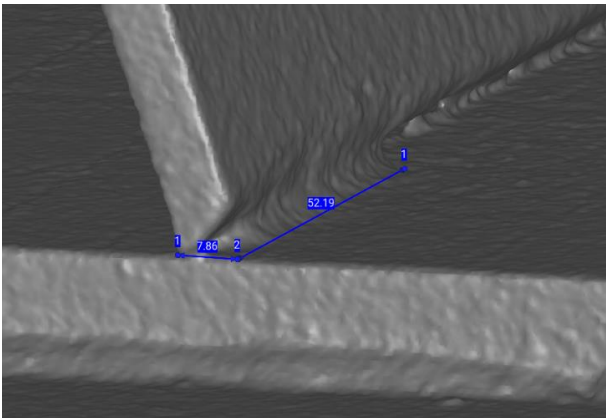


Figure 10. Tack weld geometry

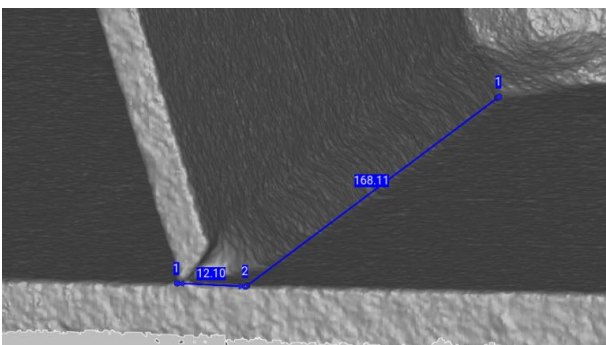


Figure 11. Final weld geometry

3 Results

3.1 Temperature

A thermal image 1.8s after the pass 1.1 in specimen 3 is shown in figure 12. The maximum recorded temperature was 1042 °C, which is around the melting point of steel.

In figure 13, maximum temperatures are shown at a distance x and y from the heat source, 1.8 sec after the welding. In figure 14, the maximum temperature as a function of time in box B1 is shown. While the temperature recording range in specimen 3 was set to 300-1500C, values up to 150C were recorded. Values in specimen 3 are significantly larger at a distance of -300 to -50 mm from the heat source compared to specimen 1 in figure 13. In specimen 1, the measured values are closer to the expected values. Both recording ranges have an accuracy of +2%, according to the manufacturer. Focussing issues might occur in the high recording temperature range, or the specimen cools down too quickly to obtain an accurate reading in this range. No explanations can be found in the manual of the camera.

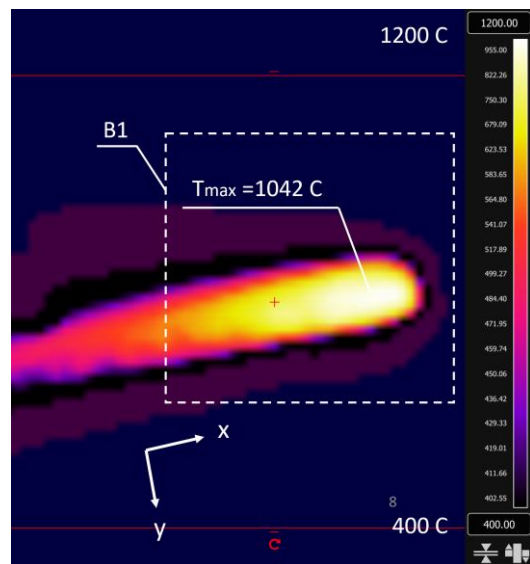


Figure 12. Thermal image specimen 3 1.8s after welding

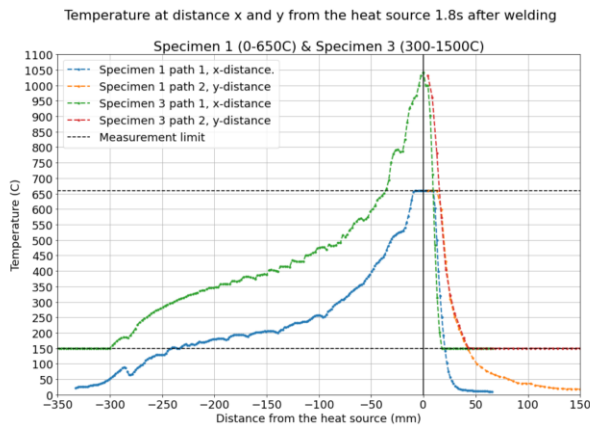


Figure 13. Temperature values at a distance x and distance y from the heat source at 1.8s after welding

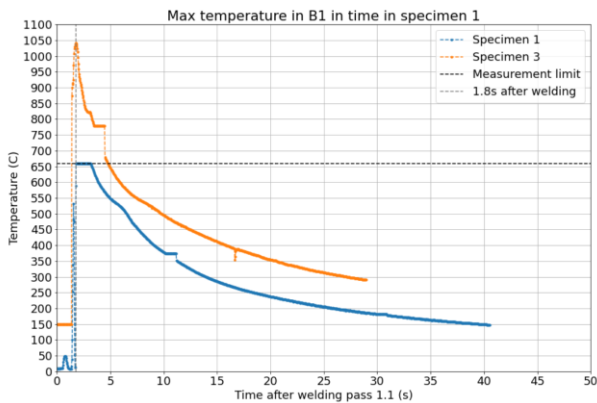


Figure 14. Maximum temperature as a function of time

3.2 Distortions

For each specimen, the z -coordinates of the polygonal nodes of the 3D model were extracted. The coordinates are plotted along path 1, 2 and 3, as defined in figure 15. Coordinates within a range of 1mm are plotted. So, for path 1, coordinates between $x = 20$ and 21 mm from the start of the deck plate are plotted and for path 2, the coordinates are between $y = 10$ and 11 mm from the weld toe. By comparing the coordinates from the scan before welding and the scan after releasing the constraints, welding distortions are obtained.

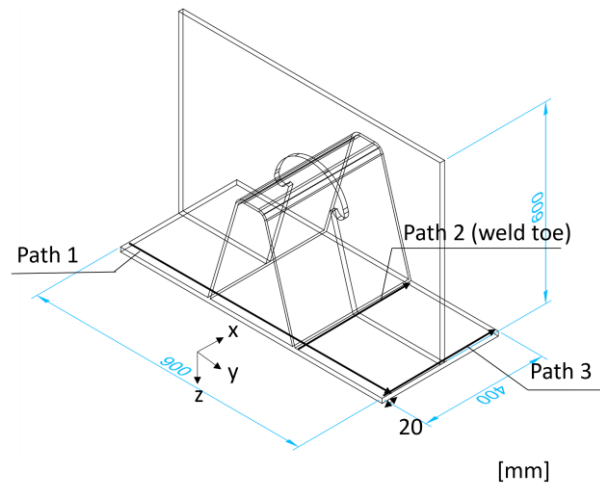


Figure 15. Paths along which z -coordinates are plotted

The resulting scattered data is filtered by the Savitzky-Golay procedure to obtain a smooth curve. The results for path 1, 2 and 3 are shown in figure 16, 18 and 19, respectively. The top figure shows the geometry with a large z -axis scale, while only a small scale is presented in the bottom figure.

The largest displacement in path 1 occurs in specimen 1. Subtracting the z -coordinate after welding from the coordinate before welding at $y = -450$ mm results in an upward displacement of 1.32mm.

The order of magnitude of the deformation is comparable to deformations of the rib-deck specimens used in the research of Sim et al. [1], where four trapezoidal stiffeners without crossbeams were investigated and measures were taken at five points in transverse direction. The measured displacements are shown in figure 17. In the research, specimen 1 was non-pre-cambered and is, therefore, the most comparable to results in this research. Upward displacements of the middle ribs are 2-3mm, compared to the initial geometry. Adding a crossbeam will reduce these values and the slope will be more shallow. The values can not directly be compared, due to the differences in geometry, welding procedure and material properties, but the order of magnitude is comparable.

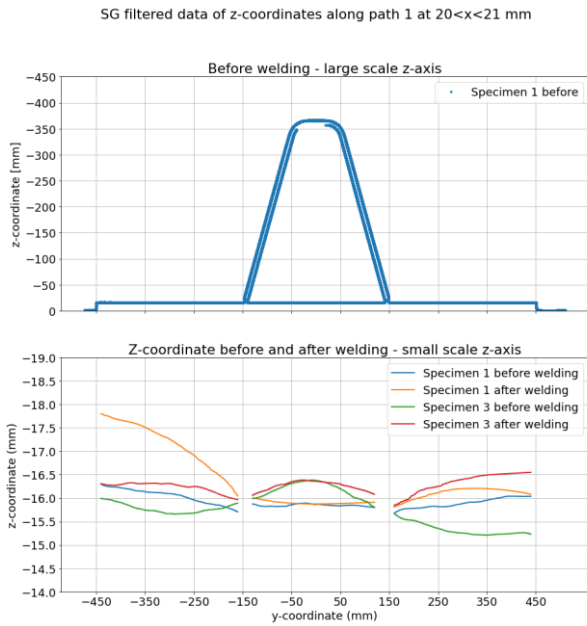


Figure 16. Z-coordinates of top of deck plate along path 1

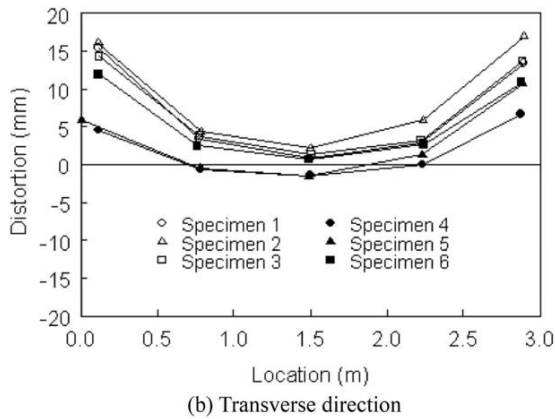


Figure 17. Transverse displacement rib-deck specimens by Sim et al. [1]

3.3 Discussion

The Artec Leo scanner can reach a 3D point accuracy of up to 0.1mm, according to the manufacturer [15]. Settings such as HD density will affect the accuracy. The exact accuracy with the current settings is unknown and needs to be studied in more detail. A scatter of z-coordinates along each path is found. The spread is approximately 0.25mm. The data has been filtered with the SG algorithm. The parameters of this algorithm will affect the accuracy. More advanced scanners need to be used to compare the scattering of the measurements and determine the

accuracy. Finally, inaccuracies may occur due to errors occurring during scanning, such as frame misalignments and surface reflections.

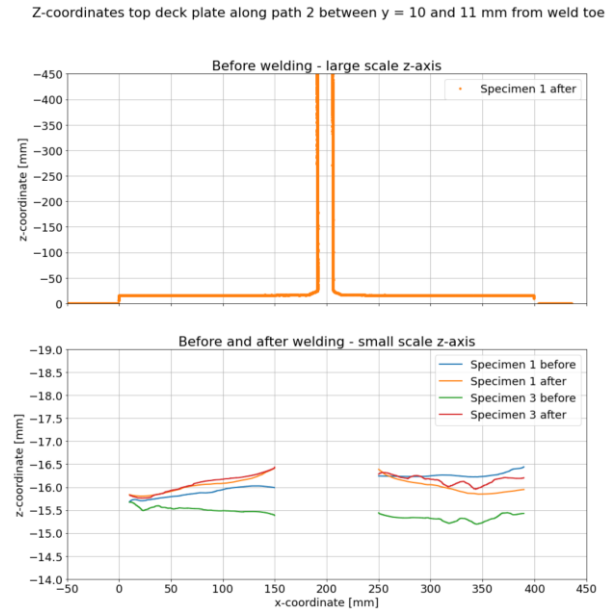


Figure 18. Z-coordinates of top of deck plate along path 2



Figure 19. Z-coordinates of top of deck plate along path 3

4 Conclusions

In this paper, experimental investigations of deformations and temperatures due to welding were performed on a segment of an OSD. These data are required to optimize welding processes,

limit distortions and improve the understanding of residual stress state in welded details derived from the deformation field. A new distortion measurement methodology has been established with the use of an advanced handheld 3D scanner. The following conclusions can be drawn from the research.

1. A maximum temperature of 1042 °C 1.8s after welding was recorded.
2. The temperature behind the heat source reduces to 200 °C at a distance of 150mm from the heat source. In front and perpendicular to the heat source, the temperature decreases to room temperature at a distance of 50 and 150mm, respectively.
3. The maximum measured upward displacement of the 900x400 deck plate was 1.32 mm.
4. The order of magnitude of the deformation is comparable to research by Sim et al. [1]. However, no crossbeam was used in that research. In addition a different welding procedure and material properties were used, so no strict comparison is justified.
5. The maximum scatter along a path in vertical coordinates was approximately 0.25mm.
6. The established methodology with the 3D scanner is an easy to use and accurate tool for measuring displacements, but scanning must be done carefully to prevent misalignment of frames.

In future work, the obtained data can be compared to data obtained from more accurate scanners, such as the Artec spider, or from laser- or 3D photography tracking equipment. The obtained data will be used to improve numerical prediction models for simulation of the fatigue life time. The accuracy of the chosen boundary conditions in simulating a bridge deck should be investigated by measuring distortions in a full scale bridge deck. This could help in reducing the size of numerical models.

5 References

- [1] Sim HB, Uang CM, Sikorsky C. Effects of Fabrication Procedures on Fatigue Resistance of Welded Joints in Steel Orthotropic Decks. *Journal of Bridge Engineering*. 2009 Sep;**14**(5):366-73.
- [2] Deng D, Murakawa H, Liang W. Numerical simulation of welding distortion in large structures. *Computer Methods in Applied Mechanics and Engineering*. 2007;**196**(45):4613-27.
- [3] Ji B, Liu R, Chen C, Maeno H, Chen X. Evaluation on root-deck fatigue of orthotropic steel bridge deck. *Journal of Constructional Steel Research*. 2013 Nov;**90**:174-83.
- [4] de Jong FBP. Overview Fatigue Phenomenon in Orthotropic Bridge Decks in the Netherlands. Sacramento, CA; 2004.
- [5] Xin H, Veljkovic M. Effects of residual stresses on fatigue crack initiation of butt-welded plates made of high strength steel; 2019.
- [6] Maddox SJ. *Fatigue strength of welded structures*. Cambridge, England: Abington Pub; 1991.
- [7] Puymbroeck EV, Staen GV, Iqbal N, Backer HD. Residual weld stresses in stiffener-to-deck plate weld of an orthotropic steel deck. *Journal of Constructional Steel Research*. 2019 Aug;**159**:534-47.
- [8] Webster GA, Ezeilo AN. Residual stress distributions and their influence on fatigue lifetimes. *International Journal of Fatigue*. 2001;**23**:375-83.
- [9] van Puymbroeck E, Nagy W, De Backer H. Use of the hole drilling method to determine residual weld stresses in bridge constructions; 2016. p. 1-6
- [10] Gu Y, Li Y, Zhou Z, Ren S, Kong C. Numerical Simulation and Measurement of Welding Residual Stresses in Orthotropic Steel Decks Stiffened with U-Shaped Ribs. *International Journal of Steel Structures*. 2020 Mar;**20**(3):856-69.
- [11] Goldak J, Chakravarti A, Bibby M. A new finite element model for welding heat

- sources. *Metallurgical Transactions B*. 1984 Jun;**15**(2):299-305.
- [12]Manai A, von Bock und Polach RUF, Al-Emrani M. A probabilistic study of welding residual stresses distribution and their contribution to the fatigue life. *Engineering Failure Analysis*. 2020 Dec;**118**:104787.
- [13]Karlsson A, Wesley C. Fatigue Analysis for Orthotropic Steel Deck Bridges. Göteborg, Sweden: Chalmers University of Technology; 2015.
- [14]Advanced Thermal Imaging Camera FLIR E96;. Accessed: 2022-03-13. <https://www.flir.com/products/e96/>
- [15]Artec-group. Artec Studio 16 User Guide;.

6 Appendix

The data points before filtering of path 1, 2 and 3 are shown in figure 21,22 and 23, respectively.

Data points along path 1 between $20 < x < 21$ mm

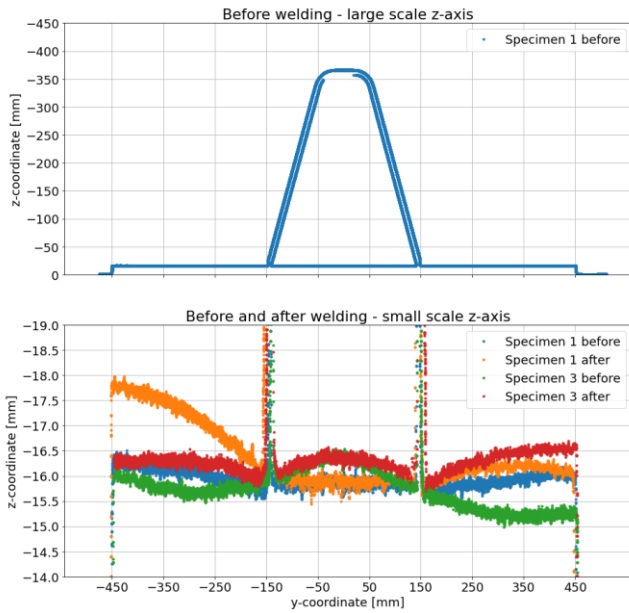


Figure 20. Raw data points along path 1

z-coordinates top deck plate along path 2 between $y = 10$ and 11 mm from weld toe

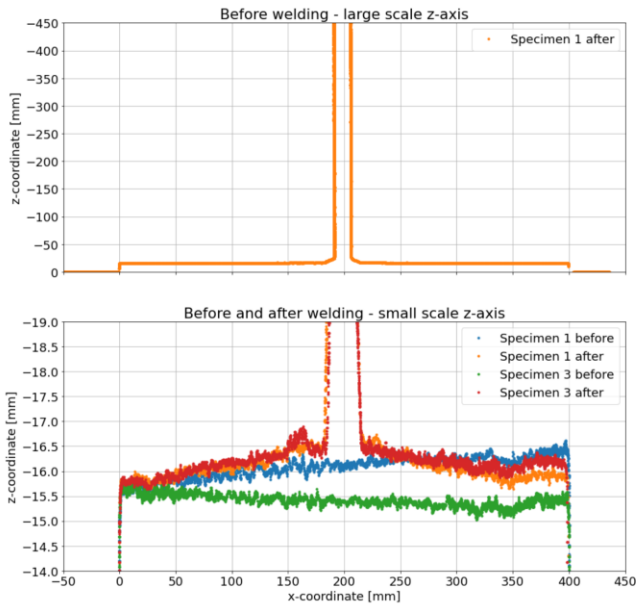


Figure 21. Raw data points along path 2

z-coordinates top deck plate along path 3 between $y = 10$ and 11 mm from weld toe

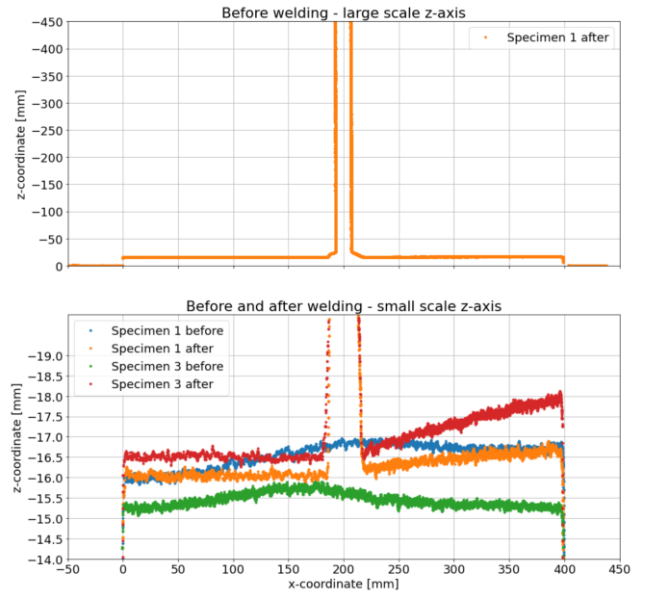
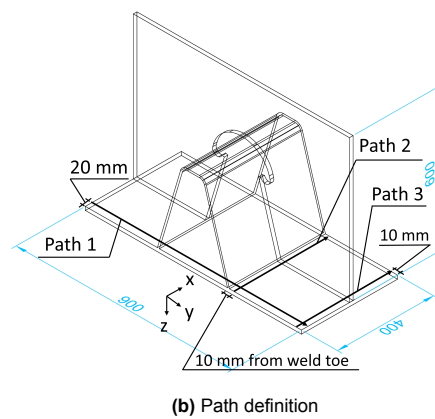
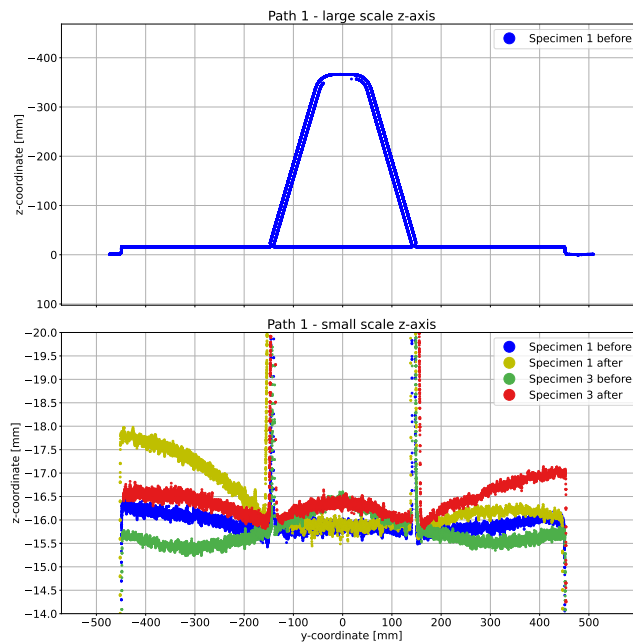


Figure 22. Raw data points along path 3

B

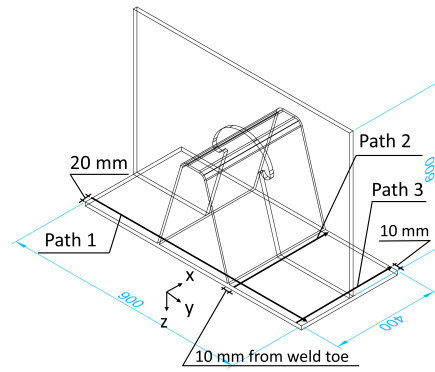
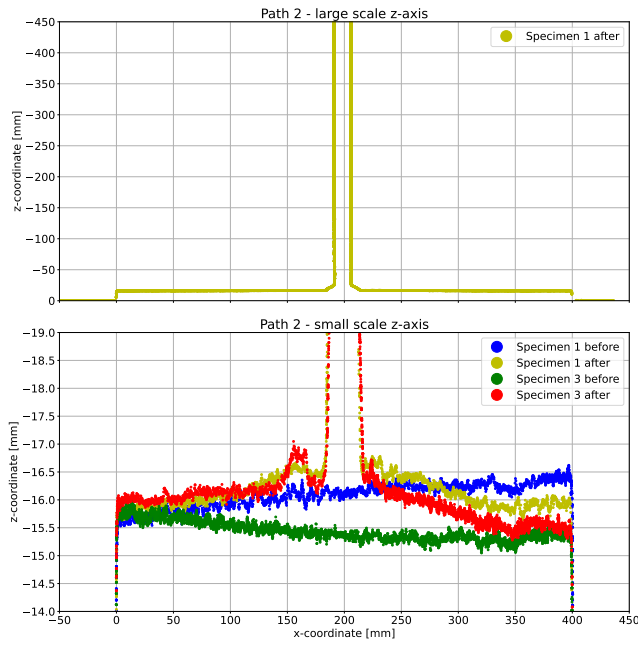
Raw data geometry Artec scanner

In this appendix, the raw data points obtained from the geometry scans are shown. The data points represent the z-coordinates of the polygonal nodes from the .stl file along Path 1, 2 and 3. The points were extracted by the NumPy-stl package. The raw data has been filtered in the main report.



(a) z-coordinates relative to work bench along path 1 in specimen 1 & 3

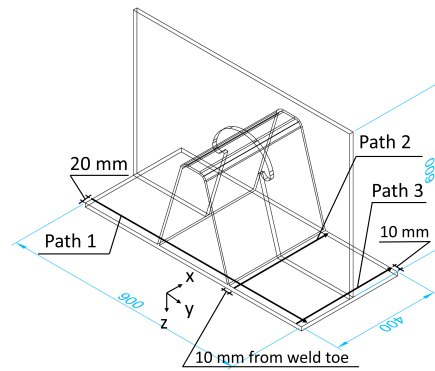
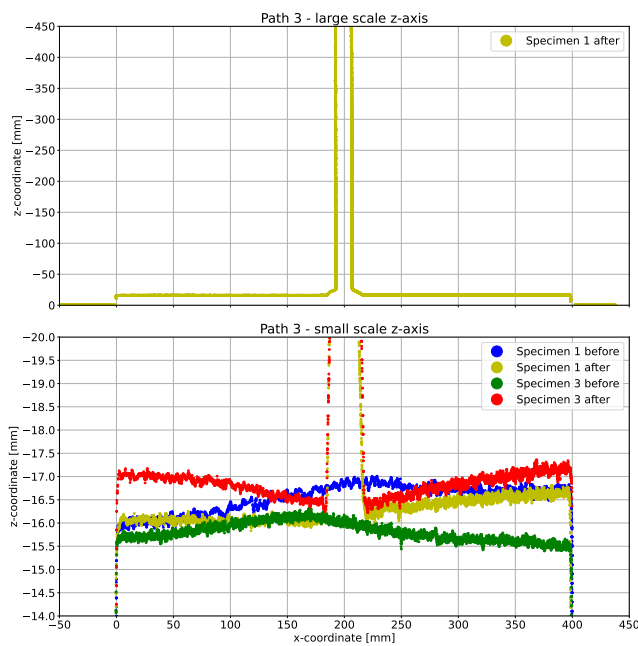
Figure B.1: z-coordinates of top of deck plate before and after welding along path 1 in specimen 1 & 3



(b) Path definition

(a) z-coordinates relative to work bench along path 2 in specimen 1 & 3

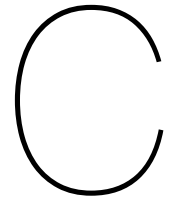
Figure B.2: z-coordinates of top of deck plate before and after welding along path 2 in specimen 1 & 3



(b) Path definition

(a) z-coordinates relative to work bench along path 3 in specimen 1 & 3

Figure B.3: z-coordinates of top of deck plate before and after welding along path 3 in specimen 1 & 3



Python script thermal model

In this appendix, the script for creating the steps and for deactivating and reactivating the weld increments in the thermal model is given. The script can be run in Abaqus.

```
1
2 # Save by amaarleveld on 2021_09_06-13.35.02; build 2019 2018_09_24-20.41.51 157541
3 from part import *
4 from material import *
5 from section import *
6 from assembly import *
7 from step import *
8 from interaction import *
9 from load import *
10 from mesh import *
11 from optimization import *
12 from job import *
13 from sketch import *
14 from visualization import *
15 from connectorBehavior import *
16 import numpy as np
17
18 Tol = 0.1
19
20 #Specimen 1
21
22 T_prestep = 1e-5 #s
23 T_pass11 = 45.0
24 T_cooling11 = 134.0
25 T_pass12 = 70.0
26 T_cooling12 = 360.0
27 T_pass21 = 46.0
28 T_cooling21 = 159.0
29 T_pass22 = 75.0
30 T_cooling22 = 4000.0
31 T_prestep_CB = 1e-5
32 T_tackweld1 = 3.0
33 T_coolingtw1 = 20.0
34 T_tackweld2 = 3.0
35 T_coolingtw2 = 20.0
36 T_pass3 = 89.0
37 T_cooling3 = 176.0
38 T_pass4 = 73.0
39 T_cooling4 = 727.0
40 T_pass5 = 81.0
41 T_cooling5 = 157.0
42 T_pass6 = 80.0
43 T_cooling6 = 1320.0
44 T_pass7 = 62.0
45 T_cooling7 = 142.0
46 T_pass8 = 58.0
```

```

47 T_cooling8 = 236.0
48 T_pass9 = 58.0
49 T_cooling9 = 76.0
50 T_pass10 = 59.0
51 T_cooling10 = 4000.0
52
53 n_steps11 = 20
54 n_steps12 = 20
55 n_steps21 = 20
56 n_steps22 = 20
57 n_steps3 = 15
58 n_steps4 = 15
59 n_steps5 = 15
60 n_steps6 = 15
61 n_steps7 = 15
62 n_steps8 = 15
63 n_steps9 = 15
64 n_steps10 = 15
65
66 #Create steps
67
68 a = [11,12,21,22,3,4,5,6,7,8,9,10]
69 b = ['Initial', 'Pre-Step']
70 c = [T_pass11,T_pass12,T_pass21,T_pass22,T_pass3,T_pass4,T_pass5,T_pass6,T_pass7,T_pass8,
71      T_pass9,T_pass10]
72 d = [T_cooling11,T_cooling12,T_cooling21,T_cooling22,T_cooling3,T_cooling4,T_cooling5,
73      T_cooling6,T_cooling7,T_cooling8,T_cooling9,T_cooling10]
74 n_steps = [n_steps11,n_steps12,n_steps21,n_steps22,n_steps3,n_steps4,n_steps5,n_steps6,
75            n_steps7,n_steps8,n_steps9,n_steps10]
76
77 for i in range(0,len(a)):
78     for j in range(1,n_steps[i]+1):
79         b.append('Pass' + str(a[i]) + '-' + str(j))
80         b.append('Cooling-' + str(a[i]))
81
82 time = [T_prestep]
83 for i in range (len(c)):
84     for j in range(n_steps[i]):
85         time.append(c[i]/n_steps[i])
86         time.append(d[i])
87
88 for i in range(1,len(b)):
89     if time[i-1] < 1:
90         mdb.models['Crossbeam-Thermal5'].HeatTransferStep(name=b[i], previous=b[i-1],
91         timePeriod=time[i-1], deltmx=300, initialInc=1e-6, maxInc=time[i-1]/10.0, maxNumInc
92         =1000000, minInc=1e-11)
93     else:
94         mdb.models['Crossbeam-Thermal5'].HeatTransferStep(name=b[i], previous=b[i-1],
95         timePeriod=time[i-1], deltmx=300, initialInc=1e-2, maxInc=time[i-1]/10.0, maxNumInc
96         =1000000, minInc=1e-11)
97
98 #Create re-activation step crossbeam
99 mdb.models['Crossbeam-Thermal5'].HeatTransferStep(name='Pre-Step-CB', previous='Cooling-22',
100 timePeriod=T_prestep_CB, deltmx=300, initialInc=1e-6, maxInc=T_prestep_CB/10.0, maxNumInc
101 =1000000, minInc=1e-11)
102
103 #Create heating step tack weld 1,2 + cooling_tw1,2
104
105 mdb.models['Crossbeam-Thermal5'].HeatTransferStep(name='TackWeld'+str(1), previous='Pre-Step-
106 CB',
107 timePeriod=T_tackweld1, deltmx=300, initialInc=1e-2, maxInc=T_tackweld1/10.0, maxNumInc
108 =1000000, minInc=1e-11)
109
110 mdb.models['Crossbeam-Thermal5'].HeatTransferStep(name='Cooling_tw'+str(1), previous='
111 TackWeld'+str(1),
112 timePeriod=T_coolingt看1, deltmx=300, initialInc=1e-2, maxInc=T_coolingt看1/10.0, maxNumInc
113 =1000000, minInc=1e-11)
114
115 mdb.models['Crossbeam-Thermal5'].HeatTransferStep(name='TackWeld'+str(2), previous='
116 Cooling_tw'+str(1),

```

```

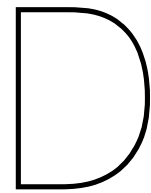
106     timePeriod=T_tackweld2, deltmx=300, initialInc=1e-2, maxInc=T_tackweld2/10.0, maxNumInc
107         =1000000, minInc=1e-11)
108 mdb.models['Crossbeam-Thermal5'].HeatTransferStep(name='Cooling_tw'+str(2), previous='
109     TackWeld'+str(2),
110     timePeriod=T_coolingtw2, deltmx=300, initialInc=1e-2, maxInc=T_coolingtw2/10.0, maxNumInc
111         =1000000, minInc=1e-11)
112 #De-activate all passes and crossbeam elements
113 e = mdb.models['Crossbeam-Thermal5'].rootAssembly
114 region= e.sets['Deactivate']
115 mdb.models['Crossbeam-Thermal5'].ModelChange(name='Pre-Step', createStepName='Pre-Step',
116     region=region, activeInStep=False,
117     includeStrain=False)
118 #Re-activate CB including tack welds
119 region =e.sets['ReactivateCB']
120 mdb.models['Crossbeam-Thermal5'].ModelChange(name='ReactivateCB', createStepName='Pre-Step-CB
121     ',
122     region=region, activeInStep=True, includeStrain=False)
123 Tol = 0.1
124 X0 = [50,0,50,0,188.75,211.25,192.5,207.5,192.5,207.5,188.75,211.25]
125 Y0 = [6.84,9.09,-290.17,-292.42,6.18,6.18,-289.51,-289.51,308.336,308.336,-591.66,-591.66]
126 Z0 = [-3.68,-3.68,-3.68,-3.68,-7.36,-7.36,-7.36,-7.36,-3.75,-3.75,-3.75,-3.75]
127
128 Weld_Inc = [300/n_steps[0],400/n_steps[1],300/n_steps[2],400/n_steps
129     [3],19.37,19.37,19.37,19.37,20.144,20.144,20.144,20.144]
130 #Rotation bounding box around z-axis
131 alpha = [0,0,0,0,-np.pi/2,-np.pi/2,np.pi/2,np.pi/2,-np.pi/2,-np.pi/2,np.pi/2,np.pi/2]
132
133 #Rotation bounding box around x-axis
134 beta = [0,0,0,0,np.arctan(350/102.5),np.arctan(350/102.5),-np.arctan(350/102.5),-np.arctan
135     (350/102.5),0,0,0,0]
136 for i in range(12):
137     e1 = e.sets['Pass' + str(a[i])].elements
138     for j in range(1,n_steps[i]+1):
139         WeldInc = Weld_Inc[i]
140         #Points boundingcylinder before rotation and translation
141
142         #x1,y1,z1 is center of first end of getbyboundingcylinder, x2,y2,z2 center of second end.
143         #Distance between the points is weld increment
144
145         y1 = 0
146         z1 = 0
147         y2 = 0
148         z2 = 0
149
150         # Last step is larger than 20mm for pass 7-10
151         if 8<=i<=11:
152             if j==n_steps[i]:
153                 x1 = -Tol+(j-1)*WeldInc
154                 x2 = Tol + WeldInc*j + 5
155             else:
156                 x1 = -Tol+(j-1)*WeldInc
157                 x2 = Tol + WeldInc*j
158
159         else:
160             x1 = -Tol+(j-1)*WeldInc
161             x2 = Tol + WeldInc*j
162
163         #Transform points 1,2 to 3,4
164         #Rotate first around z, then around x, then translate
165         x3 = np.cos(alpha[i])*x1 - np.sin(alpha[i])*y1 + X0[i]
166         y3 = np.cos(beta[i])*np.sin(alpha[i])*x1 + np.cos(beta[i])*np.cos(alpha[i])*y1 - np.sin(
167             beta[i])*z1 + Y0[i]
168         z3 = np.sin(beta[i])*np.sin(alpha[i])*x1 + np.sin(beta[i])*np.cos(alpha[i])*y1 + np.cos(
169             beta[i])*z1 + Z0[i]

```

```

168 x4 = np.cos(alpha[i])*x2 - np.sin(alpha[i])*y2 + X0[i]
169 y4 = np.cos(beta[i])*np.sin(alpha[i])*x2 + np.cos(beta[i])*np.cos(alpha[i])*y2 - np.sin(
beta[i])*z2 + Y0[i]
170 z4 = np.sin(beta[i])*np.sin(alpha[i])*x2 + np.sin(beta[i])*np.cos(alpha[i])*y2 + np.cos(
beta[i])*z2 + Z0[i]
171
172 elements1 = e1.getByBoundingCylinder((x3, y3, z3), (x4, y4, z4),100)
173
174 #Create set from elements
175 e.Set(elements=elements1, name='Pass' + str(a[i]) + '-' + str(j))
176
177 #Don't reactivate tack welds
178 if i==8 or i==10:
179     if j==8 or j==9:
180         continue
181
182 if i==9 or i==11:
183     if j==1 or j==2:
184         continue
185
186 #Re-activate set
187 region = e.sets['Pass' +str(a[i]) + '-' + str(j)]
188 mdb.models['Crossbeam-Thermal5'].ModelChange(name='Pass' +str(a[i]) + '-' + str(j),
createStepName='Pass' +str(a[i]) + '-' + str(j),
189     region=region, activeInStep=True, includeStrain=False)
190 #region = Region(elements=elements1)
191 #mdb.models['Crossbeam-Thermal5'].ModelChange(name='Pass' +str(a[i]) + '-' + str(j),
createStepName='Pass' +str(a[i]) + '-' + str(j),
192     # region=region, activeInStep=True, includeStrain=False)
193
194 #Convection
195 mdb.models['Crossbeam-Thermal5'].FilmCondition(createStepName='Pre-Step', definition=
EMBEDDED_COEFF, filmCoeff=0.015, filmCoeffAmplitude='', name='Convection',
196     sinkAmplitude='', sinkDistributionType=UNIFORM, sinkFieldName='',
197     sinkTemperature=6.0, surface=
198     mdb.models['Crossbeam-Thermal5'].rootAssembly-surfaces['FullSurface'])
199
200
201 #Radiation
202 mdb.models['Crossbeam-Thermal5'].RadiationToAmbient(name='RadiationToAmbient', createStepName
='Pre-Step', surface=e.sets['FullSurface'],
203     emissivity=0.5, ambientTemperature=6)
204
205 #Load
206 mdb.models['Crossbeam-Thermal5'].BodyHeatFlux(name='Load-'+str(1), createStepName='Pre-Step',
region=e.sets['FullModel'],
207     magnitude=1, distributionType=USER_DEFINED)

```



Python script mechanical model

In this appendix, the script for the mechanical model is given. The major differences are the step type, the definition of the temperature field resulting from the thermal analysis and the specification of mechanical boundary conditions.

```
1
2 Crossbeam-Mech5.py
3 Eerder deze maand
4 2 Apr.
5
6 Je hebt een item geüpload
7 Tekst
8 Crossbeam-Mech5.py
9 # Save by amaarleveld on 2021_09_06-13.35.02; build 2019 2018_09_24-20.41.51 157541
10 from part import *
11 from material import *
12 from section import *
13 from assembly import *
14 from step import *
15 from interaction import *
16 from load import *
17 from mesh import *
18 from optimization import *
19 from job import *
20 from sketch import *
21 from visualization import *
22 from connectorBehavior import *
23 import numpy as np
24
25 Tol = 0.1
26
27 #Specimen 1
28
29 T_prestep = 1e-5 #s
30 T_pass11 = 45.0
31 T_cooling11 = 134.0
32 T_pass12 = 70.0
33 T_cooling12 = 360.0
34 T_pass21 = 46.0
35 T_cooling21 = 159.0
36 T_pass22 = 75.0
37 T_cooling22 = 4000.0
38 T_prestep_CB = 1e-5
39 T_tackweld1 = 3.0
40 T_coolingtw1 = 20.0
41 T_tackweld2 = 3.0
42 T_coolingtw2 = 20.0
43 T_pass3 = 89.0
44 T_cooling3 = 176.0
45 T_pass4 = 73.0
```

```

46 T_cooling4 = 727.0
47 T_pass5 = 81.0
48 T_cooling5 = 157.0
49 T_pass6 = 80.0
50 T_cooling6 = 1320.0
51 T_pass7 = 62.0
52 T_cooling7 = 142.0
53 T_pass8 = 58.0
54 T_cooling8 = 236.0
55 T_pass9 = 58.0
56 T_cooling9 = 76.0
57 T_pass10 = 59.0
58 T_cooling10 = 4000.0
59
60 n_steps11 = 20
61 n_steps12 = 20
62 n_steps21 = 20
63 n_steps22 = 20
64 n_steps3 = 15
65 n_steps4 = 15
66 n_steps5 = 15
67 n_steps6 = 15
68 n_steps7 = 15
69 n_steps8 = 15
70 n_steps9 = 15
71 n_steps10 = 15
72
73 #Create steps
74
75 a = [11,12,21,22,3,4,5,6,7,8,9,10]
76 b = ['Initial','Pre-Step']
77 c = [T_pass11,T_pass12,T_pass21,T_pass22,T_pass3,T_pass4,T_pass5,T_pass6,T_pass7,T_pass8,
78      T_pass9,T_pass10]
79 d = [T_cooling11,T_cooling12,T_cooling21,T_cooling22,T_cooling3,T_cooling4,T_cooling5,
80      T_cooling6,T_cooling7,T_cooling8,T_cooling9,T_cooling10]
81 n_steps = [n_steps11,n_steps12,n_steps21,n_steps22,n_steps3,n_steps4,n_steps5,n_steps6,
82            n_steps7,n_steps8,n_steps9,n_steps10]
83
84 for i in range(0,len(a)):
85     for j in range(1,n_steps[i]+1):
86         b.append('Pass' + str(a[i]) + '-' + str(j))
87     b.append('Cooling-' + str(a[i]))
88
89 time = [T_prestep]
90 for i in range (len(c)):
91     for j in range(n_steps[i]):
92         time.append(c[i]/n_steps[i])
93     time.append(d[i])
94
95 for i in range(1,len(b)):
96     if time[i-1] < 1:
97         mdb.models['Crossbeam-Mechanical5'].StaticStep(name=b[i], previous=b[i-1],
98             timePeriod=time[i-1], initialInc=1e-6, maxInc=time[i-1]/10.0, maxNumInc=1000000, minInc
99             =1e-11)
100     else:
101         mdb.models['Crossbeam-Mechanical5'].StaticStep(name=b[i], previous=b[i-1],
102             timePeriod=time[i-1], initialInc=1e-2, maxInc=time[i-1]/10.0, maxNumInc=1000000, minInc
103             =1e-11)
104
105 #Create re-activation step crossbeam
106 mdb.models['Crossbeam-Mechanical5'].StaticStep(name='Pre-Step-CB', previous='Cooling-22',
107     timePeriod=T_prestep_CB, initialInc=1e-6, maxInc=T_prestep_CB/10.0, maxNumInc=1000000,
108     minInc=1e-11)
109
110 #Create static step tack weld 1,2 + cooling_tw1,2
111
112 mdb.models['Crossbeam-Mechanical5'].StaticStep(name='TackWeld'+str(1), previous='Pre-Step-CB'
113     ,
114     timePeriod=T_tackweld1, initialInc=1e-2, maxInc=T_tackweld1/10.0, maxNumInc=1000000, minInc
115     =1e-11)

```



```

109 mdb.models['Crossbeam-Mechanical5'].StaticStep(name='Cooling_tw'+str(1), previous='TackWeld'+
110 str(1),
111 timePeriod=T_coolingtw1, initialInc=1e-2, maxInc=T_coolingtw1/10.0, maxNumInc=1000000,
112 minInc=1e-11)
113 mdb.models['Crossbeam-Mechanical5'].StaticStep(name='TackWeld'+str(2), previous='Cooling_tw'+
114 str(1),
115 timePeriod=T_tackweld2, initialInc=1e-2, maxInc=T_tackweld2/10.0, maxNumInc=1000000, minInc
116 =1e-11)
117 mdb.models['Crossbeam-Mechanical5'].StaticStep(name='Cooling_tw'+str(2), previous='TackWeld'+
118 str(2),
119 timePeriod=T_coolingtw2, initialInc=1e-2, maxInc=T_coolingtw2/10.0, maxNumInc=1000000,
120 minInc=1e-11)
121 #De-activate all passes and crossbeam elements
122 e = mdb.models['Crossbeam-Mechanical5'].rootAssembly
123 region= e.sets['Deactivate']
124 mdb.models['Crossbeam-Mechanical5'].ModelChange(name='Pre-Step', createStepName='Pre-Step',
125 region=region, activeInStep=False,
126 includeStrain=False)
127 #Re-activate CB including tack welds
128 region =e.sets['ReactivateCB']
129 mdb.models['Crossbeam-Mechanical5'].ModelChange(name='ReactivateCB', createStepName='Pre-Step
130 -CB',
131 region=region, activeInStep=True, includeStrain=False)
132 Tol = 0.1
133 X0 = [50,0,50,0,188.75,211.25,192.5,207.5,192.5,207.5,188.75,211.25]
134 Y0 = [6.84,9.09,-290.17,-292.42,6.18,6.18,-289.51,-289.51,308.336,308.336,-591.66,-591.66]
135 Z0 = [-3.68,-3.68,-3.68,-3.68,-7.36,-7.36,-7.36,-7.36,-3.75,-3.75,-3.75,-3.75]
136 Weld_Inc = [300/n_steps[0],400/n_steps[1],300/n_steps[2],400/n_steps
137 [3],19.37,19.37,19.37,19.37,20.144,20.144,20.144,20.144]
138 #Rotation bounding box around z-axis
139 alpha = [0,0,0,0,-np.pi/2,-np.pi/2,np.pi/2,np.pi/2,-np.pi/2,-np.pi/2,np.pi/2,np.pi/2]
140 #Rotation bounding box around x-axis
141 beta = [0,0,0,0,np.arctan(350/102.5),np.arctan(350/102.5),-np.arctan(350/102.5),-np.arctan
142 (350/102.5),0,0,0,0]
143 for i in range(12):
144     e1 = e.sets['Pass' + str(a[i])].elements
145     for j in range(1,n_steps[i]+1):
146         WeldInc = Weld_Inc[i]
147         #Points boundingcylinder before rotation and translation
148
149         #x1,y1,z1 is center of first end of getbyboundingcylinder, x2,y2,z2 center of second end.
150         #Distance between the points is weld increment
151
152         y1 = 0
153         z1 = 0
154         y2 = 0
155         z2 = 0
156
157         # if 4<=i<=7:
158         # if j==1:
159             # x1 = -25
160             # x2 = Tol
161         # else:
162             # x1 = -Tol+(j-2)*WeldInc
163             # x2 = Tol + WeldInc*(j-1)
164
165         # Last step is larger than 20mm for pass 7-10
166         if 8<=i<=11:
167             if j==n_steps[i]:
168                 x1 = -Tol+(j-1)*WeldInc
169                 x2 = Tol + WeldInc*j + 5

```

```

170     else:
171         x1 = -Tol+(j-1)*WeldInc
172         x2 = Tol + WeldInc*j
173
174     else:
175         x1 = -Tol+(j-1)*WeldInc
176         x2 = Tol + WeldInc*j
177
178     #Transform points 1,2 to 3,4
179     #Rotate first around z, then around x, then translate
180     x3 = np.cos(alpha[i])*x1 - np.sin(alpha[i])*y1 + X0[i]
181     y3 = np.cos(beta[i])*np.sin(alpha[i])*x1 + np.cos(beta[i])*np.cos(alpha[i])*y1 - np.sin(beta[i])*z1 + Y0[i]
182     z3 = np.sin(beta[i])*np.sin(alpha[i])*x1 + np.sin(beta[i])*np.cos(alpha[i])*y1 + np.cos(beta[i])*z1 + Z0[i]
183     x4 = np.cos(alpha[i])*x2 - np.sin(alpha[i])*y2 + X0[i]
184     y4 = np.cos(beta[i])*np.sin(alpha[i])*x2 + np.cos(beta[i])*np.cos(alpha[i])*y2 - np.sin(beta[i])*z2 + Y0[i]
185     z4 = np.sin(beta[i])*np.sin(alpha[i])*x2 + np.sin(beta[i])*np.cos(alpha[i])*y2 + np.cos(beta[i])*z2 + Z0[i]
186
187     elements1 = e1.getByBoundingCylinder((x3, y3, z3), (x4, y4, z4),100)
188
189     #Create set from elements
190     e.Set(elements=elements1, name='Pass' + str(a[i]) + '-' + str(j))
191
192     #Don't reactivate tack welds
193     if i==8 or i==10:
194         if j==8 or j==9:
195             continue
196
197     if i==9 or i==11:
198         if j==1 or j==2:
199             continue
200
201     #Re-activate set
202     region =e.sets['Pass' +str(a[i]) + '-' + str(j)]
203     mdb.models['Crossbeam-Mechanical5'].ModelChange(name='Pass' +str(a[i]) + '-' + str(j),
204     createStepName='Pass' +str(a[i]) + '-' + str(j),
205     region=region, activeInStep=True, includeStrain=False)
206     # region = Region(elements=elements1)
207     # mdb.models['Crossbeam-Mechanical5'].ModelChange(name='Pass' +str(a[i]) + '-' + str(j),
208     createStepName='Pass' +str(a[i]) + '-' + str(j),
209     # region=region, activeInStep=True, includeStrain=False)
210
211 # #Convection
212 # mdb.models['Crossbeam-Mechanical5'].FilmCondition(createStepName='Pre-Step', definition=
213 # EMBEDDED_COEFF, filmCoeff=0.015, filmCoeffAmplitude='', name='Convection',
214 # sinkAmplitude='', sinkDistributionType=UNIFORM, sinkFieldName='',
215 # sinkTemperature=6.0, surface=
216 # mdb.models['Crossbeam-Mechanical5'].rootAssembly-surfaces['FullSurface'])
217
218 # #Radiation
219 # mdb.models['Crossbeam-Mechanical5'].RadiationToAmbient(name='RadiationToAmbient',
220 createStepName='Pre-Step', surface=e-surfaces['FullSurface'],
221 # emissivity=0.5, ambientTemperature=6)
222
223 # #Load
224 # mdb.models['Crossbeam-Mechanical5'].BodyHeatFlux(name='Load-'+str(1), createStepName='Pre-
225 Step', region=e.sets['FullModel'],
226 # magnitude=1, distributionType=USER_DEFINED)
227
228 #Create unclamping step
229 mdb.models['Crossbeam-Mechanical5'].StaticStep(name='Unclamping', previous='Cooling-'+str(10)
230 ,
231 timePeriod=1.0, initialInc=1e-2, maxInc=0.1, maxNumInc=1000000, minInc=1e-11)
232
233 #Create predefined temperature field from odb
234 mdb.models['Crossbeam-Mechanical5'].Temperature(absoluteExteriorTolerance=0.0,
235 beginIncrement=1, beginStep=1, createStepName='Pre-Step', distributionType=
236 FROM_FILE, endIncrement=None, endStep=1, exteriorTolerance=0.05, fileName=

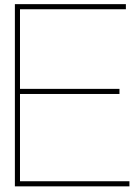
```

```

232     '/home/amaarleveld/crossbeamthermal5.odb'
233     , interpolate=MIDSIDE_ONLY, name='Predefined Field-2')
234
235 #Modify begin/end steps predefined field
236 count = 2 #Pass11-1 is step 2, so start at step 2
237 for i in range(4):
238     for j in range(1,n_steps[i]+1):
239         mdb.models['Crossbeam-Mechanical5'].predefinedFields['Predefined Field-2'].
240             setValuesInStep(
241                 beginStep=count,endStep=count, stepName='Pass' + str(a[i]) + '-' + str(j))
242                 count += 1
243         mdb.models['Crossbeam-Mechanical5'].predefinedFields['Predefined Field-2'].setValuesInStep(
244             beginStep=count,endStep=count, stepName='Cooling-' + str(a[i]))
245         #print('Cooling-' + str(a[i]), count+n_steps[i]+2,count+n_steps[i]+2)
246         count += 1
247
248 mdb.models['Crossbeam-Mechanical5'].predefinedFields['Predefined Field-2'].setValuesInStep(
249     beginStep=count,endStep=count, stepName='Pre-Step-CB')
250 count += 1
251
252 mdb.models['Crossbeam-Mechanical5'].predefinedFields['Predefined Field-2'].setValuesInStep(
253     beginStep=count,endStep=count, stepName='TackWeld'+str(1))
254 count += 1
255
256 mdb.models['Crossbeam-Mechanical5'].predefinedFields['Predefined Field-2'].setValuesInStep(
257     beginStep=count,endStep=count, stepName='Cooling_tw'+str(1))
258 count += 1
259
260 mdb.models['Crossbeam-Mechanical5'].predefinedFields['Predefined Field-2'].setValuesInStep(
261     beginStep=count,endStep=count, stepName='TackWeld' + str(2))
262 count += 1
263
264 mdb.models['Crossbeam-Mechanical5'].predefinedFields['Predefined Field-2'].setValuesInStep(
265     beginStep=count,endStep=count, stepName='Cooling_tw' + str(2))
266 count += 1
267
268 for i in range(4,12):
269     for j in range(1,n_steps[i]+1):
270         mdb.models['Crossbeam-Mechanical5'].predefinedFields['Predefined Field-2'].
271             setValuesInStep(
272                 beginStep=count,endStep=count, stepName='Pass' + str(a[i]) + '-' + str(j))
273                 count +=1
274         mdb.models['Crossbeam-Mechanical5'].predefinedFields['Predefined Field-2'].setValuesInStep(
275             beginStep=count,endStep=count, stepName='Cooling-' + str(a[i]))
276         count += 1
277
278 # count = 2 #Pass11-1 is step 2, so start at step 2
279 # for i in range(4):
280     # for j in range(1,n_steps[i]+1):
281         # print('Pass' + str(a[i]) + '-' + str(j),count,count)
282         # count +=1
283     # print('Cooling-' + str(a[i]), count,count)
284     # count += 1
285
286 # print('Pre-Step-CB', count,count)
287 # count += 1
288
289 # print('TackWeld'+str(1), count,count)
290 # count += 1
291
292 # print('Cooling_tw'+str(1), count,count)
293 # count += 1
294
295 # print('TackWeld'+str(2), count,count)
296 # count += 1
297
298 # print('Cooling_tw'+str(2), count,count)
299 # count += 1
300
301 # for i in range(4,12):
302     # for j in range(1,n_steps[i]+1):

```

```
301     # print('Pass' + str(a[i]) + '-' + str(j),count,count)
302     # count+=1
303     # print('Cooling-' + str(a[i]), count,count)
304     # count += 1
305
306 #Boundary conditions
307 mdb.models['Crossbeam-Mechanical5'].DisplacementBC(amplitude=UNSET, createStepName='Pre-Step'
308 , distributionType=UNIFORM, fieldName='', fixed=OFF, localCsys=None, name=
309 'BCDeckLine', region=mdb.models['Crossbeam-Mechanical5'].rootAssembly.sets['DeckLines'],
310 u1=
311 0.0, u2=0, u3=0, ur1=UNSET, ur2=UNSET, ur3=UNSET)
312
313 mdb.models['Crossbeam-Mechanical5'].boundaryConditions['BCDeckLine'].deactivate(
314 'Unclamping')
315
316 mdb.models['Crossbeam-Mechanical5'].DisplacementBC(amplitude=UNSET, createStepName='
317 Unclamping'
318 , distributionType=UNIFORM, fieldName='', fixed=OFF, localCsys=None, name=
319 'BCUnclampingXY', region=mdb.models['Crossbeam-Mechanical5'].rootAssembly.sets['BC2-XY-
320 Unclamping'], u1=
321 0.0, u2=0, u3=UNSET, ur1=UNSET, ur2=UNSET, ur3=UNSET)
322
323 mdb.models['Crossbeam-Mechanical5'].DisplacementBC(amplitude=UNSET, createStepName='
324 Unclamping'
325 , distributionType=UNIFORM, fieldName='', fixed=OFF, localCsys=None, name=
326 'BCUnclampingYZ', region=mdb.models['Crossbeam-Mechanical5'].rootAssembly.sets['BC1-YZ-
327 Unclamping'], u1=
328 UNSET, u2=0, u3=0, ur1=UNSET, ur2=UNSET, ur3=UNSET)
329
330 #Field output
331 # mdb.models['Crossbeam-Mechanical5'].fieldOutputRequests['F-Output-1'].setValues(
332 # variables=('S', 'PE', 'PEEQ', 'PEMAG', 'U', 'RF', 'CSTRESS',
333 # 'CDISP', 'NT', 'TEMP'))
```



Dflux subroutine

In this appendix, the script of the Dflux subroutine is given. In the script, the moving Goldak double ellipsoid heat source model (DEHSM) is defined. A loop is created to define welding parameters for each pass. Each pass also has different Goldak parameters.

```
1
2     SUBROUTINE DFLUX (FLUX , SOL , KSTEP , KINC , TIME , NOEL , NPT , COORDS ,
3     1  JLTYP , TEMP , PRESS , SNAME)
4 C
5     INCLUDE 'ABA_PARAM.INC'
6 C
7     DIMENSION FLUX (2) , TIME (2) , COORDS (3)
8     CHARACTER*80 SNAME
9
10
11     !user coding to define FLUX(1) and FLUX(2)
12     real , dimension (30) :: Time_list , Time_cum
13     real , dimension (14) :: j , L_pass , V_pass , U_voltage , I_current , a_goldak , b_goldak ,
14     alpha_rot , beta_rot , gamma_rot , X0_trans , Y0_trans , Z0_trans
15     real :: X , Y , Z , T , Q , V , a , b , cf , cr , ff , fr , alpha , beta , gamma , X0 , Y0 , Z0 , RX , RY , RZ , ETTA , PI , T_prestep ,
16     T_pass11 , T_cooling11 , T_pass12 , T_cooling12 , T_pass21 , T_cooling21 , T_pass22 , T_cooling22 ,
17     T_prestep_CB , T_tackweld1 , T_coolingtw1 , T_tackweld2 , T_coolingtw2 , T_pass3 , T_cooling3 , T_pass4
18     , T_cooling4 , T_pass5 , T_cooling5 , T_pass6 , T_cooling6 , T_pass7 , T_cooling7 , T_pass8 , T_cooling8 ,
19     T_pass9 , T_cooling9 , T_pass10 , T_cooling10
20
21     X=COORDS (1)
22     Y=COORDS (2)
23     Z=COORDS (3)
24     T=TIME (2)
25
26     T_prestep = 1e-5 !s
27     T_pass11 = 45.0
28     T_cooling11 = 134.0
29     T_pass12 = 70.0
30     T_cooling12 = 360.0
31     T_pass21 = 46.0
32     T_cooling21 = 159.0
33     T_pass22 = 75.0
34     T_cooling22 = 4000.0
35     T_prestep_CB = 1e-5
36     T_tackweld1 = 3.0
37     T_coolingtw1 = 20.0
38     T_tackweld2 = 3.0
39     T_coolingtw2 = 20.0
40     T_pass3 = 89.0
41     T_cooling3 = 176.0
42     T_pass4 = 73.0
43     T_cooling4 = 727.0
44     T_pass5 = 81.0
45     T_cooling5 = 157.0
```

```

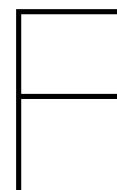
41 T_pass6 = 80.0
42 T_cooling6 = 1320.0
43 T_pass7 = 62.0
44 T_cooling7 = 142.0
45 T_pass8 = 58.0
46 T_cooling8 = 236.0
47 T_pass9 = 58.0
48 T_cooling9 = 76.0
49 T_pass10 = 59.0
50 T_cooling10 = 4000.0
51
52 Time_list = (/T_prestep,T_pass11,T_cooling11,T_pass12,T_cooling12,T_pass21,T_cooling21,
T_pass22,T_cooling22,T_prestep_CB,T_tackweld1,T_coolingtw1,T_tackweld2,T_coolingtw2,
T_pass3,T_cooling3,T_pass4,T_cooling4,T_pass5,T_cooling5,T_pass6,T_cooling6,T_pass7,
T_cooling7,T_pass8,T_cooling8,T_pass9,T_cooling9,T_pass10,T_cooling10/)
53 Time_cum(1) = T_prestep
54 do i = 2,30
55 Time_cum(i) = Time_cum(i-1) + Time_list(i)
56 end do
57
58 !index of passes in time_list
59 j = (/2,4,6,8,11,13,15,17,19,21,23,25,27,29/)
60
61 !Length of passes. Tack welds have no length to make v=0
62 L_pass = (/300.0,400.0,300.0,400.0,0.0,0.0,282.32,282.32,282.32,282.32,302.16,302.16,
302.16,302.16/)
63
64
65 do i = 1,14
66 V_pass(i) = L_pass(i)/Time_list(j(i))
67 end do
68
69 PI=3.141593
70
71 !(pass1.1,pass1.2,pass2.1,pass2.2,tw1,tw2,pass3,pass4,pass5,pass6,pass7,pass8,pass9,
pass10)
72 U_voltage = (/26.2,26.2,26.2,26.2,23.2,23.2,23.2,23.2,23.2,23.2,26.2,26.2,26.2,26.2/)
73 I_current = (/251,251,251,251,238,238,238,238,238,238,274,274,274,274/)
74 a_goldak = (/7.48/2,9.39/2,7.48/2,9.39/2,10.61/2,10.61/2,10.61/2,10.61/2,
75 10.61/2,10.61/2,10.61/2,10.61/2,10.61/2,10.61/2/)
76 b_goldak = (/7.38,3.53,7.38,3.53,5.3,5.3,5.3,5.3,5.3,5.3,5.3,5.3,5.3,5.3/)
77 alpha_rot = (/80*PI/180,52*PI/180,-80*PI/180,-52*PI/180,29*PI/180,-29*PI/180,-45*PI
/180,45*PI/180,45*PI/180,-45*PI/180,-45*PI/180,45*PI/180,45*PI/180,-45*PI/180/)
78 beta_rot = (/0.0,0.0,0.0,0.0,0.0,0.0,-PI/2.0,-PI/2.0,PI/2.0,PI/2.0,-PI/2.0,-PI/2.0,PI
/2.0,PI/2.0/)
79 gamma_rot = (/0.0,0.0,0.0,0.0,0.0,0.0,atan(350/102.5),atan(350/102.5),-atan(350/102.5),-
atan(350/102.5),0.0,0.0,0.0,0.0/)
80 X0_trans =
(/50.0,0.0,50.0,0.0,200.0,200.0,188.75,211.25,188.75,211.25,188.75,211.25,188.75,211.25/)
81 Y0_trans =
(/6.84,9.09,-290.17,-292.42,-70.83,-212.5,9.57,9.57,-292.9,-292.9,308.34,308.34,
82 -591.66,-591.66/)
83 Z0_trans = (/ -3.68,-3.68,-3.68,-3.68,-283.65,-283.65,-9.12,-9.12,-9.12,-9.12,-3.75,
84 -3.75,-3.75,-3.75/)
85
86 ETTA=0.85
87
88 FLUX(1) = 0
89 do i = 1,14 !14 passes including tack welds, change 14 to 4 for rib-deck model
90 if (T .GT. Time_cum(j(i)-1) .AND. T .LE. Time_cum(j(i))) then
91 Q = ETTA * U_voltage(i) * I_current(i) *10**3
92 V = V_pass(i)
93
94 !Goldak parameters
95 a = a_goldak(i)
96 b = b_goldak(i)
97 cf = a_goldak(i)
98 cr = 2.33*cf
99 ff = 0.6
100 fr = 1.4
101
102 Q=(Q*6*(3**0.5))/((a*b)*(PI**1.5))

```

```

103      !Translate x with V*T, rotate alpha around x, beta around z, gamma around x, then
104      translate with X0,Y0,Z0
105      alpha = alpha_rot(i)
106      beta = beta_rot(i)
107      gamma = gamma_rot(i)
108      X0 = X0_trans(i)
109      Y0 = Y0_trans(i)
110      Z0 = Z0_trans(i)
111
112      !Matrix multiplication and taking inverse
113      RX = ((y - Y0)*cos(gamma) + sin(gamma)*(z - Z0))*sin(beta) + cos(beta)*(x - X0) - V * (
T-Time_cum(j(i)-1))
114      RY = (cos(beta)*(y - Y0)*cos(gamma) + cos(beta)*(z - Z0)*sin(gamma) - sin(beta)*(x - X0
))*cos(alpha) + sin(alpha)*((z - Z0)*cos(gamma) - sin(gamma)*(y - Y0))
115      RZ = (-cos(beta)*(y - Y0)*cos(gamma) - cos(beta)*(z - Z0)*sin(gamma) + sin(beta)*(x -
X0))*sin(alpha) + cos(alpha)*((z - Z0)*cos(gamma) - sin(gamma)*(y - Y0))
116
117
118      !Goldak flux equations
119      IF (RX<=0) THEN !rear
120          IF((((RX)**2)/(cr**2)+((RY)**2)/(a**2)+((RZ)**2)/(b**2))<1) THEN
121              FLUX(1)=Q*(fr/cr)*EXP(-3*(((RX)**2)/(cr**2)+((RY)**2)/(a**2)+((RZ)**2)/(b**2)))
122          END IF
123
124      ELSEIF (RX>0) THEN !front
125          IF((((RX)**2)/(cf**2)+((RY)**2)/(a**2)+((RZ)**2)/(b**2))<1) THEN
126              FLUX(1)=Q*(ff/cf)*EXP(-3*(((RX)**2)/(cf**2)+((RY)**2)/(a**2)+((RZ)**2)/(b**2)))
127          END IF
128      END IF
129  end if
130  end do
131
132  FLUX(2)=0.0
133
134  RETURN
135  END

```

Documentation of experiment

In this appendix, the documentation of the welding experiment is given. The duration, voltage, current, wire feeding speed and wire type are given for each pass. The passes are defined in Figure F.1. More refined details of the tack weld geometry are also given.

F.1. Welding parameters

Table F.1: Documentation specimen 1

Action	Duration [mm:ss]	Voltage [V]	Current [A]	Wire feeding speed [mm/min]	Wire type	Recorded temp range [°C]
Pass 1.1	00:45	26.2	251	9.5	MC715H	0-650
Cooling 1.1	02:14					
Pass 1.2	01:10	26.2	251	9.5	MC715H	0-650
Cooling 1.2	06:00					
Pass 2.1	00:46	26.2	251	9.5	MC715H	0-650
Cooling 2.1	02:39					
Pass 2.2	01:15	26.2	251	9.5	MC715H	0-650
Cooling 2.2	25 days					
Pass 3	01:29	23.2	238	8.5	52RC	300-1500
Cooling 3	02:56					
Pass 4	01:13	23.2	238	8.5	52RC	300-1500
Cooling 4	12:07					
Pass 5	01:21	23.2	238	8.5	52RC	300-1500
Cooling 5	02:37					
Pass 6	01:20	23.2	238	8.5	52RC	0-650
Cooling 6	22:00					
Pass 7	01:02	26.2	274	10.5	MC715H	300-1500
Cooling 7	02:22					
Pass 8	00:58	26.2	274	10.5	MC715H	300-1500
Cooling 8	03:56					
Pass 9	00:58	26.2	274	10.5	MC715H	300-1500
Cooling 9	01:16					
Pass 10	00:59	26.2	274	10.5	MC715H	300-1500

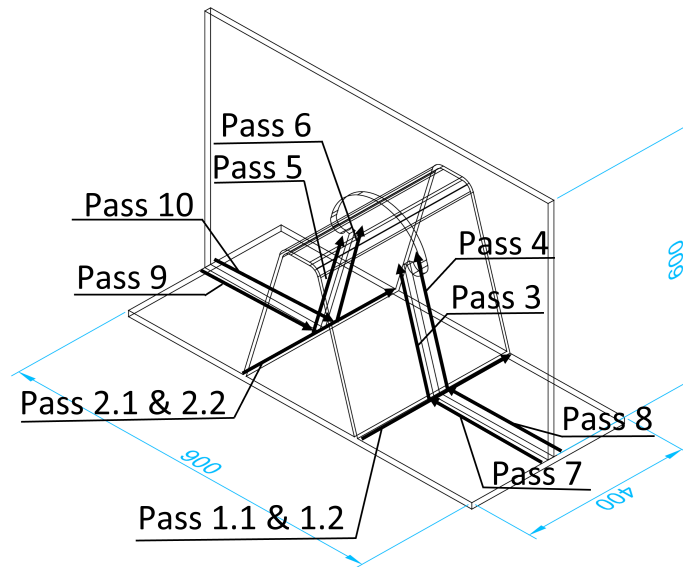


Figure F.1: Welding passes definition

Table F.2: Sequence of events specimen 2

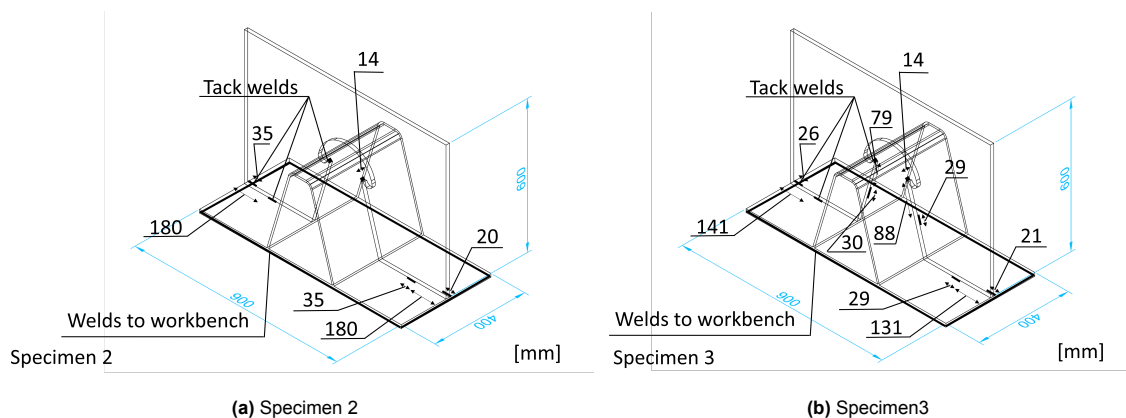
Action	Duration [mm:ss]	Voltage [V]	Current [A]	Wire feeding speed [mm/min]	Wire type	Recorded temp range [°C]
Fill pass 1	00:52	24.5	250	9.5	52RC	0-650
Cooling 1.1	05:47					
Pass 1	01:25	24.5	250	9.5	52RC	-20-120
Cooling 1.2	06:40					
Fill pass 2	00:52	24.5	250	9.5	52RC	0-650
Cooling 2.1	04:02					
Pass 2	01:20	24.5	250	9.5	52RC	300-1500
Cooling 2.2	57:00					
Pass 3	01:30	22.8	240	8.2	52RC	0-650
Cooling 3	04:57					
Pass 4	01:30	22.8	240	8.2	52RC	300-1500
Cooling 4	05:09					
Pass 5	01:28	22.8	240	8.2	52RC	0-650
Cooling 5	05:15					
Pass 6	01:21	22.8	240	8.2	52RC	0-650
Cooling 6	15:09					
Pass 7	00:58	24.2	250	9.5	52RC	0-650
Cooling 7	50:00					
Pass 8	00:59	24.2	250	9.5	52RC	0-650
Cooling 8	15:38					
Pass 9	00:57	24.2	250	9.5	52RC	0-650
Cooling 9	10:26					
Pass 10	01:00	24.2	250	9.5	52RC	0-650

Table F.3: Sequence of events specimen 3

Action	Duration [mm:ss]	Voltage [V]	Current [A]	Wire feeding speed [mm/min]	Wire type	Recorded temp range [°C]
Fill pass 1	00:42	28.2	264	10.5	MC715H	300-1500
Cooling 1.1	01:42					
Pass 1	01:18	28.2	264	10.5	MC715H	300-1500
Cooling 1.2	62:00					
Fill pass 2	00:43	28.2	264	10.5	MC715H	300-1500
Cooling 2.1	07:01					
Pass 2	01:10	28.2	264	10.5	MC715H	300-1500
Cooling 2.2	38:00					
Pass 3	01:22	22.8	250	8.5	52RC	300-1500
Cooling 3	06:46					
Pass 4	01:10	22.8	250	8.5	52RC	300-1500
Cooling 4	00:18					
Pass 5	01:25	22.8	250	8.5	52RC	300-1500
Cooling 5	02:17					
Pass 6	01:17	22.8	250	8.5	52RC	300-1500
Cooling 6	11:00					
Pass 7	01:03	28.2	250	10.5	MC715H	300-1500
Cooling 7	01:53					
Pass 8	00:50	28.2	250	10.5	MC715H	300-1500
Cooling 8	07:00					
Pass 9	00:55	28.2	250	10.5	MC715H	300-1500
Cooling 9	04:07					
Pass 10	00:57	28.2	250	10.5	MC715H	300-1500

F.2. Tack weld geometry

The tack weld geometry after fitting the crossbeam in specimen 2 and 3 are given in Figure F.2. A 3D scan after fitting the crossbeam of specimen 1 was not made, so no exact dimensions are known, but the position and length of the tack welds were similar to Specimen 2.

**Figure F.2:** Tack welds after fitting of the crossbeam